Modelling Contact Mechanics with improved Green's Function Molecular Dynamics

Dissertation

zur Erlangung des Grades
des Doktors der Naturwissenschaften
der Naturwissenschaftlich-Technischen Fakultät
der Universität des Saarlandes

von

Yunong Zhou

Saarbrücken
2020

UNIVERSITÄT
DES
SAARLANDES

Tag des Kolloquiums: 17. Februar 2021

Dekan: Prof. Dr. Jörn Erik Walter

Berichterstatter: Prof. Dr. Martin H. Müser

Prof. Dr.-Ing. Stefan Diebels

Vorsitz: Prof. Dr.-Ing. Dirk Bähre

Akad. Mitarbeiter: Dr.-Ing. Florian Schäfer

Declaration of Authorship

Eidesstattliche Erklärung

Ich erkläre hiermit an Eides Statt, dass ich die vorliegende Arbeit selbstständig verfasst und keine anderen als die angegebenen Quellen und Hilfsmittel verwendet habe.

Statement in Lieu of an Oath

I hereby confirm that I have written this thesis on my own and that I have not used any other media or materials than the ones referred to in this thesis.

Einverständniserklärung

Ich bin damit einverstanden, dass meine (bestandene) Arbeit in beiden Versionen in die Bibliothek der Materialwissenschaft und Werkstofftechnik aufgenommen und damit veröffentlicht wird.

Declaration of Consent

I agree to make both versions of my thesis (with a passing grade) accessible to the public by having them added to the library of the Material Science and Engineering Department.

Datum/Date: _____

Unterschrift/Signature: _____

Abstract

Modelling Contact Mechanics with improved Green's Function Molecular Dynamics

by Yunong Zhou

Green's function molecular dynamics (GFMD) is frequently used to solve linear boundary-value problems using molecular-dynamics techniques. In this thesis, we first show that the convergence rate of GFMD can be substantially optimized. Improvements consist in the implementation of the so-called "fast inertial relaxation engine" algorithm as well as in porting the solution of the equations of motion into a Fourier representation and a shrewd assignment of inertia. GFMD was furthermore generalized to the simulation of finite-temperatures contact mechanics through the implementation of a Langevin thermostat. An analytical expression was derived for the potential of mean force, which implicitly describes the interaction between a hard wall and a thermally fluctuating elastomer. GFMD confirmed the correctness of the derived expression. A Hertzian contact was simulated as additional benchmark. Although the thermally induced shift in the displacement can be substantial, it turns out to be essentially independent of the normal load. A final application consisted in the test of the frequently made hypothesis that contact area and reduced pressure are linearly related for randomly rough surfaces. The relation was found to be particularly reliable if the pressure is undimensionalized with the root-mean-square height gradient.

Zusammenfassung

Modellierung von Kontaktmechanik mit verbesserter Green's Function Molecular Dynamics

by Yunong Zhou

Green's function molecular dynamics (GFMD) wird häufig verwendet, um lineare Randwertprobleme im Rahmen einer Molekulardynamik-Simulation zu lösen. In dieser Dissertation zeigen wir zunächst, dass die Konvergenzrate von GFMD substantiell optimiert werden kann. Verbesserungen bestehen in der Implementierung des sogenannten "fast inertial relaxation engine" Algorithmus sowie der Verlagerung der Lösung der Bewegungsgleichungen in die Fourier-Darstellung und einer geschickter Wahl der Massen. Desweitern wurde GFMD zur Simulation der Kontaktmechanik bei endlichen Temperaturen durch Verwendung von Langevin Thermostaten verallgemeinert. Diesbezüglich wurde ein analytischer Ausdruck für ein effektives thermisches Potential hergeleitet, welches die Thermik repulsiver Wände implizit beschreibt und durch GFMD bestätigt wurde. Als Referenzsystem wurde ein zudem klassischer Hertz'scher Kontakt simuliert. Obgleich die Thermik eine substantielle Verschiebung der Auslenkung bewirken kann, erweist sich die Auslenkung als nahezu unabh"angig von der Normalkraft. Schliesslich konnte als Anwedung auch die häufig für zufällig raue Oberflächen postulierte lineare Abhängigkeit zwischen realer Kontaktfläche und reduziertem Druck getestet werden. Sie gilt vor allem dann, wenn der Druck über dem im echten Kontakt gemittelte Standardabweichung des Höhengradienten entdimensionalisiert wird.

Acknowledgements

First and foremost, I would like to express my sincerest appreciation to my supervisor, Prof. Dr. Martin H. Müser, for his academic instruction and encouragement during my thesis work. Without his enlightening and patient guidance, this thesis would not have been possible.

I would also like to acknowledge the other members of my committee: Prof. Dr. Stefan Diebels, and Prof. Dr. Dirk Bähre. I want to thank each of them for attending my Ph.D. defense, reading my thesis, and providing constructive suggestions.

I also received invaluable advice from my group mates. I want to give special recognition to Dr. Anle Wang for his enthusiastic help on debugging my simulation codes during these years; Dr. Hongyu Gao for his suggestions on scientific research; and Dr. Sergey Sukhomlinov for his instructions and discussions on the CSMP course and research.

Lastly, I would like to thank my parents for all the endless love, support, and encouragement in the ups and downs during my years at Saarland University.

Content

Chapter 1

Introduction

1.1 Background

Contact mechanics is a study that focuses on the deformation of elastic bodies when they contact each other. The pioneering work on contact mechanics was another important contribution by the famous German physicist Heinrich Hertz, following his confirmation of the existence of electromagnetic waves. In 1882, Hertz solved the adhesion- and frictionless contact problem of two linear elastic spheres analytically [1]. So far, the analytical work managed by Hertz on contact mechanics still remains the theoretical basis for many practical contact problems in engineering, and has a profound influence on the development of mechanical engineering and tribology in particular [2]. Since then, the study of contact mechanics has made great progress. Johnson *et al.* strived to include short-ranged adhesion into classical Hertzian contact problem, the resulting theory work was known as Johnson-Kendall-Roberts (JKR) model [3]. Another similar work was managed by Derjaguin *et al.*, in which the interaction was replaced by long-ranged force. It is known as Derjaguin-Muller-Toporov (DMT) model [4].

All of the theoretical works mentioned above considered only contacts of smooth bodies. However, there is no such an absolutely smooth surface in the world, even a highly polished surface will have many microscopic asperities. Therefore, accurately evaluating the true contact situation, such as knowing the true contact area of rough surface, is significant for many engineering applications. Currently, the dominant rough contact theories can be broadly divided into the following two categories: (1) multiple asperity contact model, pioneered by Greenwood and Williamson in their Greenwood-Williamson (GW) model; (2) scaling theory for randomly rough contacts proposed by Persson, which is also known as Persson

theory. More details about these two theories will be outlined in the following section.

In terms of numerical methods, the boundary element method (BEM) and the finite element method (FEM) provide effective approaches of solving contact mechanics problems with complex boundary conditions. However, for numerical simulations of contact problems that consider small scale roughness for the purpose of practical interest, a fine surface grid is necessary for the numerical contact analysis. As a result, rough surface contact problems generally need to be conducted on grids with a large number of nodes. Solution of such huge systems of equations is extremely time-consuming even on high speed computers. Thus, it is particularly meaningful to study the optimization of numerical simulations. Polonsky *et al.* proposed a conjugate-gradient (CG) based method combined with the multi-level multi-summation (MLMS) algorithm to obtain a fast converge contact mechanics solver [5]. Bugnicourt *et al.* developed a similar toolbox based on CG method, while the MLMS algorithm was replaced by fast Fourier transform (FFT) algorithm [6]. Campana and Müser developed Green's function molecular dynamics (GFMD)[7], which, as other boundary value method do, allows us to simulate the linear elastic response of contact problem in terms of the displacement in the top layer of elastic solid.

So far, contact mechanics is adopted in a wide range of applications, ranging from traditional mechanical engineering systems, microelectromechanical systems (MEMS), and biological systems.

In the domain of classical mechanical engineering, the performance of tires, gaskets, sealings, braking systems and so on are closely related to their contact mechanics. A commonly used example is the leakage problem of seal in the water tap or hydraulic system. The gap and the relative contact area between the contact solids play a critical role in this issue. Many studies tried to understand how external load and surface roughness affect the gap and relative contact area [8–11]. These studies could in turn make it possible to design a more reliable mechanical device to reduce leakage. Even though a seal is only a small component, it deserves a lot of attention. In the event of leakage in the hydraulic part, the reliability would be reduced, and the oil would be wasted. In some instances, it could also trigger an undesirable accident, such as the Challenger disaster.

The mechanical properties of the contact process in MEMS is another substantial topic in contact mechanics. MEMS is a modern technology, which combines microelectronics and mechanical engineering. It has been broadly employed in a number of applications, which profoundly affect people's daily life. A classical application is a pressure sensor, which is a kind of device that receives pressure as an input signal and outputs electrical signals as a function of the input pressure. In general, a pressure sensor could be modeled as an elastic body with finite thickness deposited on a rigid nominally flat substrate, *e.g.*, silicon. Its operating scale is in the micrometer range. There are pieces of evidences showing that, the surfaces cannot be regarded as smooth [12, 13]. Additionally, due to the sizable surface-volume ratio in MEMS devices, surface force, *e.g.*, van der Waals forces, start to play an important role in adhesion. Vast studies have demonstrated that surface roughness is a prominent factor reducing in adhesion [14, 15]. At this point, it is interesting to study how surface roughness and adhesion contribute to the output electrical signal in a pressure sensor, which is still in the range of contact mechanics study. On the other hand, some studies have demonstrate that the thermal effect could significantly affect van der Waals interactions [16–18]. At this point, considering the performance of MEMS devices in different conditions, such as a wide range of temperature, it is also interesting to include the effect of thermal fluctuation into a contact mechanics treatment.

1.2 Approaches to contact mechanics

As mentioned in the previous section, the classical Hertzian contact theory, which was conceived in 1881, established the groundwork for the field of contact mechanics. In the next two hundred years, a diverse understanding of rough surfaces was developed and a number of theories of rough contact mechanics were formulated based on this understanding. The most dominant of these are GW model (multiple asperity model) and Persson theory (scaling theory for randomly rough contact). Since this thesis mainly focuses on Hertzian and random rough surface contacts, this section will review these methods briefly. On the other hand, numerical techniques for the solution of contact problem, such as GFMD, will also be discussed.

1.2.1 Theory approaches

Single asperity contact theory

The theory work conducted by Hertz is commonly considered to be the beginning of modern contact mechanics study [1]. He solved the adhesion- and frictionless normal contact problem at small load between two elastic sphere bodies with Young's modulus E_1 and E_2, Poisson ratio ν_1 and ν_2 and radius curvature R_1 and R_2. This contact problem is equivalent to the contact of a rigid parabolic indenter with radius curvature R_c and a flat half-space elastic surface with effective modulus E^* if satisfying the following relation:

$$\frac{1}{R_\mathrm{c}} = \frac{1}{R_1} + \frac{1}{R_2}$$

and

$$\frac{1}{E^*} = \frac{1-\nu_1^2}{E_1} + \frac{1-\nu_2^2}{E_2}$$

A typical Hertzian contact model is drawn in Fig. 1.1.

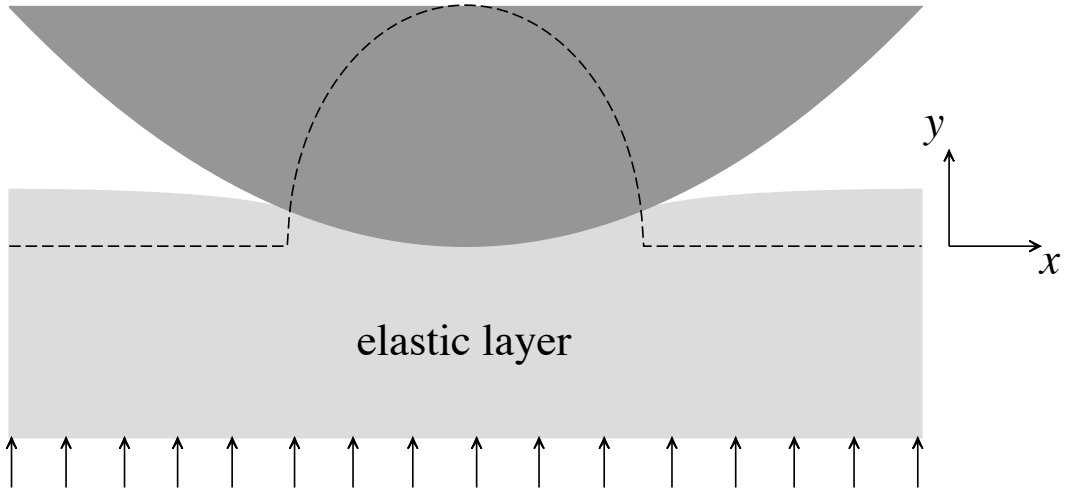

Figure 1.1: Hard-wall constraint, elastic solid of finite thickness compressed by a parabolic indenter. The dotted line shows the associated stress profile.

The parabolic indenter is given by

$$h(\mathbf{r}) = \frac{r^2}{2R_\mathrm{c}}$$

where R_c is the radius of curvature and $r = \sqrt{x^2 + y^2}$ is the in-plane distance of the center of the indenter from the origin of the coordinate system. The gap $g(x, y)$ represents the distance between elastic solid and rigid parabolic indenter, which reads

$$g(x, y) = h(\mathbf{r}) - u(x, y)$$

where $u(x, y)$ is defined as the displacement of elastic solid. The hard-wall constraint is applied in Hertzian contact theory, which indicates that the indenter cannot penetrate the elastic layer, it reads

$$g(x, y) \geq 0$$

Hertzian theory predicts that the contact area a_c increases with external force F_N, which reads,

$$a_c^3 = \frac{3F_N R_c}{4E^*} \tag{1.1}$$

The stress profile in the contact area is given below.

$$\sigma(r) = \sigma_0 \left[1 - \left(\frac{r}{a_c}\right)^2\right]^{1/2} \tag{1.2}$$

where $\sigma_0 = 3F_N/(2\pi a_c^2)$ is the maximum (compressive) stress.

The traditional Hertz theory only included the repulsion force induced by the squeezing of contact bodies. This approach is applicable to macro-scale contact problems. However, the surface force, which is neglected at the macro-scale, can become effective at micrometer, or even smaller scales. This surface force stems from van der Waals forces. Because surface forces play an essential part in many technical applications and biological systems, it is necessary to generalize the nonoverlap Hertzian theory to adhesive contact theory.

Towards this end, Johnson *et al.* reinvestigated the Hertzian contact problem by considering adhesive interaction, which is also known as JKR model [3]. JKR theory included adhesion as short-range interaction, which means JKR theory only considered the adhesion within the contact area between two bodies to predict the force response of the system. The adhesion outside the contact area is neglected. At this point, Johnson *et al.* derived the expression of the contact area a_c as a

function of external force F_{N} to be

$$a_{\mathrm{c}}^3 = \frac{3R_{\mathrm{c}}}{4E^*}\left(F_{\mathrm{N}} + 3\gamma\pi R_{\mathrm{c}} + \sqrt{6\gamma\pi R_{\mathrm{c}}F_{\mathrm{N}} + (3\gamma\pi R_{\mathrm{c}})^2}\right), \tag{1.3}$$

where γ is the energy per unit contact area. When $\gamma = 0$, this expression reduces to Hertzian theory, as shown in Eq. (1.1). In the JKR model, an additional force F_{p} is required to separate the contact bodies, this pull-off force is predicted as

$$F_{\mathrm{p}} = -\frac{3}{2}\gamma\pi R_{\mathrm{c}} \tag{1.4}$$

Unlike the JKR model, Derjaguin *et al.* treated adhesion as a long-range interaction and neglected the effect of adhesion on the deformation of elastic bodies [4]. As a result, adhesion force behaves as an external load that is independent of the contact area. This model is known as the DMT model, for which the contact area is predicted as

$$a_{\mathrm{c}}^3 = \frac{3R_{\mathrm{c}}}{4E^*}\left(F_{\mathrm{N}} + 2\gamma\pi R_{\mathrm{c}}\right) \tag{1.5}$$

When contact area $a_{\mathrm{c}} = 0$, the resulting pull-off force is given by

$$F_{\mathrm{p}} = -2\gamma\pi R_{\mathrm{c}} \tag{1.6}$$

Apparently, the estimation of the pull-off force in DMT theory remains different from that in JKR theory. There was a longtime discussion about the way to explain this divergence. Tabor recognized that the JKR model and DMT model describe the opposite limits of short-range and long-range interaction [19]. He demonstrated that the opposition between these two theories could be fixed by introducing a dimensionless parameter μ_{T}, which is now known as Tabor parameter.

$$\mu_{\mathrm{T}} = \left[\frac{R_{\mathrm{c}}\gamma^2}{E^{*2}z_0^3}\right]^{\frac{1}{3}} \tag{1.7}$$

where z_0 characterizes the range of adhesion. Essentially, the Tabor parameter could be interpreted as the ratio of elastic deformation induced by adhesion and the effective range of this surface force. The contact is close to JKR limit when μ_{T} is large ($\mu_{\mathrm{T}} > 5$) while close to DMT limit when μ_{T} is small ($\mu_{\mathrm{T}} < 0.1$) [20].

Contact mechanics theory of nominally flat surfaces

Classical single-asperity contact mechanics assumes that the contact surface is geometrically smooth. However, even though the real surface appears to be flat on a macro-scale, it is rough on the micro-scale. Standing by a practical point of view, the Hertzian theory, and the JKR and DMT model cannot meet the requirement of mechanical engineering demands. In this case, various models based on roughness representation are developed to describe the contact behavior between the elastic surface and rough indenter. One of the pioneering works is developed by Greenwood and Williamson, known as the GW model [21].

GW model solved the contact between an ideally flat surface and a nominally flat surface with many asperities. In this model, numerous asperities are distributed on a nominal flat plane. All asperity heights follow a specific height distribution function, for example, a Gaussian distribution. Each asperity is treated as a classical Hertzian model with identical radius curvature, however, interactions between asperity is neglected. In this case, the rough surface can be determined by three statistical parameters: the standard deviation of asperity height σ_{G}, a characteristic asperity radius R_{G}, and the surface density of asperities η_{G}. Suppose the separation between two surfaces is d, the height of a certain asperity is s. The penetration is given by $s-d$. Some asperities would be contact at this height, the probability is

$$\Pr(s>d)=\int_{d}^{\infty}\phi^{*}(s)ds \tag{1.8}$$

where $\phi^{*}(s)$ is the probability distribution function of the asperity height. Suppose the asperity height follows Gaussian distribution, $\phi^{*}(s)$ is normalized to standard Gaussian distribution to simplify the calculation, therefore,

$$\phi^{*}(s)=\frac{1}{\sqrt{2\pi}}e^{-\frac{s^{2}}{2}} \tag{1.9}$$

Once the rough surface is determined, the GW model could estimate the expression of relative contact area a_{r} and mean pressure p, which are quantities that people interested. They read

$$\begin{aligned} a_{\mathrm{r}} &= \pi\eta_{\mathrm{G}}R_{\mathrm{G}}\sigma_{\mathrm{G}}F_{1}(h) \\ p &= \frac{4}{3}\eta_{\mathrm{G}}E^{*}\sqrt{R_{\mathrm{G}}}F_{\frac{3}{2}}(h) \end{aligned}$$

where

$$F_n(h) = \int_h^\infty (s-h)^n \phi^*(s) ds$$

and $h = d/\sigma_{\mathrm{G}}$.

The GW model has been extensively used since it was published. Additionally, many studies made an effort to extend the utility of the GW model. For example, Fuller and Tabor applied the JKR model to each asperity instead of the traditional Hertzian contact model so that the GW model was able to include adhesion interaction [22].

Despite the successfully widespread use of the GW model, it still suffers from limitations [23]. First, it is still unclear that the statistical construction of the random surface is correct. Second, the GW model assumed that the surface roughness was only on a single length-scale. This assumption leads to an identical asperity radius of a random surface, which remains physically meaningless since the radius is obviously affected by the resolution of the measuring apparatus [24]. Third, the GW model neglected the elastic coupling between asperities. In fact, as mentioned by Campana, Müser and Robbins, any bearing area model, such as the GW model, produces a very poor contact auto-correlation function (ACF), which reads $\tilde{C}_c(q) \propto \Delta r^{-2(1+H)}$, while the correct ACF should be $\tilde{C}_c(q) \propto \Delta r^{-(1+H)}$ [25].

Persson developed an alternative approach to contact mechanics that was able to overcome many shortcomings of the GW model [24, 26, 27]. As mentioned by Archard, the stochastic parameters of random surfaces are dominated by the resolution of the measurement apparatus [28]. At this point, the rough surface in the Persson theory was designed to be self-affine fractal. A fractal surface has the property that the roughness's statistical property remains identical if the length scale changes. This kind of surface is defined by the surface roughness power spectrum $C(q)$, it reads

$$C(q) = C(q_0) \left(\frac{q}{q_0} \right)^{-2(H+1)} \tag{1.10}$$

where H is the Hurst exponent, which is related to the fractal dimension via $D_f = 3 - H$, q_0 indicates an arbitrary reference wave number. Usually, q_0 is chosen to be identical with $q_{\mathrm{r}} = 2\pi/\lambda_{\mathrm{r}}$, where $\lambda_{\mathrm{r,s}}$ represents the roll-off and shortest wavelength, respectively. In reality, the random surface cannot be self-affine over all length scales. Therefore, the power spectrum should be within a

range of $2\pi/\lambda_r \leq q \leq 2\pi/\lambda_s$, an idealized power spectrum is depicted in Fig. 1.2. A variety of surfaces are demonstrated by experiments that follow this feature [24, 26, 29, 30]. The Fourier transform of a random roughness surface profile

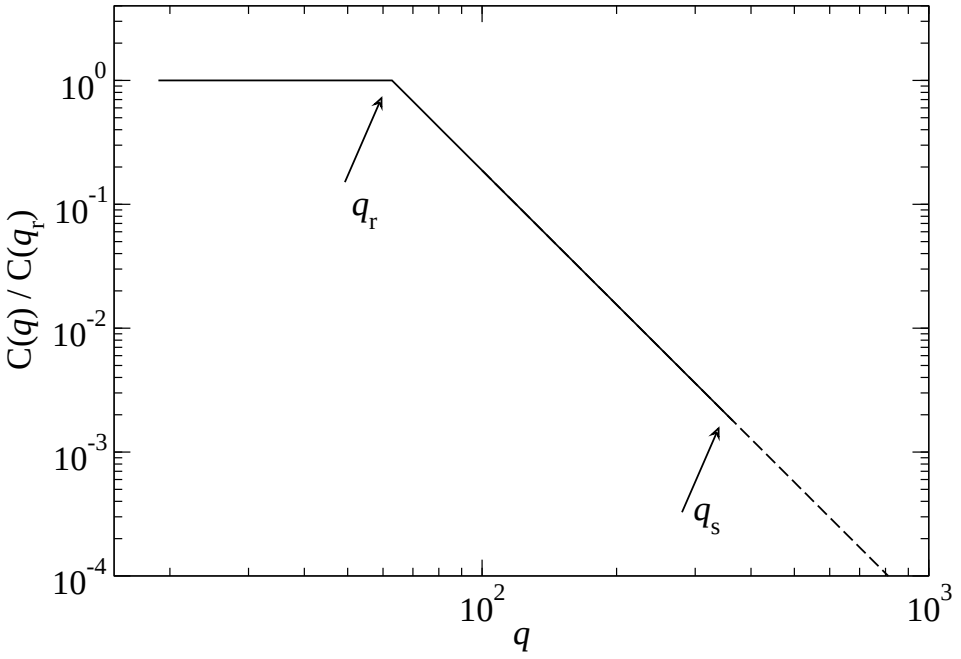

Figure 1.2: Surface roughness power spectrum of a surface which is self-affine fractal for $2\pi/\lambda_r \leq q \leq 2\pi/\lambda_s$. Dash line indicates that those wavenumbers cannot be detected by measurement apparatus.

satisfying the random-phase approximation is defined by

$$\tilde{h}(\mathbf{q}) = \sqrt{C(q)}e^{2\pi i r(\mathbf{q})} \tag{1.11}$$

where $r(\mathbf{q})$ is a uniform random number on $(0, 1)$. The resulting surface height $h(\mathbf{r})$ of random roughness surface is given by the inverse Fourier transform of $\tilde{h}(\mathbf{q})$. A typical random surface produced from the power spectrum shown in Eq. 1.10 is depicted in Fig. 1.3.

The basic idea of Persson theory is to understand how the pressure distribution $\Pr(p, \zeta)$, changes as the magnification $\zeta = q/q_r$ is increased, where $q_r = 2\pi/\lambda_r$ indicates the smallest wavenumber that could be detected. Additionally, when observing the random surface under the magnification ζ, only those asperities

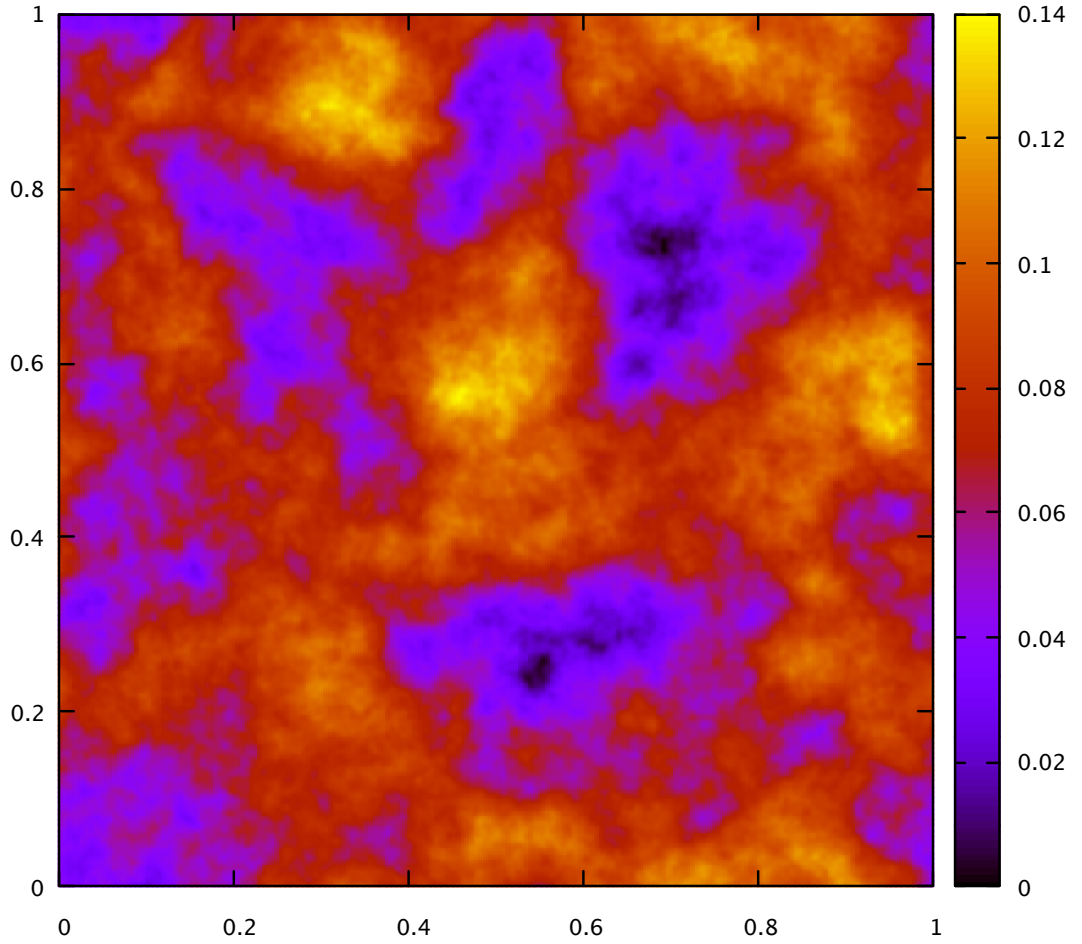

Figure 1.3: Height profile of random roughness surface with self-affine property for $\lambda_r/\mathcal{L} = 1/2$.

which wavenumber smaller than q could be detected. In a special case, say $\zeta = 1$, no asperity could be identified, which means, direct contact of two smooth planes [24, 31]. On the other hand, when $\zeta = q_s/q_r$, this magnification takes maximum, where $q_s = 2\pi/\lambda_s$ is the maximum wavenumber that measurement apparatus could detect.

The starting point in Persson theory is to assume that full contact is satisfied in any magnification. At this point, a probability density function $P(p, \zeta)$ is defined, where p is pressure. After that, a diffusion function is derived to describe the probability function changing with magnification ζ. It is given by

$$\frac{\partial P}{\partial \zeta} = f(\zeta)\frac{\partial^2 P}{\partial p^2} \tag{1.12}$$

where $f(\zeta)$ is a function that includes all information about the random roughness surface.

$$f(\zeta) = \frac{\pi}{4}\left(\frac{E}{1-\nu^2}\right)^2 q_r q^3 C(q) \tag{1.13}$$

Because the contact problem degenerates to the contact of two smooth surfaces when $\zeta = 1$, the initial condition of diffusion function should satisfy

$$P(p, 1) = \delta(p - p_0) \tag{1.14}$$

where $\delta(\cdot)$ is the Dirac delta function, p_0 represents nominal contact pressure. Under the assumption of full contact and no adhesion included, the boundary condition of diffusion function should be

$$P(0, \zeta) = 0 \tag{1.15}$$

The diffusion function could be solved analytically with the boundary condition and the initial condition given above. The relative contact area is given by

$$a_r = \mathrm{erf}\left(\frac{p_0}{2\sqrt{G}}\right) \tag{1.16}$$

where

$$G(\zeta) = \frac{\pi}{4}\left(\frac{E}{1-\nu^2}\right)^2 \int_{q_r}^{\zeta q_r} dq q^3 C(q) \tag{1.17}$$

is identical to the standard deviation of the stress in full contact. Compared with the GW model, Persson theory is more accurate when the contact area is very large.

1.2.2 Numerical approaches

Theoretical approaches to contact mechanics encounter difficulties when the contact is coupled with too many factors, such as temperature and humidity. In this case, physical experiment and numerical simulation would be more convenient ways to access contact mechanics studies. Consequently, these two approaches have attracted a lot of attention [32–34]. However, the experimental approach to contact mechanics to some extent still suffers limitations. First, the experiment apparatus can only work for contact mechanics problems with a specific strategy, namely, the applicability is limited. Second, in most cases, it is cost-consuming

to set up and maintain the experiment apparatus. Therefore, considering the fast development of computer technology in the past decades, it is urgent to develop a powerful numerical modeling technique to benefit the study of contact mechanics.

The finite element method (FEM) is one of the dominating numerical techniques to solve partial differential equations (PDE) in combination with boundary conditions, this kind of problem is known as boundary value problem (BVP). Generally, a contact mechanics problem can be mapped onto BVP without much effort. Therefore, the contact mechanics problem could also be investigated within the framework of FEM. A series of studies of contact mechanics with FEM approach has demonstrated its reliability [35–37].

However, when investigating the linear elastic contact problem, although FEM can also solve such problems, GFMD, which is a BEM, is more efficient. GFMD allows us to simulate the linear elastic response of a semi-infinite or finite-thickness elastic solid to an external load, or generally, boundary condition acting on the surface [7, 38]. During the last decades, GFMD has been used extensively to solve those contact mechanics of elastic solids with either simple parabolic or random roughness surfaces [39–42]. The advantage of GFMD is that it only propagates the displacement of the top layer. As a result, a relatively large system can be resolved, and the local potential energy minimum could be located more quickly than all-atom simulations and FEM. Most of the simulations in this thesis is concerned with stable mechanical structures. Therefore, the damping term is introduced to the dynamics, such that the minimum of potential energy could be quickly located with a well-chosen damping parameter.

As stated above, GFMD tends to find the Fourier transform of displacement field $\tilde{u}(\mathbf{q})$ such that the potential energy is the local minimum. Therefore, the Verlet algorithm is applied to propagate the system, which reads

$$\tilde{u}_{\text{new}}(\mathbf{q}) = 2\tilde{u}_{\text{now}}(\mathbf{q}) - \tilde{u}_{\text{old}}(\mathbf{q}) + \tilde{F}(\mathbf{q})\Delta t^2 \tag{1.18}$$

In the following, the basic logic of GFMD in terms of pseudo code is given.

`loop over time steps until the potential energy minimum is located`

- `add external force, adhesion, or finite-range repulsion`
  $F(\mathbf{r}) = F_{\text{int}}(\mathbf{r}) + F_{\text{ext}}(\mathbf{r})$
- `transform force to Fourier space`
  $F(\mathbf{r}) \rightarrow \tilde{F}(\mathbf{q})$

```
   - transform displacement to Fourier space
```
$u(\mathbf{r}) \rightarrow \tilde{u}(\mathbf{q})$
```
   - calculate elastic force in Fourier space
```
$\tilde{F}(\mathbf{q}) += \tilde{F}_{\mathrm{ela}}(\mathbf{q})$
```
   - add damping force
```
$\tilde{F}(\mathbf{q}) \mathrel{+}= \eta(\tilde{u}_{\mathrm{now}}(\mathbf{q}) - \tilde{u}_{\mathrm{old}}(\mathbf{q}))$
```
   - propagate the simulation with Verlet algorithm
   - transform displacement into real space
```
$u(\mathbf{q}) \rightarrow \tilde{u}(\mathbf{r})$
```
   - implement the boundary condition
end loop
```

1.3 Research gaps in contact mechanics

1.3.1 How to locate stable mechanical structure quickly?

Numerical optimization is a fundamental issue with the intention of time- and cost-efficient in a computer simulation. It is widely used in simulations on physics, chemistry and material science. The optimized quantity is a penalty function, which is often the total potential energy of a given system. For example, the stable mechanical structure requires the minimum potential energy to be located.

Various classical minimization methods, such as the steepest descent algorithm, take steps parallel to the negative gradient direction. If the penalty function is potential energy, the optimal direction is parallel to the force [43–46]. However, this algorithm can lead to undesired zig-zag motion if the bottom of this function is extremely flat, in which case the minimum is only reached slowly. The CG method avoids this inadequacy if the penalty function is quadratic. However, if the function is far from quadratic, CG method may suffer from many times of restart before the minimum potential is located.

An alternative approach was developed by Bitzek *et.al.* in 2006, known as the fast-inertial-relaxation-engine (FIRE). It is a minimization method which can suppress the zig-zag motion. Meanwhile, unlike CGM based algorithm, it can get rid of the quadratic limitation of the penalty function [47]. Up to now, FIRE has been successfully implemented into traditional particle-based simulation toolboxes, such

as LAMMPS. This fact indicates that FIRE should also work for the solution of partial-differential equations (PDEs). The reason is that the solution of PDEs can be mapped onto a MD problem after discretization of the variable space. Similarly, FIRE also works for boundary-value problems (BVPs). Therefore, it could also benefit the solution of contact mechanics simulation, which could be translated to a boundary-value problem (BVP). GFMD is a technique that allows such BVPs to be addressed within the framework of MD [7, 38, 48]. Although GFMD has been widely used in contact mechanics simulations, there is little research on optimization for this technique. There is also no research on the implementation of FIRE for the optimization of GFMD.

1.3.2 What structural parameters affect contact area?

Another issue regarding the real contact area has received considerable critical attention, especially the relation between relative contact area a_r and pressure p in nominally flat, linearly elastic contact [21, 36, 49–51]. It has been reported many times that the relative contact area a_r increases with pressure from very small but non-zero a_r up to $a_\mathrm{r} \approx 0.1$ in randomly rough surface contact simulations [35, 51–54]. This randomly rough, self-affine surface is defined by a height power spectrum $C(q)$, which reads $C(q) \propto q^{-2(1+H)}$, where H is the Hurst exponent, which is a quantity that correlates to the fractal dimension via $D_\mathrm{f} = 3-H$, q is the magnitude of wave vector $\mathbf{q}$. The phases of the randomly rough surface height in Fourier space are independent random numbers that are uniformly distributed on $(0, 2\pi)$, such that the surface is fully defined as the random phase approximation (rpa) surface. Persson theory managed to explain the linearity of area-pressure relation up to roughly 10% relative contact area on Taylor expanding of Eq. (1.16) if the randomly rough surface is rpa [8, 24]. Unlike the bearing-area model, Persson theory also finds an accurate pressure-dependence of the interfacial stiffness along with an accurate distribution function of the interfacial separation [27, 34, 54–57].

Although it is argued that the area-pressure relation should be linear for randomly rough surfaces, several indications suggest that this linearity is not accurate, especially when the external load is fairly small so that only a meso-scale patch in contact region is measured [58]. In fact, as Yastrebov and coworkers reported, even though several asperities were in contact, the area-pressure relation still deviates from linearity [59]. However, the ratio of system size and short-wavelength

cutoff was fixed in their simulations, in which case the deviation from the linearity may not convincing. To make it clear, Nicola *et.al.* carefully studied (1+1) dimensional, adhesionless contact between an elastic body and a randomly rough surface, remarkable logarithmic corrections to the area-pressure linearity were reported [42]. After that, a similar study, which was (2+1) dimensional, adhesive contact between an elastic solid and a randomly rough, self-affine surface was conducted [60]. In this study, a clearly sublinear scaling was found. However, since they studied the adhesive contact problem, the deviation from linearity could stem from the adhesive hysteresis.

It is still remain unclear how the Hurst exponent affects the linear pre-factor of area-load relation. Some studies claimed that this pre-factor is closely correlated with the Nayak parameter at fixed pressure [59, 61, 62]. However, as mentioned above, the ratio of system size and short-wavelength cutoff was fixed in their simulations, as a result, the logarithmic relation between contact area and the Nayak parameter is not plausible. In fact, the dependence of the pre-factor on the Nayak parameter turns out to be weak if the surface is not in the domain of ideally random rough. To make it clear, let us consider two thought experiments regarding the contact problem of nominally flat surfaces. In the first experiment, we arbitrary modify the height profile of the rough indenter in non-contact zone, but make sure that all modified points are below the elastic body. In such a way, the contact area remain unchanged, while the Nayak parameter could have shifted by orders of magnitude. In the second experiment, we modify the randomly rough surface such that the peaks are blunt and the valleys are steep. In this case, for a given pressure, the relative contact area should be large. After then, the indenter is flipped around, and the resulting contact area would decreased while the Nayak parameter remain unchanged. As a result, the correlation between the Nayak parameter and the pre-factor is not convincing, especially when the rpa surface is not considered.

1.3.3 How do thermal fluctuations affect Hertzian theory?

As mentioned above, many mechanical applications, such as gaskets, braking systems and pressure sensors, need to be considered for their performance at different temperatures because temperature can affect the mechanical contact in numerous

ways. Continuum contact mechanics theories, such as Hertzian theory, often ignore the effect of thermal fluctuations. This approximation is reasonable when applying the theory to macro-scale problems. However, if the contact problem is micro-scale or even smaller, the approximation could lead to noticeable errors for the load-indentation relation when two bodies are pressed against each other [63, 64]. Temperature can affect mechanical contacts and their interpretation in numerous other ways. For example, the presence of thermal noise generally impedes an unambiguous definition of contact area [65–69]. In addition, considering the van der Waals force between contact bodies, significant reduction of pull-off force with increasing temperature was observed in atomic-force microscope (AFM) experiment [16]. It is possible that thermal surface fluctuations, which were not included in the modeling of temperature effects on tip depinning, are responsible for a significant reduction of effective surface energy and thereby for a reduction of the depinning force. In fact, it has been shown that thermal fluctuations limit the adhesive strength of compliant solids [70]. Finally, in the context of colloid science, it may well be that thermal corrections have a non-negligible effect on the surprisingly complex phase diagram of Hertzian spheres [71]. It is therefore certainly desirable to model the effect of thermal fluctuations in a variety of contact and colloid problems.

While thermal fluctuations can be incorporated into simulations with so-called thermostats [72, 73], proper sampling can require a significant computational overhead. In addition, some contact solvers do not appear amenable to thermostatting. This concerns in particular those contact-mechanics approaches that optimize the stress field, as done with the classical solver by Polonsky and Keer [39, 74], rather than the displacement fields in the GFMD method [7, 75]. The issues sketched above indicate that investigating how thermal fluctuation affects the mean force F (per unit area) between surfaces as a function of their interfacial separation, or gap g is significant.

1.4 Outline of this thesis

My thesis is composed of five themed chapters. Chapter 1 gave a brief introduction of contact mechanics, such as the background of contact mechanics study and some fundamental approaches to contact mechanics, including theoretical and numerical methods. After that, the main research gaps in contact mechanics are

drawn and this thesis's contributions are summarized. Chapter 2 demonstrates that the fast-inertial-relaxation-engine (FIRE) benefits the solution of boundary-value problems. Additionally, considering that GFMD solves Newton's equations of motion in Fourier space, a rather remarkable speedup could be reached by choosing the masses associated with the eigenmodes of the free elastic solid appropriately. Chapter 3 investigates the classical Hertzian contact mechanics theory in the presence of thermal noise in the framework of GFMD and by using various mean-field approaches. Theoretical results are validated to be consistent with numerical simulations. Chapter 4 investigates what structural parameters affect the area-pressure relation. Chapter 5 summarizes the main conclusions that can be made from this thesis. Some suggestions for future work are also outlined.

Chapter 2

Optimizations of Green's function molecular dynamics

This Chapter demonstrates that FIRE can benefit the solution of BVPs. Towards this end, the mechanical contact between weakly adhesive indenter and a flat, linearly elastic solid is studied. The reason is that the contact mechanics problem of isotropic solids can be translated to BVP without much effort. Green's function molecular dynamics (GFMD) is a technique that allows BVPs to be addressed within the framework of MD [7, 38, 48]. To locate the minimum potential energy, a damping term is usually added to Newton's equation of motion. In this study, we replace the damping term in GFMD with a FIRE-based algorithm and investigate how this modification affects the rate of convergence.

We also investigate further optimization considering the rearrangement of inertia of modes. In a certain contact problem, or generally, a BVP, long wavelength modes relax more slowly than short wavelength modes. Therefore, it is possible to assign wavelength-dependent inertia to match the frequencies so that all modes relax on similar time scales.

Conjugate gradient (CG) method is one of the most commonly used minimization method in contact simulations. This method is also implemented into our GFMD code and the basic idea follows the works introduced by Bugnicourt *et al.* [6]. The CG method by Bugnicourt and co-workers had not only outrun regular GFMD in the contact-mechanics challenge [39]. In our understanding, the CG implementation of that group had led to the overall most quickly convergent solution, although other CG-based contact-mechanics methods [5, 76–78] may well be on par. The contact-mechanics challenge was a publicly announced large-scale contact problem

for three-dimensional solids having the added complexity of short-range adhesion. More than one dozen groups participated in the exercise using a similarly large number of solution strategies.

In the remaining part of this chapter, the problems are defined in Sec. 2.1, while the numerical methods are described in Sec. 2.2. Numerical results are presented in Sec. 2.3 and conclusions are drawn in the final Sec. 2.4.

2.1 Model and problem definition

In this study, we investigate the contact problem between a linearly elastic solid and a rigid indenter with various topographies. The contact modulus is defined as $E^* = E/(1-\nu^2)$, where E represents Young's modulus and ν is Poisson ratio. For isotropic solids with central interaction, the elastic tensor satisfies $C_{1122} = C_{1212}$. With this in mind, the bead-spring model can be used to simulate an isotropic elastic solid with $\nu = 1/4$.

The height of the elastic solid is set to $h = L/2$, where L is the width of the elastic body. A constant normal pressure is applied to the elastic body, causing it to come into contact with a rigid indenter fixed in space. Since the purpose of this chapter is to explore the optimization methods for GFMD rather than to study specific contact mechanics problems, in order to be time-efficient, we only consider the contact problem in the (1+1)-dimensional case, which means that the rigid indenter is a cylinder, whose symmetry axes are oriented parallel to the z axis. As a result, all our energies are line energy densities.

2.1.1 Treatment of elasticity

Bead-spring model

The first approach to compute the elastic energy is based on the bead-spring model, in which case the elastic solid is discretized into a square lattice. As shown in Fig. 2.1, the nearest neighbors and the next-nearest neighbors interact with springs of "stiffness" $k_1 = 0.75\ E^*$ and $k_2 = 0.375\ E^*$, respectively. (True spring stiffnesses have to be multiplied with the length of the cylinder in z-direction.) These values are independent of the discretization of our effectively two-dimensional elastic

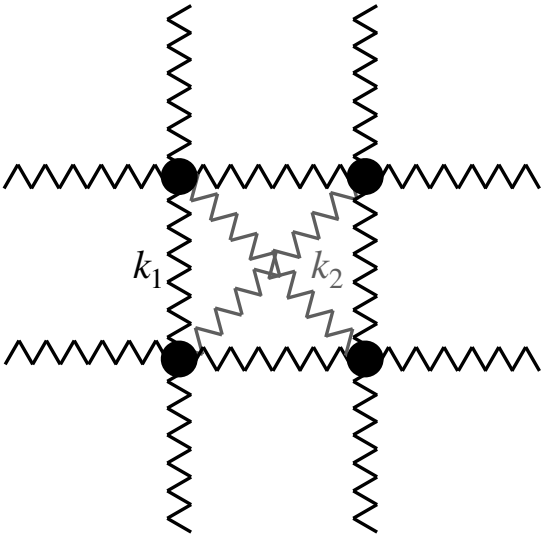

Figure 2.1: An illustrative diagram of a bead-spring system.

body. The equilibrium length of the two springs are set to the equilibrium nearest and next-nearest neighbor distance, r_1 and r_2, respectively. Therefore, the elastic energy, which is the sum of all spring energies can be written as below.

$$V_{\mathrm{el}} = \frac{1}{2} \sum_{i,j>i} k_{ij} \left\{ r_{ij} - r_{ij}^{\mathrm{eq}} \right\}^2 . \tag{2.1}$$

Inverse Green's function matrix

The basic idea of the second approach stems from GFMD, in which all information on the elastic energy is included in the displacement field of the bottom layer since the indenter is located below the elastic body. The elastic body allows for displacements in both directions that are normal to the z axis, *i.e.*, parallel to x and y. For this discrete set of displacements, we use the Fourier transform so that the displacements are propagated in reciprocal space, as a result, the elastic energy is also evaluated in the Fourier representation. The Fourier transform read

$$\tilde{u}_\alpha(q) = \frac{1}{N_x} \sum_{n=1}^{N_x} u_{n\alpha} \exp\{iqx\} \tag{2.2}$$

$$u_{n\alpha}(x) = \sum_q \tilde{u}_\alpha(q) \exp\{-iqx\}. \tag{2.3}$$

where N_x is the number of points in the surface and q denotes a wave number which satisfies $-\pi N_x/L \leq q < \pi N_x/L$. Greek indices enumerate Cartesian coordinates,

$\alpha = 1$ corresponding to the x coordinate and $\alpha = 2$ to y, while the Latin letter n enumerates grid points.

The elastic energy of this elastic solid is fully defined with these definitions. It reads

$$V_{\text{ela}} = \frac{L}{4} \sum_{q} \sum_{\alpha\beta} q M_{\alpha\beta}(q) u^*_\alpha(q) u_\beta(q), \tag{2.4}$$

where the matrix coefficients $M_{\alpha\beta}$ contain all needed information on the elastic coupling between different modes. They read [38]

$$\begin{aligned}
M_{11}(qh) &= (1-r)\frac{\cosh(qh)\sinh(qh) - rqh}{\|f(qh)\|} C_{11} \\
M_{12}(qh) &= \frac{1-r}{1+r}\frac{(1-r)\sinh^2(qh) - 2(rqh)^2}{\|f(qh)\|} C_{11} \\
M_{22}(qh) &= (1-r)\frac{\cosh(qh)\sinh(qh) + rqh}{\|f(qh)\|} C_{11},
\end{aligned}$$

where

$$\begin{aligned}
r &= \frac{1-s}{1+s} \\
s &= \frac{C_{44}}{C_{11}}
\end{aligned}$$

C_{11} and C_{44} are elastic constants in Voigt notation and

$$\|f(qh)\| = \cosh^2(qh) - (rqh)^2 - 1$$

2.1.2 Rigid indenters

The first example is the classical Hertzian contact problem, which is a parabolic rigid indenter in contact with a flat, elastic manifold. The indenter is depicted in Fig 2.2 and the elastic layer is defined in Sec. 2.1.1. The profile of the indenter is given by

$$h(x) = -x^2/2R_{\text{c}}, \tag{2.5}$$

where R_{c} is the radius of curvature.

In the second example, the indenter is replaced by a random rough, self-affine surface, as shown in Fig. 2.3. The power spectrum of random surface $C(q)$ for a

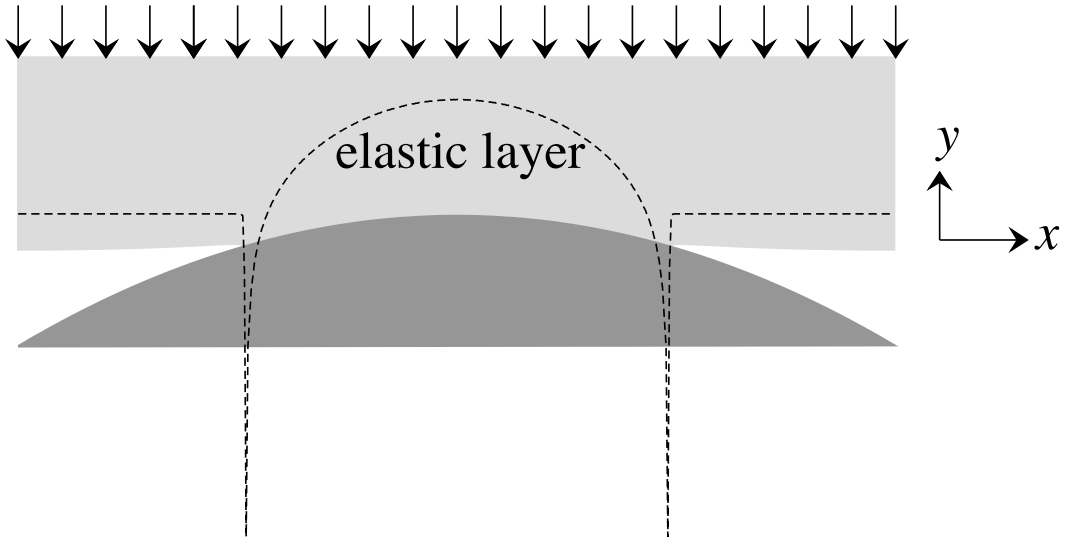

Figure 2.2: The elastic contact of a finite-thickness, linear elastic body with a rigid parabolic indenter. The interaction is defined as a short-ranged adhesion and an even shorter-ranged repulsion. The dotted line shows the associated stress profile.

$D = 1 + 1$ dimensional solid is defined as follows [79].

$$C(q) \propto q^{-2H-1}\Theta\left(q_{\max} - q\right),$$

where $H = 0.8$ is called the Hurst exponent. $\Theta(\bullet)$ is the Heavyside step function,

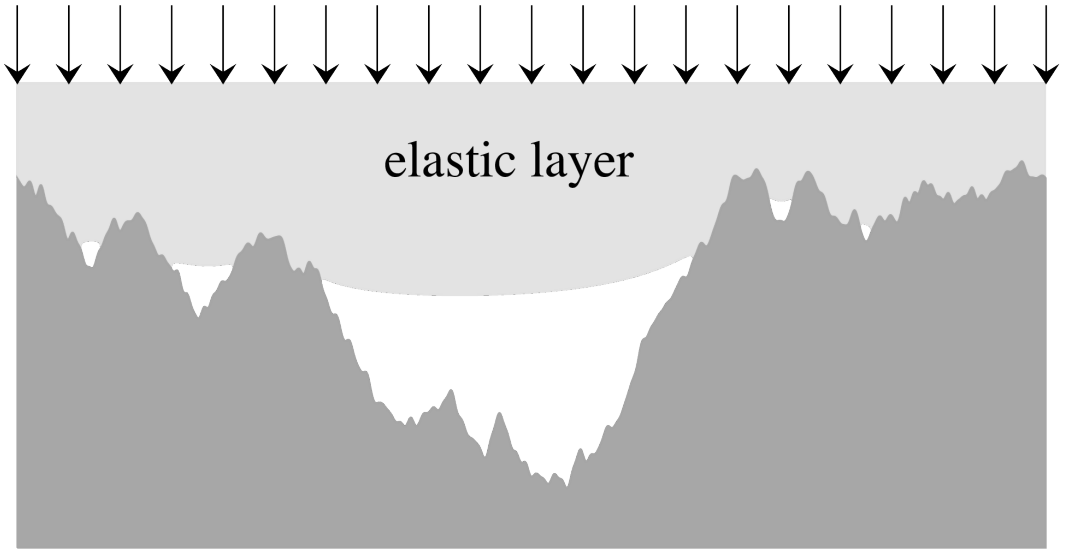

Figure 2.3: The elastic contact of a finite thickness linear elastic body with a rigid, randomly rough indenter. The figure is not to scale, *i.e.*, the resolution in y direction is enhanced. The height of the elastic solid $h = L/2$, where L is the width of this elastic solid.

and $q_{\max} = 1024\, q_0$ with $q_0 = 2\pi/L$.

The third and final example is the problem defined in the contact-mechanics challenge [39]. The indenter is similar to the second one, however, the surface is two dimensional and the interaction between the indenter and elastic surface is the short-ranged adhesion plus a hard-wall constraint. More details can be found in the original manuscript [39]. Configurations both in real space and Fourier space and the problem definition can be downloaded at [80]. So far, the implementation of mass-weighted GFMD method with a nonoverlap constraint is still problematic, therefore, we only evaluate the performance of FIRE-GFMD for this example. Mass-weighted and FIRE-GFMD are introduced in Sec. 2.2.

2.1.3 Interaction

The initial normal equilibrium positions of the elastic body are set to $y_n = 0$ if no external forces acting on the body. The lateral equilibrium positions are set to $x_n^{\mathrm{eq}} = nL/N_x$. Since the rigid indenter is fixed in space and the positions are determined, the gap g_n, namely, the normal distance of a grid point n from the indenter is given by

$$g_n = u_{n,y} - h_{\mathrm{s}}(x_n), \tag{2.6}$$

where $x_n = x_n^{\mathrm{eq}} + u_{n,x}$ is the lateral position of the discretization point n. Unlike classical Hertzian contact theory, the hard-wall constraint is abandoned by default in this study if not explicitly mentioned, otherwise the interaction is defined as short-ranged adhesion and an even shorter-ranged repulsion. At this point, the interaction energy (line density) is given by

$$V_{\mathrm{int}} = \frac{L}{N_x} \sum_n \gamma_1 \exp(-2g_n/\rho) - \gamma_2 \exp(-g_n/\rho) \tag{2.7}$$

where γ_i has the unit energy per surface area and ρ of length. In this study, the values of γ_1, γ_2, and ρ are set as $\rho \approx 2.56 \times 10^{-4}\ R_{\mathrm{c}}$, $\gamma_1 \approx 2.10 \times 10^{3}\ E^* R_{\mathrm{c}}$ and $\gamma_2 \approx 2.05\ E^* R_{\mathrm{c}}$. The equilibrium gap can be found by having the first-order derivative of the interaction equal to zero. With the choice of parameters, the equilibrium gap would be $\rho_{\mathrm{eq}} \approx 1.95 \times 10^{-3}\ R_{\mathrm{c}}$ and the resulting surface energy of $\gamma_{\mathrm{eq}} = 5.0 \times 10^{-4}\ E^* R_{\mathrm{c}}$ would be gained at a gap of ρ_{eq}. The resulting Tabor parameter is roughly 3, which means that the adhesion could be treated as short-ranged.

It is possible that one wants to map these reduced units to real units, it could be conducted by assuming that the ρ_{eq} equals to the typical atomic distance, say $\rho_{\mathrm{eq}} \approx 3\mathring{A}$, and the interfacial interaction $\gamma_{\mathrm{eq}} \approx 50$ mJ/m^2. With this choice, the radius of curvature of indenter $R_{\mathrm{c}} \approx 150$ nm and contact modulus $E^* \approx 650$ MPa. These values are representative of a thermoplastic polymer.

2.2 Numerical methods

2.2.1 FIRE GFMD

As introduced in Sec. 1.3.1, FIRE is a minimization method that can avoid the disadvantages of steepest descent algorithm and CG algorithm. The basic idea of FIRE in a certain simulation is described as follows: Inertia are assigned to the variables leading to an implicit averaging of the gradient direction over past iterations and turning a steepest-descent program into a MD code. At the same time, the instantaneous velocity is slightly biased toward the steepest-descent direction. Moreover, the time step size is increased with each iteration, which can be done because true dynamics do not matter. Once the vector product of velocity and forces (negative gradients) is negative all velocities are set to zero, the time step is set back to a small value, and the procedure is restarted with the original, small time step.

FIRE has been demonstrated to be efficient for the solution of particle-based simulations. Similarly, it should also benefit the solution of contact mechanics simulation, which could be translated to typical PDEs. The implementation of FIRE into GFMD in terms of pseudo code works as follows:

`loop over time steps until the minimum potential energy is located`

- `transform displacements to Fourier space`
  $u(\mathbf{r}) \rightarrow \tilde{u}(\mathbf{q})$
- `calculate velocities of each mode in Fourier space`
  $\tilde{v}(\mathbf{q}) = (\tilde{u}(\mathbf{q})_{\mathrm{now}} - \tilde{u}(\mathbf{q})_{\mathrm{old}})/\Delta t$
- `calculate elastic forces in Fourier space`
  $\tilde{F}(\mathbf{q}) = \tilde{F}_{\mathrm{ela}}(\mathbf{q})$
- `calculate the external load`
  $\tilde{F}(0)$ += p

- propagate the simulation with the Verlet algorithm
- modify velocity according to the following expression
  $\tilde{v}(\mathbf{q}) = (1-\xi)\tilde{v}(\mathbf{q}) + \xi\tilde{F}(\mathbf{q})\|\tilde{v}(\mathbf{q})\|/\|\tilde{F}(\mathbf{q})\|$
  if $V_{\rm pot}^{\rm now} < V_{\rm pot}^{\rm old}$, increase the time step and decrease $\xi \to \xi f_\xi$
  if $V_{\rm pot}^{\rm now} > V_{\rm pot}^{\rm old}$, decrease time step $\Delta t \to \Delta t f_{\rm dec}$, freeze the system
  $\tilde{v}(\mathbf{q}) = 0$ and set $\xi \to \xi_{\rm start}$.
- transform displacement into real space
  $u(\mathbf{q}) \to \tilde{u}(\mathbf{r})$
- implement the boundary condition

end loop

2.2.2 Mass-weighted GFMD

GFMD propagates the displacements according to the Newton's equations of motion in Fourier space. The expression for each mode reads

$$m(q)\ddot{\tilde{\mathbf{u}}} = \tilde{\mathbf{f}}(q) \tag{2.8}$$

where $\tilde{\mathbf{f}}(q)$ represents the total force in the Fourier space, which consists of an elastic force, an interaction force and an external force. $m(q)$ denotes an inertia for each mode. The expressions for forces are presented as follow:

$$\tilde{f}_{{\rm ela},\alpha}(q) = -\frac{qE^*}{2}\sum_\beta M_{\alpha\beta}(q)\tilde{u}_\beta(q), \tag{2.9}$$

$$\tilde{f}_{{\rm int},\alpha}(q) = \frac{1}{N_x}\sum_n \frac{\partial V_{\rm int}}{\partial r_\alpha}\exp\left(iqx_n^{\rm eq}\right), \tag{2.10}$$

$$\tilde{f}_{{\rm ext},\alpha}(q) = p_0\delta_{\alpha 2}\delta_{q0}, \tag{2.11}$$

where p_0 denotes the external force divided by the linear length of the system in x direction. This total force equals to the negative gradient of the total potential energy line density $V_{\rm tot}$, which reads

$$V_{\rm tot} = V_{\rm ela} + V_{\rm int} - p_0 N_x \tilde{u}_y(0), \tag{2.12}$$

If a static mechanical structure is required, the total potential $V_{\rm tot}$ should be minimized. In such a case, a contact-mechanics problem is translated to a mathematical minimization problem.

In traditional GFMD, the inertia $m(q)$ are assumed to be independent of the wave vector, in which case the inertia for each mode remains identical. In fact, the elastic deformation of an undulation with wave vector λ penetrates $O(\lambda)$ deep into the elastic body if the thickness is infinite. Therefore, a more natural dynamics would be achieved if $m(q)$ were chosen to proportionally to $1/q$. The efficient dynamics, which is applicable to locate the local minimum potential energy quickly, could be reached if the effective masses $m(q)$ are chosen proportional to the stiffness at wave vector q. For a free surface, this would be $m(q) \propto qE^*$, in the limit of large thickness h. In most contact problems, an external force applied on the elastic manifold, in which case an additional contribution arises due to the contact stiffness k_{cont}, which couples, in particular, to the center-of-mass (COM) or $q = 0$ mode. In this case, the resulting inertia for each mode $m(q)$ would be

$$m(q) \propto \sqrt{(qE^*)^2 + \theta(k_{\mathrm{cont}}/A)^2} \tag{2.13}$$

where A is the apparent contact area and θ a number of order unity. In this expression, the value of the contact stiffness k_{cont} requires extra consideration. If it is known reasonably well, then by rearranging the inertia of each mode according to the scheme presented above, the long-wavelength modes and short-wavelength modes will converge to their minimum values with similar characteristic times. Unfortunately, in some cases, it is difficult to obtain the exact value of the contact stiffness. However, a systematic slowing down with system size – or with increased small-scale resolution – is prevented from happening even if the estimate of the optimum choice for k_{cont} is off by a factor of 10 or 100.

In the case of randomly rough surfaces, k_{cont} can often be roughly estimated to be a small but finite fraction of the external pressure divided by the root-mean-square height $\bar{h}$, say $k_{\mathrm{cont}} \approx p_0/(10\bar{h})$.

2.2.3 Mass-weighted FIRE GFMD

As already mentioned in the introduction, FIRE can benefit the solution of classical boundary-value problems within the framework of MD. In principle, FIRE should also work for mass-weighted GFMD. The basic idea of this study is described below. The system is propagated without damping as long as the power

$$P = \mathbf{F} \cdot \mathbf{v} \tag{2.14}$$

is positive, where $\mathbf{F}$ and $\mathbf{v}$ are vectors containing the (generalized) forces and velocities of the considered degrees of freedom. The time step was increased in each iteration by 2%. Moreover, we redirected the current direction of steepest descent while keeping the magnitude of the velocity constant. This is done such that $\mathbf{v} \to (1-\xi)\mathbf{v} + \xi \mathbf{f} v/f$, where $\xi = 0.1$ initially and after each FIRE restart. Otherwise, $\xi(t+1) = 0.99\xi(t)$, where t is the time step.

This method is called "mass-weighting", because the dynamics are propagated in Fourier space and the inertia of each mode is designed to be proportional to the expected stiffness of a given mode. On the other hand, we also tried another scheme, in which the inertia $m(q)$ in propagation is kept constant, while q-dependent in the effective power evaluation. However, this approach did not optimize the simulation as expected, hence we do not consider this idea in this study. In this approach, the effective power is given by $\sum_q m(q)\tilde{\mathbf{F}}^*(q) \cdot \mathbf{v}(q)$. The effect of this and related modifications to FIRE was meant to make the slow modes move down in potential energy as long as possible before restarting the engine.

2.3 Numerical results

2.3.1 Hertzian indenter

We evaluated the efficiency of various minimization methods based on a contact mechanics problem with one parabolic and one randomly rough indenter in this section. We start with the simple parabolic contact problem, because it is much easier to validate the results through theoretical approach. Because of this advantage, this test case has become a benchmark for numerical solution technique in contact mechanics [81]. Because we utilize the short-range adhesion rather than nonoverlap constraint on the regular Hertz problem, the surface topography after equilibrium has features at small scale in addition to the long-range elastic deformation. Therefore, the elastic deformation of manifold consists of various length scales even though the indenter is simply parabolic.

Fig. 2.4 shows us how quickly various solution strategies minimize the energy at a fixed system size. Towards this end, we first compute the excess energy Δv, which is defined as the total potential energy minus the total potential energy of a fully relaxed structure. The excess energy is then divided by the value obtained for the

initial structure, which is set up such that the elastic manifold is flat and located ρ_{eq} above the highest indenter coordinate. The expression of Δv is given by

$$\Delta v = \frac{V_{\mathrm{tot}}(t) - V_{\mathrm{tot}}(\infty)}{V_{\mathrm{tot}}(0) - V_{\mathrm{tot}}(\infty)}$$

This figure shows us that the all-atom simulation is confirmed to be the most inefficient of all investigated methods, even when measured in (global) time steps, which does not account for the many layers that need to be simulated. The reason is the large disparity of frequencies in the system. The fastest mode, which is limits the time step, has an intrinsic frequency ω_{max} which is $O(N_x)$ higher than that of the slowest mode, ω_{min}, for which the damping is chosen to be roughly critical. The FIRE algorithm is successfully implemented into all-atom simulation, and it leads to an increase of the convergence rate of 6 for the investigated system size. However, this improvement does not surpass the performance of conventional GFMD, in which case the convergence rate increased by a factor of 2.5 compared with that of FIRE based all-atom simulation. The ratio $\omega_{\mathrm{max}}/\omega_{\mathrm{min}}$ reduces from $O(N_x)$ to $O(\sqrt{N_x})$, which is at the root of the speedup compared to natural dynamics.

Once FIRE is added to regular GFMD, the convergence rate increases by a factor of 3 compared to regular GFMD, which is slightly faster than the performance of CGM. CGM only leads to a speedup $\gtrsim 2$ at this system size compared to regular GFMD. In contrast, mass-weighted GFMD leads to a speedup of a factor of 10 compared to regular GFMD. Lastly, we implement FIRE into mass-weighted GFMD, the convergence rate increases by another 20%. The overall speedup is remarkable.

The FIRE based mass-weighted GFMD needs 75 iterations to reduce the excess energy to 10^{-5} of its original value compared to $\gtrsim 15000$ iterations for natural all-atom simulation, while regular GFMD requires 1000 iterations.

The reason why we choose the value of $\Delta v = 10^{-5}$ is to call a configuration related somewhat arbitrary. However, it is hard to tell difference between the stress profile produced when excess energy equals 10^{-5} and that of the fully relaxed structure when excess energy smaller than 10^{-5}. Specifically, errors in the stress are clearly less than 0.5% of the maximum (compressive) contact stress for the investigated and related examples. This error drops to roughly 10^{-3}% when excess energy smaller than 10^{-8}.

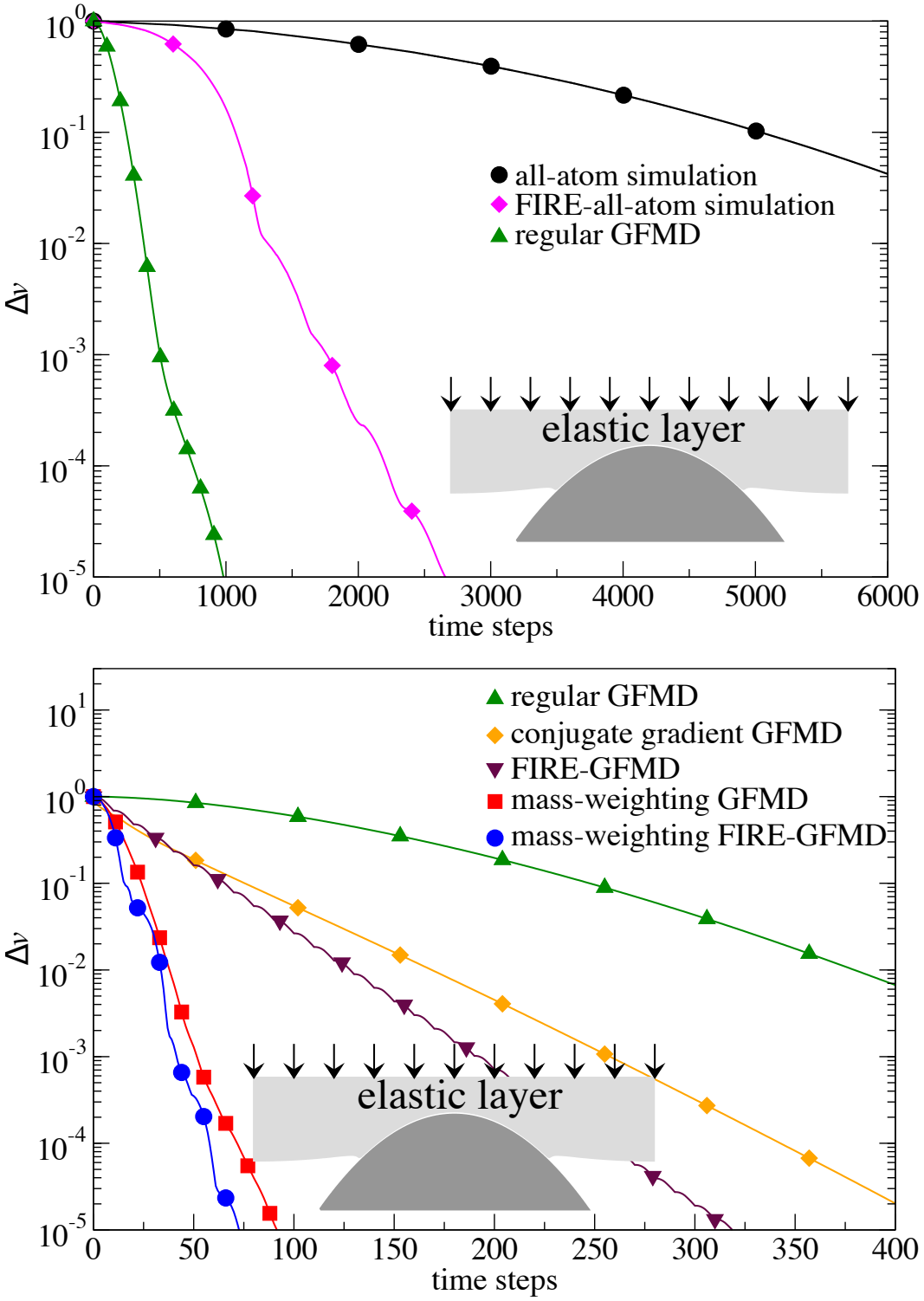

Figure 2.4: Relative excess energy Δv as a function of time steps for a parabolic indenter contact simulation with grid number $N_x = 512$. All GFMD-based methods have N_x grid points, while the all-atom simulations have $N_x \times N_y$ grid points, where $N_y = N_x/2$. The top and bottom graph presents different methods, regular GFMD being the only one reported in both graphs.

So far, we have anaylsed the performance of each algorithm with a fixed number of discretization points in contact mechanics problem. However, it is often important to know how the convergence rate scales with number of discretization points, or system size. The related results are depicted in Fig. 2.5.

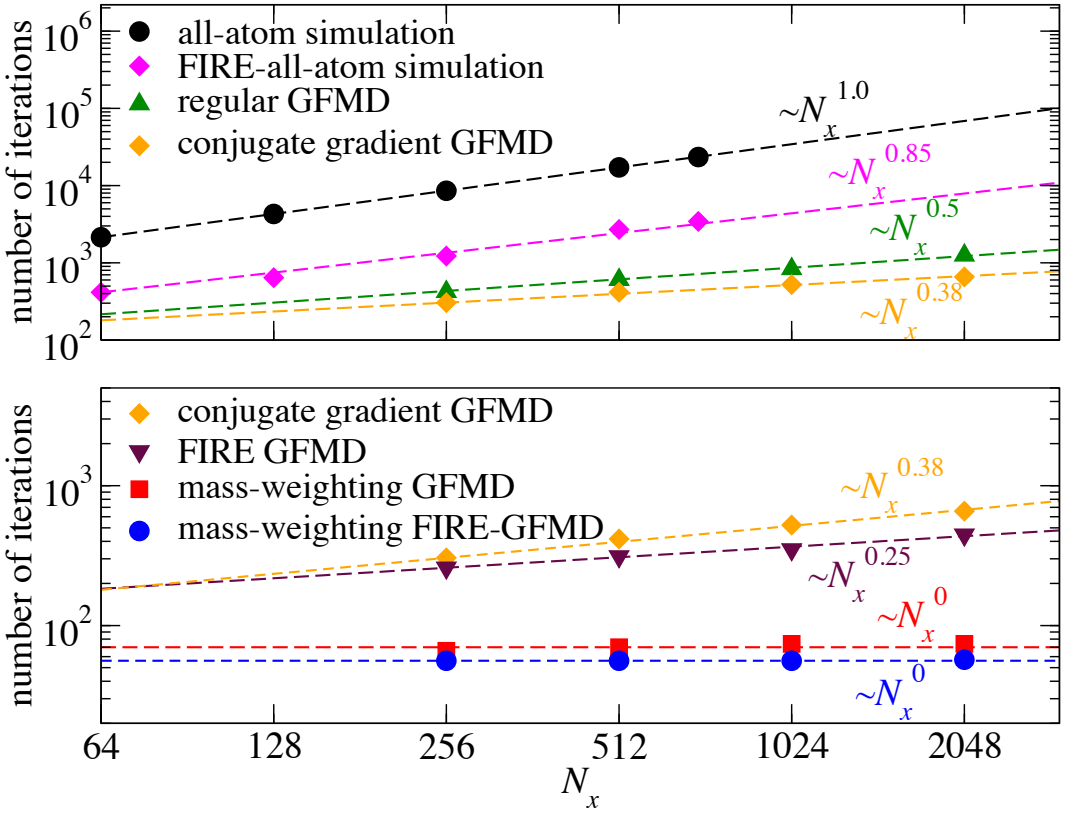

Figure 2.5: Number of iterations needed to relax the relative excess energy Δv to 10^{-5} for the Hertzian case as a function of the number of grid points. Top and bottom graph presents different method, conjugate-gradient method is the only one presented in both graphs.

This figure shows us that the number of iterations needed to decrease the excess energy to 10^{-5} scales linearly with N_x (or number of discretization points in the topmost layer) in an all-atom simulation. To achieve this scaling, the damping has to be reduced with increasing N_x. If the damping were kept constant, the long-range modes would be automatically over damped at large N_x and the scaling would go as N_x^2. Adding FIRE to an all-atom simulation could alleviates the situation, however, the exponent is only reduced marginally to 0.85. Regular GFMD improves that to a squareroot dependence.

The measured exponent reduced to 0.38 with CG and to 0.25 with FIRE. This indicates that FIRE slightly outperforms CG-based optimization. For the particular problem under consideration mass-weighting appears to eliminate the size

dependence altogether.

The scaling show in Fig 2.5 is found to be also valid for (2+1)-dimensional contact problems, whenever tested, *e.g.*, GFMD, FIRE-GFMD, and MW-GFMD. When the short-range repulsion was replaced by nonoverlap constraint, the scaling was also found to exist.

In computer simulations, considering the cost- and time-efficient issues, it is also significant to evaluate the relation between the CPU time per iteration and system size, which is analyzed in Fig. 2.6. In all-atom simulations, the relation between CPU time per iteration and system size satisfies a scaling law with exponent 2.0 (3.0 for three-dimensional systems). However, the exponent of this scaling decreased to 1.0 (2.0 for three-dimensional systems) plus a logarithmic correction for GFMD based approaches.

In a typical simulation, we could start with a relatively small system size, for which crude results can be obtained and reasonable parameters required for FIRE, damping, or mass-weighting can be gauged. After that, the continuum limit can be approximated with increasing resolution by keeping those parameters unchanged. In this way, the number of iterations is much reduced.

2.3.2 Randomly rough indenter

In this section, the adhesive Hertzian indenter is replaced by a purely repulsive self-affine, rigid indenter. Nevertheless, the trends in results part remain similar, as depicted in Fig. 2.7. Both FIRE and mass-weighting GFMD perform faster than regular GFMD. Implementing FIRE into mass-weighted GFMD, the convergence rate increased by a factor of 2, while the factor was 0.25 for simple parabolic indenter contact case.

2.3.3 Application to the contact-mechanics challenge

In this section, we reinvestigate the contact-mechanics-challenge problem. FIRE algorithm is used to optimize the simulation. Since this study is the first time for us to implement CGM into GFMD, it is possible to be unsufficient to conclude that FIRE outperforms CGM. The risk to be erroneous motivated us to apply FIRE

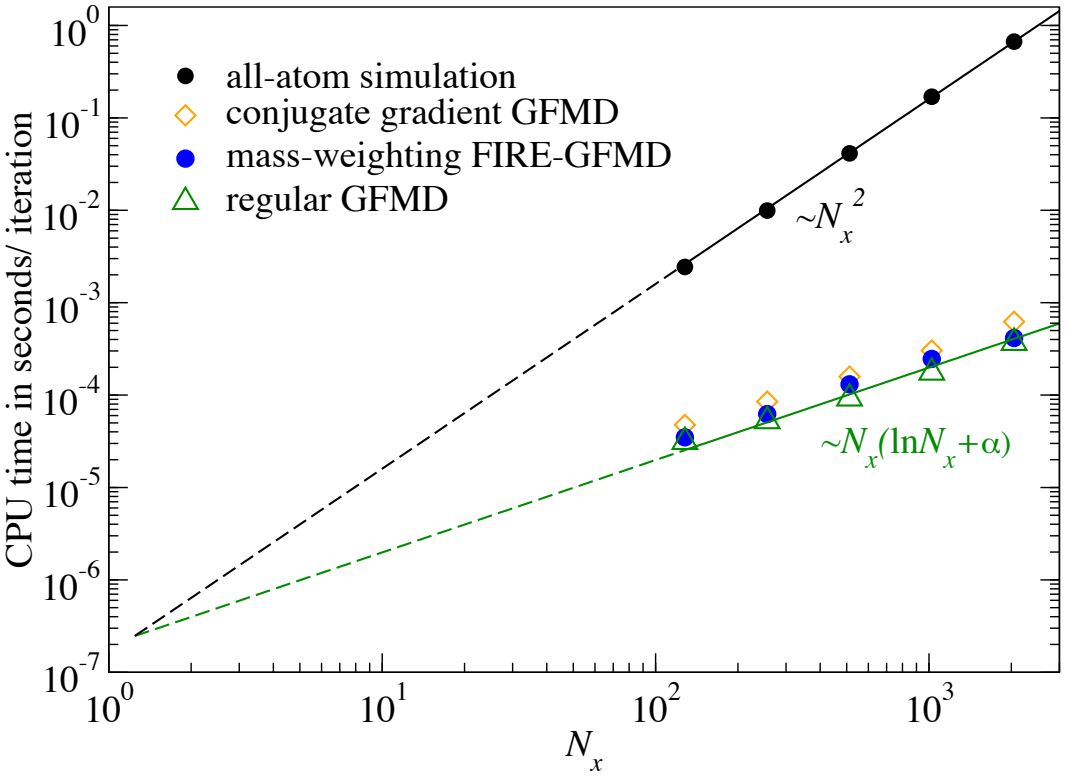

Figure 2.6: CPU time in seconds per iteration as a function of the linear system size N_x. The solid lines reflect fits, while the dashed lines are reverse extension of the fits. Adding mass weighting or FIRE or conjugate gradient method does not significantly affect the time per iteration for typically used numbers. All computations were performed on a laptop with a 1.6 GHz Intel Core i5 central processor unit (CPU). The FFTW version 3.3.5 is used in our code.

GFMD to the problem defined in the contact-mechanics challenge. CG methods was reported to spend 3000 iterations for a discretization points of 32768×32768, which definitely outrun the regular GFMD in terms of convergence rate, for which $30,000$ iterations were required to obtain a similar accuracy at that size. The data obtained from CGM, which was submitted by Bugnicourt and coworkers, revealed convergence to a few 10^{-9} times the maximum compressive stress. An even greater accuracy would certainly require higher data precision than those obtained when requesting "double" in C++ or "double precision" in Fortran.

The convergence of FIRE GFMD for the contact-mechanics-challenge problem is similar to that identified in this study for related contact problems. FIRE GFMD needs a little more than 500 iterations to reduce the excess energy to 10^{-3} of its original value. This value is slightly higher than that reported in the previous benchmark, which needs only roughly 300 to achieve the same reduction.

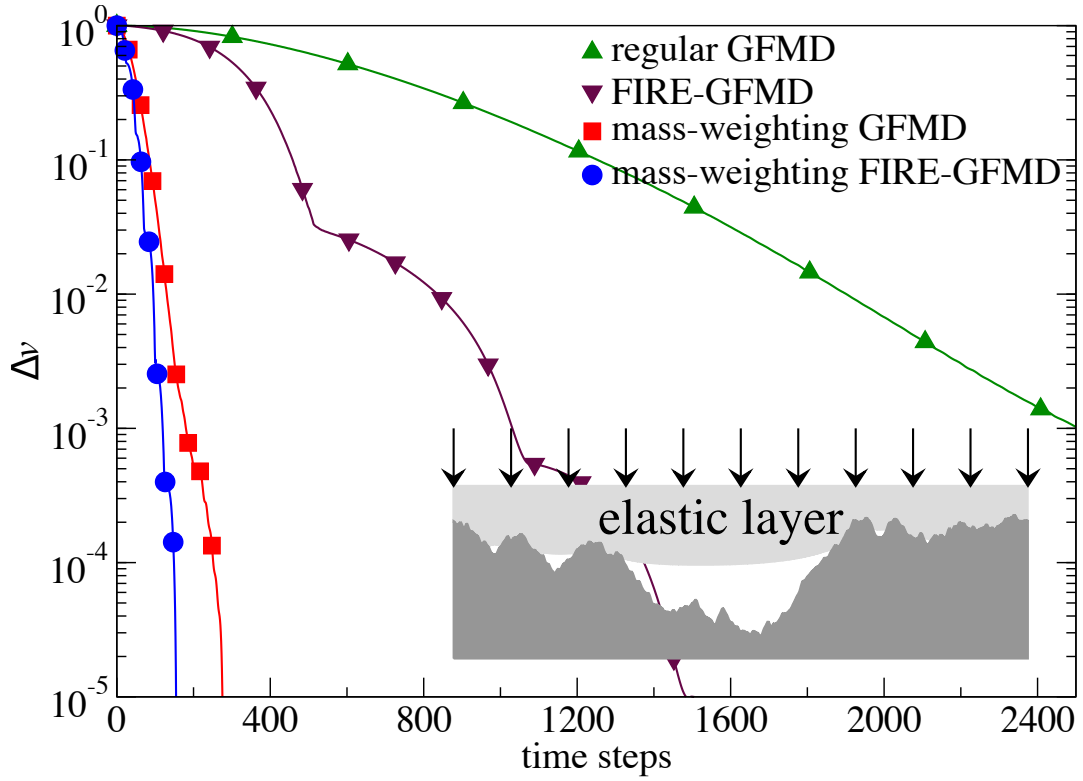

Figure 2.7: As in Fig.2.4, however, for a randomly rough indenter. The default substrate roughness is set up as follows: we use a Hurst exponent of $H = 0.8$. There is no roll-off so that the system size corresponds to the long wavelength cutoff λ_l. The short wavelength cutoff is chosen to be $\lambda_\mathrm{s} = 0.01 L_x$. By default, the system is discretized into $N_x = 1024$ grid points.

The reason is that the number of discretization points for the contact mechanics challenge is greater. Additionally, the range of adhesion of the contact-mechanics-challenge problem is much shorter. FIRE GFMD needs 2000 iterations to reach the stress to the same accuracy as Bugnicourt. In this case, FIRE GFMD turns out to slightly outperform the CGM by Bugnicourt. This improvement may not be strong enough to motivate the replacement of a working CG-based minimization in a code with a new FIRE method. However, when designing new code, the FIRE method appears to be a better choice, because it is much easier to implement.

2.4 Conclusion

In this chapter, we investigated the performance of various minimization methods, including FIRE method, the mass-weighting method and mass-weighting FIRE

method, on classical BVPs within the framework of GFMD. Two contact mechanics problems were conducted as benchmarks to illustrate the extension of FIRE. In regular GFMD, a critical damped dynamics for each surface Fourier mode was set up to minimize the total potential energy. It allows for the possibility of short-range adhesion, and even shorter-range repulsion, and nonoverlap constraints. Since GFMD is a MD technique, introducing FIRE to GFMD would not require much effort.

It is demonstrated that FIRE can successfully accelerate a regular GFMD simulation resulting in a remarkable speedup of one order of magnitude for typical system sizes compared to regular GFMD and even larger speedups for larger systems. It is also possible to combine FIRE with other minimization methods in a straightforward fashion in the framework of GFMD, such as an effective choice for the inertia of each mode. This is known as a mass-weighting method, which induces a narrow distribution of intrinsic frequencies whereby the number of required sweeps to relax the system no longer increases substantially with system size. Even though the relative speedup due to FIRE in such mass-weighted GFMD approach is not overwhelming, a factor of two in efficiency can still be useful for pushing the boundaries of large-scale problems on massive parallel supercomputers.

The successful implementation also indicates that the FIRE algorithm could also benefit finite-element method, or generally, any engineering simulation that could result in the solution of boundary value problems. Experience from atomic-scale applications shows that FIRE is always competitive with much more complex mathematical optimization algorithms [47, 82, 83] (such as quasi-Newton methods) and sometimes FIRE can even be superior [84].

Chapter 3

Thermal Hertzian contact mechanics

This chapter attempts to study how thermal fluctuations affect the mean force F (per unit area) between surfaces as a function of their interfacial separation, or, gap g. Furthermore, it is also interesting to study if this relation could be applied to classical Hertzian contact theory. Towards this end, we attempt to construct the effective surface interactions. Because a hard-wall constraint is the most commonly used interaction between surfaces, we restrict our attention to the effect of thermal fluctuations on hard-wall constraints. Since atoms fluctuate about their equilibrium sites in solids, thermal fluctuations automatically make repulsion effectively adopt a finite range.

The purpose of this chapter is to quantify thermal effects, namely, the relation between the interfacial separation and the mean force obtained for flat walls. After that, an extension of this relation to a Hertzian contact would be conducted to ascertain its applicability. Another purpose of this chapter is to identify an analytical expression for the thermal corrections to the load-displacement relation in a Hertzian contact.

In the remaining part of this chapter, the contact problem and the interaction between surfaces are designed in Sec. 5.1. The numerical technique is introduced in Sec. 3.2, while the theory is outlined in Sec. 3.3. Numerical and theoretical results are presented in Sec. 3.4 and conclusions are drawn in the final Sec. 5.4.

3.1 Model design

3.1.1 Treatment of elasticity and thermal displacement

In this study, the elastic body is designed as initially flat, semi-infinite and linearly elastic. The rigid substrate is fixed in space and the elastic body is moving from above, while the contact is defined as friction- and adhesionless. The indenter, as designed in this study, is either perfectly flat, *i.e.*, $h(\mathbf{r}) = 0$, or parabola, in which case $h(\mathbf{r}) = -r^2/(2\,R_\mathrm{c})$, where R_c is the radius of curvature. In order to reduce finite-size effects and to simplify both analytical and numerical treatments, periodic boundary conditions are assumed by default within the quadratic, interfacial plane.

The elastic surface is subjected not only to an external load per particle, l, squeezing it down against the indenter but also to thermal fluctuations, as they would occur in thermal equilibrium at a finite temperature T. Additionally, the small slope approximation is applied to the counterface, therefore, the shear displacement could be neglected.

In this case, the elastic energy of the deformed solid (semi-infinite thickness) can be expressed as

$$U_\mathrm{ela}[u(\mathbf{r})] = \frac{E^* A}{4} \sum_{\mathbf{q}} q \, |\tilde{u}(\mathbf{q})|^2 \,. \tag{3.1}$$

Here, $u(\mathbf{r})$ states the z-coordinate of the elastic solid's bottom surface as a function of the in-plane coordinate $\mathbf{r} = (x, y)$. E^* is the contact modulus, A the (projected) interfacial area, $\mathbf{q}$ an in-plane wave vector, and q its magnitude.

$$\tilde{u}(\mathbf{q}) = \frac{1}{A} \int d^2r \, e^{-i\mathbf{q}\cdot\mathbf{r}} u(\mathbf{r}) \tag{3.2}$$

denotes the Fourier transform of $u(\mathbf{r})$. The short-hand notation $u_0 = \tilde{u}(\mathbf{q} = 0)$ will be used for the center-of-mass coordinate.

For a flat indenter, only u_0 will be used to denote the mean distance, or gap, between indenter and the solid surface. Here, we define the displacement d as a function of temperature and load according to

$$d(T, L) \equiv h_\mathrm{ind}(r = 0) - \langle u(T, L, r \to \infty) \rangle, \tag{3.3}$$

where $\langle u(T, L, r \to \infty) \rangle$ is the thermal expectation value that the field $u(\mathbf{r})$ would have (infinitely) far away from the top if the simulation cell were infinitely large.

In this chapter, we are interested mostly in the temperature-induced reductions of d, *i.e.*, in the term d_T defined in the expression

$$d = d_0 - d_T, \tag{3.4}$$

where d_0 indicates the displacement for an athermal Hertzian indenter at a given load. We compute d_T through the following approximation

$$d_T \approx \langle u(T, L, \mathbf{r}_X) \rangle - u(0, L, \mathbf{r}_X), \tag{3.5}$$

where $\mathbf{r}_X$ is the most distant point from the center of the Hertzian indenter.

3.1.2 Treatment of interaction

As in the reminder of this thesis, the interaction is fully defined by the integral of the surface energy density $\gamma(g)$ over the surface, which is a function of the local interfacial separation or gap, $g(\mathbf{r}) = u(\mathbf{r}) - h(\mathbf{r})$, between the surfaces. It reads

$$U_{\text{int}} = \int_A d^2r \, \gamma\{g(\mathbf{r})\}, \tag{3.6}$$

If the elastic energy is given explicitly, the probability of a certain configuration to occur would be proportional to the Boltzmann factor, *i.e.*,

$$\Pr[u(\mathbf{r})] \propto e^{-\beta(U_{\text{ela}} + U_{\text{int}})} \tag{3.7}$$

where $\beta = 1/k_B T$ is the inverse thermal energy.

This section will introduce a variety of interaction strategies that will be used in this chapter.

Non-overlap constraint

The non-overlap constraint, or hard-wall constraint is applied for most traditional contact problems, in which case the surface energy density is defined as

$$\gamma(g) = \begin{cases} \infty & \text{if } g < 0 \\ 0 & \text{else}\,. \end{cases} \tag{3.8}$$

This function indicates that the rigid indenter is not allowed to penetrate the elastic sheet.

In this study, we will repeatedly go back and forth between continuous and discrete descriptions of displacement fields. For the discrete description, the elastic solid is split into individual atoms, which are arranged on a square lattice with the lattice constant Δa. Transitions between these two representations in real space can be achieved with the substitutions

$$\sum_n ... \leftrightarrow \frac{1}{\Delta a^2} \int_A d^2r..., \tag{3.9}$$

while transitions between summations and integrals in the Fourier space can be achieved with

$$\sum_{\mathbf{q}} ... \leftrightarrow \frac{A}{(2\pi)^2} \int d^2q... \,. \tag{3.10}$$

To simplify the analytical evaluation of integrals, the square Brillouin zone (BZ) of the surface will be approximated with a circular domain. In this case, the upper cutoff for q is chosen to be $q_{\max} = \sqrt{4\pi}/\Delta a$ as to conserve the number of degrees of freedom with respect to the original BZ.

Effective hard-wall potentials

Non-overlap constraints can be applied in GFMD simulations if the thermal effect is neglected. The basic idea of this constraint is sketched as follows: elastic sheet is split into discrete atoms and pressed against the rigid sheet, once the atoms penetrate the rigid solid, they go back onto the surface. This scheme no longer works at finite temperature, in which case the thermal fluctuation is considered. It violates the fluctuation-dissipation theorem (FDT) because the damping that is

effectively imposed by this algorithm, is not compensated by a conjugate random force.

In order to apply non-overlap constraint when thermal fluctuations are considered, a controlled fashion to violate of the rigid sheet should be allowed. The resulting procedure in terms of surface energy density function is given as below.

$$\gamma(g) = \frac{\kappa_{\mathrm{o}}\, E^*\, \Delta a}{n} \left(\frac{-g}{\Delta a}\right)^n \Theta(-g) \tag{3.11}$$

where Θ is the Heavyside step function, κ_{o} is the hard-wall stiffness and n is a dimensionless parameter.

Although this procedure allows the atom penetrate the rigid sheet, it is designed to eliminate the penetration as quickly as possible. Towards this end, good numbers for the exponent n and the dimensionless hard-wall stiffness κ_{o} need to be chosen. In order for the effective hard-wall potential to have a minimal effect on Δt, the (non-negative) exponent n should be as small as possible. However, we would like the force to be a continuous function, for reasons explained at length in any better text book on molecular dynamics [72, 73]. While these arguments can be somewhat academic when the discontinuities are small, we are going to send κ_{o} to large numbers resulting in significant force discontinuities. Thus, n must be chosen greater equal two. This appears to make $n = 2$ the optimal choice.

Regarding the choice of κ_{o} when Δt and n are determined, we should keep in mind that we do not need extremely accurate dynamics in the "forbidden" domain. The main purpose of this energy density function is to leave the "forbidden" zone as quickly as possible. On the other hand, the stiffness should be designed less than a critical value above which the energy conservation is not satisfied for athermal simulation even when Verlet algorithm is used. For Verlet, the critical time step for a harmonic oscillator is $\Delta t_{\mathrm{c}} = T/\pi$, where T is the oscillator period, *i.e.*, for $\Delta t < \Delta t_{\mathrm{c}}$, the trajectory may be inaccurate, but the energy is conserved (except for round-off errors). This can be achieved by setting the overlap stiffness to

$$k_{\mathrm{o}} = \nu_{\mathrm{o}}\, \pi^2\, \frac{m}{dt^2} - k_{\mathrm{s}}, \tag{3.12}$$

where $k_{\mathrm{s}} = \Delta u^2/(k_B T)$, while m is the inertia of the considered degree of freedom. ν_{o} is a numerical factor, which must be chosen less than unity. At and above the critical value of $\nu_{\mathrm{o}} = 1$, energy conservation would be no longer obeyed in the

absence of a thermostat. At the same time, dynamics but also static distribution functions are very inaccurate, even if a thermostat prevents the system from blowing up.

The optimum value for k_o certainly depends on the specific investigated problem. However, the analysis of simple models can provide useful preliminary estimates. This will be done in Sec. 3.1.2.

Approximate collision rules

Another technique to apply hard-wall constraint with consideration of thermal fluctuation is to use approximate collision rules and control the error of the imprecision with the time step. The implementation is summarized as follows: Δt is fixed in simulation, atom velocity changes sign if it violates the non-overlap constraint. The procedure in terms of pseudo code is sketched as follows, in which case the constraint is ignored.

```
if (z violates constraint) then
   z = 2z_constr-z
   v_z = -v_z            (velocity Verlet)
   z_old = 2z_constr-z_old (standard Verlet)
end if
```

In a certain GFMD simulation, in which case all observables are propagated in Fourier space, the following extra cost would have to be achieved: not only the current positions, but also the old positions in real space will have to be stored in memory for the purpose of the velocity calculation. Additionally, two extra Fourier transforms on old positions will have to be requested, which would double the number of the most expensive function calls. Since this approach appears to show similar scaling with Δt in simple models as effective hard-wall repulsion, see Sec. 3.1.2 for more details, we did not apply this procedure in this study in case of time consuming.

Numerical case studies

To investigate the performance of these two approaches to mimic hard-wall constraint, we study the following single harmonic oscillator problem: thermal fluctuations are applied to an originally free harmonic oscillator, the resulting variance is Δu^2. Additionally, this harmonic oscillator is then constrained to have no negative deflections from its mechanical equilibrium site.

Essentially, the harmonic oscillator problem described above requires that k_BT, k, and m should be chosen such that the Δu^2 is unity (in units of k_BT/k). The default time step that we use for the free oscillator is $2\pi/30$, *i.e.*, 30 time steps per period. The damping coefficient is chosen to be $\gamma = 1$, whereby the free harmonic oscillator is slightly under-damped. Results for the convergence of how the estimate for the mean displacement u_0 approaches the exact value with decreasing time step Δt are shown in Fig. 3.1.

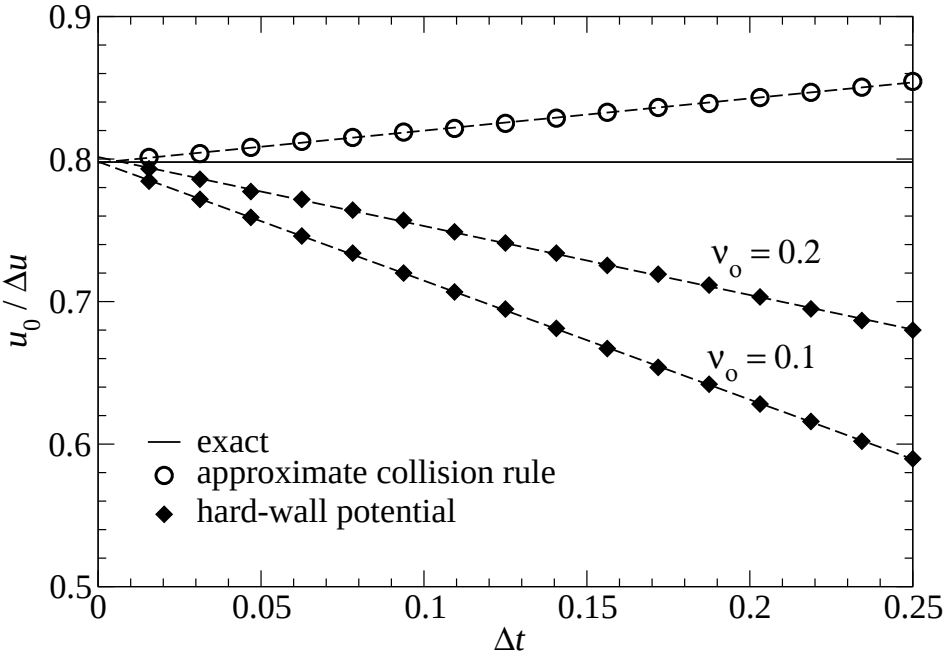

Figure 3.1: Mean displacement u_0 in units of Δu as a function of time steps. Different symbols represent different hard-wall approximation, open circles indicates approximate collision rules and closed diamonds the harmonic effective hard-wall potential. Dash lines show linear fits, while solid line shows the analytical solution.

As shown in this figure, the approximate collision rules turns out to be better than the approximate hard-wall interactions at a given value of Δt. However, u_0 has leading-order corrections of order Δt in both approaches. The error for effective hard-wall potential is less than 1% with the choice of $\nu_o = 0.1$, which is rigorous for most simulations. Additionally, simulations must be conducted at two different values of Δt for the purpose of a meaningful extrapolation. Considering that the double times of Fourier transform when using approximate collision ruls would result the time consuming problem, we decided to apply the effective hard-wall interaction for the full contact mechanics simulations.

3.2 Thermal GFMD

GFMD is a boundary element method allowing us to effectively solve the elastic response of a linearly elastic solid to boundary conditions [7, 38, 75]. The elastic surface displacement field is split into discrete atoms, thus these atoms could reflect the dynamic degrees of freedom. Elastic interactions are applied on the surface in terms of elastic Green's function. In this study, we consider a linear elastic solid with semi-infinite thickness frictionlessly contacts with rigid counterface. The equation to be solved in GFMD is

$$m_q \ddot{\tilde{u}}(\mathbf{q}) + \eta_q \dot{\tilde{u}}(\mathbf{q}) + \frac{q\,E^*}{2}\,\tilde{u}(\mathbf{q}) = \tilde{F}(\mathbf{q},t), \tag{3.13}$$

where $\tilde{F}(\mathbf{q},t)$ is the Fourier transform of all external forces acting on the surface atoms. The terms m_q and η_q represent inertia and damping coefficients of different surface modes, which may depend on the wave vector. In this study, we focus on isotropic systems, therefore, both m_q and η_q only depend on the magnitude q but not on the direction of $\mathbf{q}$.

The thermal fluctuations can be explained as random forces, which have to satisfy the FDT [85], in which case the random forces must obey a zero mean, and the second moments must satisfy,

$$\langle \Gamma(\mathbf{q},t)\Gamma(\mathbf{q}',t')\rangle = 2\,\eta_{\mathbf{q}}\,k_B T\,\delta_{\mathbf{q},\mathbf{q}'}\,\delta(t-t'), \tag{3.14}$$

assuming discrete atoms, finite domains but continuous times. Here, $\delta(\bullet)$ is the Dirac delta function, which can be replaced with $\delta_{t,t'}/\Delta t$ in a molecular dynamics (MD) simulation, in which the time t is discretized into steps of size Δt.

At this point, GFMD is only used to generate the correct distribution of configurations, which—in a classical system—does not depend on the choice of inertia. In this case, the m_q can be chosen at will as long as the stable configurations can be reached. In standard GFMD simulation, m_q is assumed to be constant, in which case identical simulations are obtained as if the Newton's equation were propagated in real space. However, a realistic dynamics would be produced if m_q are chosen proportional to $1/q$. In fact, realistic dynamics require the treatment of damping and random noise to have "memory", as discussed in Ref. [86]. When being interested in efficient dynamics, which are useful to identify the local minimum potential energy, or stable equilibrium configuration quickly, the m_q are better chosen proportionally to the stiffness at wave vector q, which means, small value of m_q for long-wavelength modes and large value of m_q for short-wavelength modes [75]. In this context, it is also worth mentioning that significant progress has been made recently on GFMD to properly reflect not only true (rather than efficient) dynamics of crystalline solids [87] but also for truly visco-elastic materials with broad relaxation functions [41].

3.3 Theory

In this section, we investigate the analytical expression for the thermal expectation value of an interfacial force per atom $f(u_0)$ as a function of their mean separation u_0 in the case of hard-wall potential. Towards this end, a partition function $Z(N, \beta, u_0)$ of a fluctuating surface in front of a wall is defined, therefore, the free energy could be determined according to $\mathcal{F}(k_BT, u_0) = -k_BT \ln Z(\beta, u_0)$. The mean force between hard wall and elastic surface can then be calculated from

$$f = -\frac{1}{N}\frac{\partial \mathcal{F}(N, k_BT, u_0)}{\partial u_0}. \tag{3.15}$$

Minor errors in the treatment presented below appear in numerical coefficients that result, for example, by having approximated the Brillouin zone of a square with a sphere, or, by having replaced a discrete set of wave vectors (finite system)

with a continuous set (infinitely large system). However, these and related approximations are controlled, because errors resulting from them can be estimated and they could even be corrected systematically.

3.3.1 The statistical mechanics of a free surface

We start our theoretical study with the free surface, which is the reference state and the easiest case to investigate. In this approach, the variance of atomic displacement caused by thermal fluctuation is an important quantity. In the case of fixed center-of-mass mode, the variance is defined as

$$\Delta u^2 \equiv \left\langle \{u(\mathbf{r}) - \tilde{u}(0)\}^2 \right\rangle . \tag{3.16}$$

The variance could be computed in a straightforward fashion if we make Fourier transform of the displacement, which reads

$$\begin{aligned} \Delta u^2 &= \sum_{\mathbf{q}'} \left\langle |\tilde{u}(\mathbf{q}')|^2 \right\rangle && (3.17)\\ &\approx \frac{A}{(2\pi)^2} \int d^2q \frac{2\, k_B T}{q E^* A} && (3.18)\\ &\approx \frac{2}{\sqrt{\pi}} \frac{k_B T}{E^* \Delta a}, && (3.19) \end{aligned}$$

where we made use of equipartition for harmonic modes, see also Eq. (3.28).

The prefactor $2/\sqrt{\pi} \approx 1.1284$ turns out to be very close to unity. However, in a quantitative theory, we wish to know and perhaps to understand its precise value. Towards this end, we assume the BZ to be square in real space with N atoms and a summation based on this assumption is conducted. It shows that Δu^2 can be evaluated by

$$\Delta u^2 = \left(1.1222 - \frac{1.24}{\sqrt{N}}\right) \frac{k_B T}{E^* \Delta a}, \tag{3.20}$$

if $\sqrt{N} > 512$ to more than three digits accuracy. This result is fairly close to the analytical result based on a BZ, which is approximated as sphere.

Eq. (3.19) reveals that the fluctuations are dominated by the small scales. In the case of an Einstein solid, in which each surface atom is an independent harmonic oscillator with identical stiffness $k_{\mathrm{E}} = k_B T / \{(N-1)\, \Delta u^2\}$. In reality, *i.e.*,

in less than infinite dimensions, there is always a correlation of thermal height fluctuations.

In this case, the following question remains: what is the distance over which height fluctuations are correlated? Towards this end, we calculate the thermal displacement autocorrelation function (ACF) $C_{uu}(r)$. It can be defined and evaluated to obey:

$$
\begin{aligned}
C_{uu}(\Delta r) &= \langle u(\mathbf{r})\, u(\mathbf{r}+\Delta\mathbf{r})\rangle && (3.21)\\
&\approx \frac{1}{2\pi^2}\frac{k_B T}{q E^*}\int_0^{\sqrt{4\pi}/\Delta a} dq \int_0^{2\pi} d\varphi\, e^{iqr\cos\varphi} && (3.22)\\
&= \frac{1}{\pi}\frac{k_B T}{r q E^*}\int_0^{\sqrt{4\pi}r/\Delta a} d(qr) J_0(qr) && (3.23)\\
&= \frac{2\,k_B T}{q E^*}\frac{\sqrt{4\pi}\,r}{\Delta a}\,{}_1F_2\left(\frac{1}{2};1,\frac{3}{2};\frac{-\pi\, r^2}{\Delta a^2}\right) && (3.24)\\
&\approx \begin{cases} \frac{2\,k_B T}{\sqrt{\pi}\,E^*\,\Delta a}+\mathcal{O}(r^2) & \text{for } r\to 0\\ k_B T/(\pi\, q\, E^*\, r) & \text{for } r\to\infty, \end{cases} && (3.25)
\end{aligned}
$$

in this expression, $J_0(x)$ represents the Bessel function of the first kind and ${}_1F_2(...)$ a generalized hypergeometric function. The analytical result of ACF shows Helmholtz ringing at intermediate values of r. This leads to the theoretical solution of little practical use, except in the two limiting cases $r \to 0$ and $r \to \infty$. Generally, Helmholtz ringing is the result of feature, such as abrupt cutoffs in the wave vector domain. However, even using exact expectation values of $|\tilde{u}(\mathbf{q})|^2$ for a square BZ and extending the ACF to continuous limit between the lattice positions, the Helmholtz ringing remains. The validity of these claims is demonstrated in Fig. 3.2.

One could generalize the $C_{uu}(r)$ to a continuous function by constructing the simplest expression with the correct limit behaviors, which reads

$$
C_{uu}(r) \approx \frac{2}{\sqrt{\pi}}\frac{k_B T}{E^*}\frac{1}{(\Delta a^2+4\pi\, r^2)^{1/2}}. \qquad (3.26)
$$

As shown in Fig. 3.2, this asymptotic function is acceptable at a intermediate domain where $r = \Delta a$ and the errors remain less than 5% in the limit of large N for larger r. Although numerical results presented in Fig. 3.2 include data for $\mathbf{r}$ parallel to $[1, 0]$, it is demonstrated that other direction, such as $[1, 1]$ direction could also get similar results.

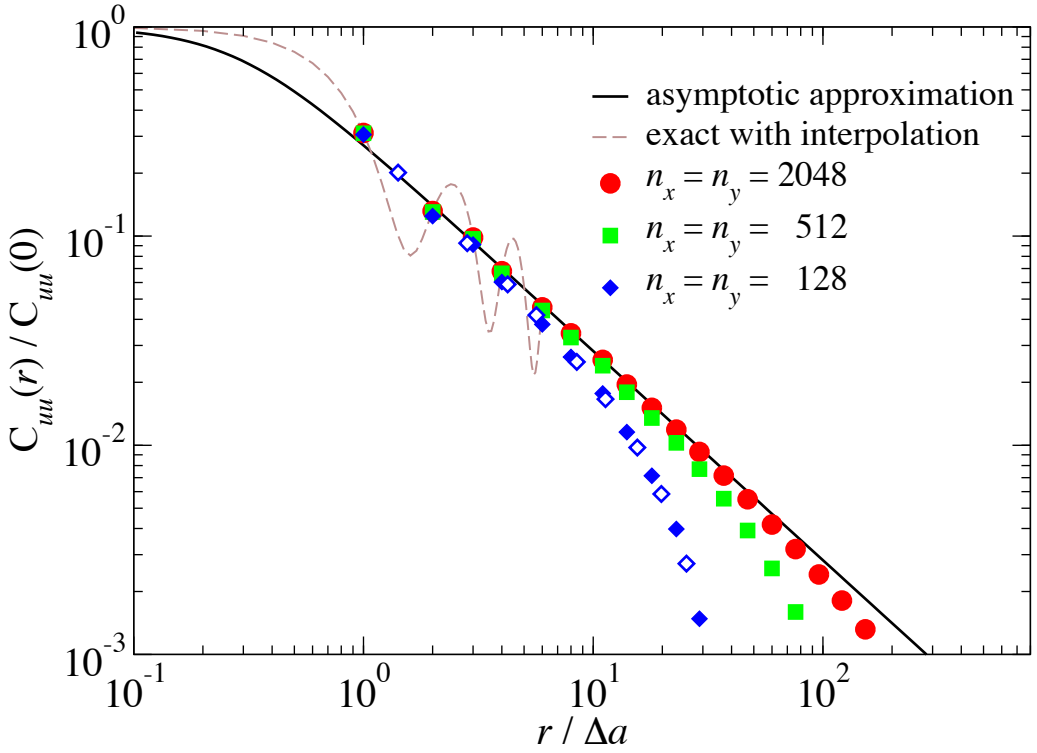

Figure 3.2: The ACF $C_{uu}(r)/C_{uu}(0)$ as a function of $r/\Delta a$. Closed color symbols represent numerical results along the [10] direction for different system sizes, while open symbols refer to the numerical result along the [11] direction. The solid line represents the asymptotic approximation presented in Eq. (3.26), while the dashed line the exact correlation function along the [10] direction with interpolation between non-lattice sites.

Another property should be noticed is that the asymptotic function has decayed to roughly 30% of its maximum value at the nearest-neighbour distance. This indicates that the displacements of neighboring lattice sites are substantially uncorrelated.

The partition function of a free surface is defined as

$$Z_{\mathrm{fs}}(\beta) = \prod_{\mathbf{q}} \frac{\lambda_q}{\sqrt{2\pi\Delta u^2(q)}} \tag{3.27}$$

with

$$\Delta u^2(q) = \frac{2\,k_B T}{q\,E^* A}. \tag{3.28}$$

$\lambda_q = h/\sqrt{2\,m_q\,k_B T}$ represents the thermal de Broglie wavelength of a surface mode. It indicates the ideal-gas contribution of the momenta conjugate to $\tilde{u}(\mathbf{q})$ to the partition function. The intention of including λ_q into the calculation is to

satisfy the partition function dimensionless, as long as E^* is small compared to the external pressure and temperature kept fixed. At this point, a precise choice of m_q is not necessary, even though it might be an interesting issue in itself.

If the solid is simplified to an Einstein solid, the partition function can be given as

$$Z_{\mathrm{mf}}(\beta) = \left(\frac{\lambda_{\mathrm{mf}}}{\sqrt{2\pi\Delta u^2}} \right)^N , \tag{3.29}$$

where Δu was sketeched above and λ_{mf} represents a mean-field de Broglie wavelength.

3.3.2 Interaction of a thermal, elastic surface with a flat wall

In this section, the statistical mechanics of an initially flat, linearly elastic surface in front of a flat, rigid wall is studied. The purpose is to deduce the expression of mean force in a straightforward fashion. We conducted various mean-field approaches for this intention. The theoretical results appears to be quite accurate in different asymptotic limits of the full problem.

First mean-field approximation

The Einstein solid, which was introduced in Sec. 3.3.1, is the most straightforward way to thermal contact problem. As a result, a degree of freedom is a hybrid of an atom in real space and a delocalized, ideal sine wave. Additionally, we assume that the elastic energy of an individual atom follows

$$v_{\mathrm{ela}}^{\mathrm{mf}}(u) = \frac{k_B T}{2\,\Delta u^2}\, u^2. \tag{3.30}$$

According to FDT, the expectation value of u should remain zero, towards this end, we assume that the interaction energy with a counterface placed at a distance u_0 from the atom's mean position is given by

$$v_{\mathrm{sub}}^{\mathrm{mf}}(u) = \frac{\Delta a^2}{2\pi} \int_0^{2\pi} d\varphi\, \gamma(u_0 + u\cos\varphi). \tag{3.31}$$

This expression indicates that an oscillation of an atom leads to an undulation. If so, u_0 automatically corresponds to the atom's mean position.

The excess free energy per particle $\Delta\mathcal{F}/N$ for a fixed center-of-mass position satisfies

$$e^{-\beta\mathcal{F}/N} = \frac{1}{\sqrt{2\pi\Delta u^2}}\int_{-\infty}^{\infty} du\; e^{-\beta\{v_{\rm ela}^{\rm mf}(u)+v_{\rm sub}^{\rm mf}(u)\}}, \tag{3.32}$$

where the term "excess" refers to the change of the free energy relative to that of a free surface. For hard-wall interactions, the integral in Eq. (3.32) can be evaluated to be

$$\begin{aligned} e^{-\beta\mathcal{F}/N} &= \frac{1}{\sqrt{2\pi\Delta u^2}}\int_{-u_0}^{u_0} du\; e^{-\beta v_{\rm ela}(u)} \\ &= \mathrm{erf}\left(\frac{u_0}{\sqrt{2}\Delta u}\right). \end{aligned} \tag{3.33}$$

Hence,

$$\frac{\mathcal{F}}{N\,k_BT} = -\ln\left\{\mathrm{erf}\left(\frac{u_0}{\sqrt{2}\Delta u}\right)\right\} \tag{3.34}$$

$$\approx \begin{cases} -\ln\left(\sqrt{\frac{2}{\pi}}\,\frac{u_0}{\Delta u}\right) & \text{for } u_0 < \Delta u/2 \\ \frac{\Delta u}{\sqrt{\pi}u_0}\,e^{-u_0^2/(2\Delta u^2)} & \text{for } u_0 > 2\Delta u. \end{cases} \tag{3.35}$$

The derivative of Eq. (3.34) leads to the force expression from this first mean-field approximation, which reads

$$f_{\rm mf1}(u_0) = \sqrt{\frac{2}{\pi}}\,\frac{k_BT}{\Delta u}\,\frac{\exp\{-u_0^2/(2\Delta u^2)\}}{\mathrm{erf}\{\mathrm{u}_0/(\sqrt{2}\Delta\mathrm{u})\}}. \tag{3.36}$$

Second mean-field approximation

Another approach to thermal contact problem is to introduce an external force f divided by the thermal energy instead of the interaction force, such that u adopts the desired value of u_0. In this case, the possibility of a displacement u to occur reads

$$\Pr(u) \propto e^{-(u-u_0)^2/(2\Delta u^2)-\beta f(u-u_0)}\Theta(u), \tag{3.37}$$

where f should be well chosen such that $\langle u\rangle = u_0$, in which case the equilibrium lattice position satisfies $u_{\rm eq} = u_0 + \beta f\Delta u^2$. In this case, the restoring force in the spring equals to zero. The requirement $\langle u\rangle = u_0$ automatically leads to the

following self-consistent equation for f:

$$\beta\, f\, \Delta u = \sqrt{\frac{2}{\pi}}\, \frac{\exp\left\{-\frac{(\beta\, f\, \Delta u^2 - u_0)^2}{2\Delta u^2}\right\}}{1 - \mathrm{erf}\left(\frac{\beta\, f\, \Delta u^2 - u_0}{\sqrt{2}\, \Delta u}\right)}. \tag{3.38}$$

This approach leads to similar results for the f at small u_0 as the first mean-field estimation. However, the predicted force appears to be half that of the first mean-field approach for large u_0.

Probabilistic approach

The third approach is to define the excess free energy of an elastic body in front of a hard-wall by a path integral, which reads

$$e^{-\beta \mathcal{F}(u_0')} = \frac{1}{Z_A} \int \mathcal{D}[u(\mathbf{r})]\ \delta\left(u_0' - u_0\right)\ e^{-\beta\, v_{\mathrm{tot}}[u(\mathbf{r})]}, \tag{3.39}$$

where $\mathcal{D}[u(\mathbf{r})]$ denotes an integral over all possible displacement realizations and

$$Z_A = \int \mathcal{D}[u(\mathbf{r})]\ \ \delta\left(u_0 - u_0'\right)\ e^{-\beta\, v_{\mathrm{ela}}[u(\mathbf{r})]}. \tag{3.40}$$

Eq. (3.39) can be explained as follows: the relative number of configurations that are produced with the thermal equilibrium distribution of a free surface (fs), whose maximum displacement is less than u_0, *i.e.*,

$$e^{-\beta \mathcal{F}(u_0)} = \left\langle \Pr(u_{\max} < u_0) \right\rangle_{\mathrm{fs}}, \tag{3.41}$$

This interpretation motivated us to solve the following probability problem: what is the possibility of $N' = N\Delta a^2/\Delta A_{\mathrm{c}}$ independent Gaussian random number satisfies $\langle u \rangle = 0$ and $\Delta u^2 < u_0$? Here ΔA_{c} is the correlation area for the displacements.

The distribution of $u_{\max} = \max\{u(\mathbf{r})\}$ converges to the Gumbel distribution [88] as long as the Gaussian random number N' is large enough, which reads

$$\Pr(u_{\max}) = \frac{1}{\beta_{\mathrm{gev}}}\, e^{-\left(e^{-z}\right)} \tag{3.42}$$

with

$$z = \frac{u_{\max} - \mu_{\mathrm{gev}}}{\beta_{\mathrm{gev}}}, \tag{3.43}$$

where μ_{gev} is the mode of the Gumbel distribution, *i.e.*, the most likely value for $u_{\max}$ to occur, and β_{gev} a parameter determining the shape of the distribution. For a normal Gaussian distribution $\Phi_{\mathrm{G}}(u/\Delta u)$, they are given by

$$\frac{\mu_{\mathrm{gev}}}{\Delta u} = \sqrt{2}\,\mathrm{erf}^{-1}\left(1-\frac{2}{N'}\right) \tag{3.44}$$

$$\frac{\beta_{\mathrm{gev}}}{\Delta u} = \frac{1}{N'\cdot\Phi_{\mathrm{G}}(\mu_{\mathrm{gev}}/\Delta u)} \tag{3.45}$$

in the limit of large N'. Here $\mathrm{erf}^{-1}(...)$ stands for the inverse function of the error function [88].

As shown in Fig. 3.3, the distribution of $u_{\max}$ one time produced with GFMD and another time by taking N' independent random numbers are roughly identical, and both of them are almost dead-on the Gumbel distribution.

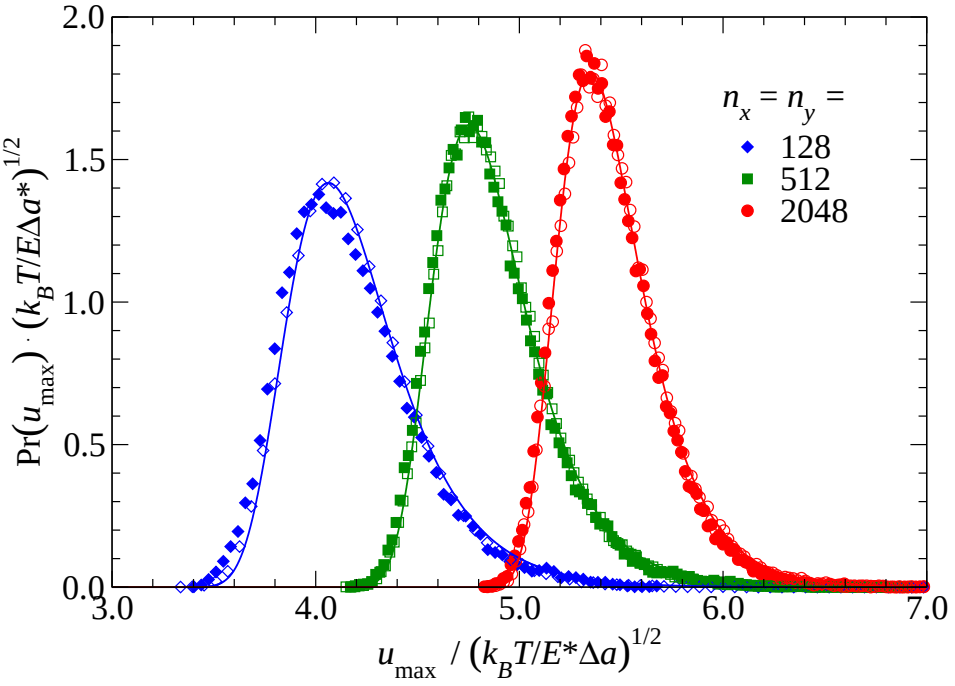

Figure 3.3: Distribution of maximum displacements for different system sizes. Closed symbols represent the data obtained from GFMD simulation, while open symbols indicate the data obtained from $N' = 0.92\,N$ independent random numbers of mean zero and variance Δu. Solid lines represent the Gumbel distributions.

Rather than relying on the Gumbel distribution, one might as well write down the exact probability of one positive Gaussian random variable (grv) to be less than u_0 and take the result into the $N'/2$-th power. (On average, there are $N'/2$ positive grv's, whose value may not exceed u_0. The negative grv's are irrelevant with respect to the violation of the violation of the non-overlap constraint.) In this approximation,

$$\Pr(u_{\max} < u_0) = \left\{ \operatorname{erf}\left(\frac{u_0}{\sqrt{2}\sigma} \right) \right\}^{N'/2}. \tag{3.46}$$

and therefore

$$\Delta\mathcal{F} = -\frac{N' k_B T}{2} \ln \left\{ \operatorname{erf}\left(\frac{u_0}{\sqrt{2}\Delta u} \right) \right\}. \tag{3.47}$$

This approach works for large separations, in which case $u_0/\Delta u \gg 1$. One should notice that this expression is similar to the first mean-field case, except for the prefactor, which is reduced by a factor of two while N is replaced with N'.

3.3.3 Thermal Hertzian contacts

Preliminary considerations

All variables needed to define a thermal Hertzian contact problem are listed as follows: the radius of curvature of the rigid indenter R_c, grid distance Δa, contact modulus E^*, external load L, and thermal energy $k_B T$. Therefore, the thermal displacement d_T should be identified by a function of variables listed above. Specifically, at small temperature, the leading-order approximation of the relative displacement d_T/d_0 can be expected to depend on powers of the variables declared above, which reads

$$\frac{d_T}{d_0} \propto \left(\frac{R_\mathrm{c}}{\Delta a} \right)^{\alpha} \left(\frac{E^* R_\mathrm{c}^2}{L} \right)^{\beta} \left(\frac{k_B T}{E^* R_\mathrm{c}^3} \right)^{\gamma}, \tag{3.48}$$

where d_0 represents the displacement of a typical athermal Hertzian indenter at external load L. E^* and R_c are used to define the units of pressure and length, respectively. Furthermore, the exponents should satisfy the following rule, which is deduced with the help of dimensional analysis.

$$\alpha + 3\beta - 5\gamma = 0 \tag{3.49}$$

The sum rule Eq. (3.49) holds generally for temperature ranging from low to high value.

Low-temperature approximation

Low-temperature corresponds to weak thermal fluctuations, in which case the stress profile of a typical Hertzian contact problem is expected to be similar to that of the athermal Hertzian contact problem except for a slightly deviation. This deviation then could be predicted as a constant shift d_T according to the perturbative assumption. In this case, the thermal Hertzian gap could be evaluated with $g(r) = g_{\mathrm{H}}(r) + d_T$, where $g_{\mathrm{H}}(r)$ is the Hertzian gap for athermal case. Considering that the dominant contribution to thermal energy are located in the original contact domain, the thermal energy per atom could be approximated as

$$e_T = -d_T\, L + \frac{1}{\Delta a^2} \int d^2 r\, \mathcal{F}_{\mathrm{pa}} \left\{ g_{\mathrm{H}}(r) + d_T \right\} \tag{3.50}$$

$$\approx -d_T\, L + \frac{2\pi}{\Delta a^2} \int_0^{\mathrm{a_c}} dr\, r\, \mathcal{F}_{\mathrm{pa}}(d_T), \tag{3.51}$$

where $\mathcal{F}_{\mathrm{pa}} \equiv \mathcal{F}/N$ denotes the hard-wall, free-energy normalized to the atom. The thermal displacement d_T could be obtained by minimizing e_T over T, which leads to

$$L = \frac{\pi\, a_{\mathrm{c}}^2}{\Delta a^2}\, f(d_T) \tag{3.52}$$

$$\approx \frac{\pi\, a_{\mathrm{c}}^2}{\Delta a^2} \sqrt{\frac{2}{\pi}} \frac{k_B T}{\Delta u} \frac{\exp\left(-u_0^2/2\Delta u^2\right)}{\mathrm{erf}(\mathrm{u_0}/\sqrt{2}\Delta \mathrm{u})} \tag{3.53}$$

where the last approximation is only valid at small temperatures. Taylor expanding this last expression leads to

$$\frac{d_T}{d_0} \approx \frac{T}{T^*} \tag{3.54}$$

with

$$T^* = \frac{L\, \Delta a^2}{\pi\, k_B\, R_{\mathrm{c}}}. \tag{3.55}$$

High-temperature approximation

When the temperature is very high, the thermal displacement d_T is far beyond the original displacement d_0, so that the deformation of the elastic solid could

be neglected. In this case, we assume the displacement field is a constant, say, d_T, and the resulting individual forces can be summed up with a mean gap of $d_\mathrm{T} + r_n^2/(2R_\mathrm{c})$. The external load then could be approximated as

$$L \approx \frac{N'}{2\,N}\,\frac{1}{\Delta a^2}\int d^2r\, f_\mathrm{mf1}\left(d_T + \frac{r^2}{2R_\mathrm{c}}\right) \tag{3.56}$$

$$\approx L_0\,\frac{\Delta u}{d_T}\,e^{-d_T^2/(2\Delta u^2)} \tag{3.57}$$

with

$$L_0 = \sqrt{\frac{2}{\pi}}\frac{N'}{N}\,\frac{k_B T\,R_\mathrm{c}}{\Delta a^2}. \tag{3.58}$$

To solve Eq. (3.57), we introduce Lambert W function $W(x) \approx \ln x - \ln\ln x$ for $x \gg 1$. The thermal displacement in unit of Δu could be evaluated as

$$\frac{d_T}{\Delta u} \approx \sqrt{W\left(\frac{L_0^2}{L^2}\right)}. \tag{3.59}$$

3.4 Results and analysis

3.4.1 Flat indenter

We have introduced three different theoretical approaches to the thermal contact mechanics for a perfect flat-on-flat geometry in Sec. 3.3.2. In this section, we explore for which case these approaches are consistent with the numerical results obtained with thermal GFMD technique. In numerical simulation, we set contact modulus $E^* = 1$, grid distance $\Delta a = 1$, and consider different values of $u_0/\Delta u$.

As shown in Fig. 3.4, the first mean-field theory is consistent with GFMD data for small values of u_0, while the probabilistic approach appears to be consistent with GFMD data for large values of u_0. There is a smooth transition between these two limits, which could be matched by the second mean-field theory. However, as introduced in Sec. 3.3.2, there is no closed form expression to describe this transition. On the other hand, we noticed that these two limits have similar functional form and the transition is quite continuous. The limitation and property mentioned above motivated us to apply a switching function to approximate this transition, as presented in Fig. 3.4, this function matches the GFMD data ranging from small to large values of u_0 with maximum errors less than 10%.

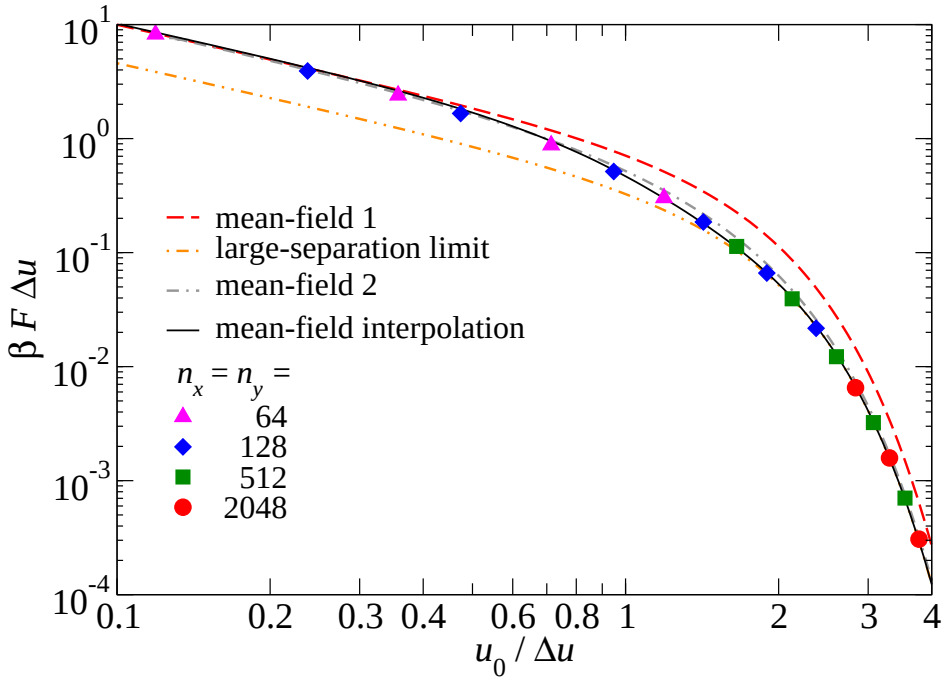

Figure 3.4: Dimensionless mean force $\beta f \Delta u$ as a function of normalized mean separation $u_0/\Delta u$, where Δu represents the height standard deviation of a surface atom in the absence of a counterface.

This switching function is given by

$$\mathcal{F}(u_0) \approx w_1(u_0)\mathcal{F}_{\mathrm{mfl}}(u_0) + w_2(u_0)\Delta\mathcal{F} \tag{3.60}$$

with the weighting functions

$$w_1(u_0) = \frac{1}{2}\left\{\frac{N'}{N} + \left(2 - \frac{N'}{N}\right) e^{-u_0^2/\Delta u^2}\right\} \tag{3.61}$$

$$w_2(u_0) = e^{-u_0^2/\Delta u^2}\ \{1 - \tanh(u_0/\Delta u)\} \tag{3.62}$$

where $\Delta\mathcal{F} = -N' k_B T/2$. The negative derivative of Eq. (3.60) with respect to u_0 is nothing but the mean force f.

3.4.2 Hertzian indenter

So far, an effective potential to describe the thermal effects in terms of repulsive force has been managed in a straightforward fashion. In this section, we implement this potential into classical Hertzian contact problem to validate its applicability. Towards this end, we investigate how thermal fluctuations effect the load-displacement relation within the framework of GFMD. Additionally, the definition of a contact area with consideration of thermal fluctuations is also studied.

In order to avoid the discreteness problem, the grid distance Δa is set to sufficiently small compared to the linear dimension of the contact area a_c. This convention allows the simulation results to be consistent with the continuous Hertzian contact theory.

The default parameters to conduct the thermal Hertzian contact simulation are listed as follows: the radius of curvature $R_\mathrm{c} = 256\ \Delta a$, the normal load $L = 131\ E^* \Delta a^2$, as a result, contact area could be calculated with the area-load expression in classical Hertzian contact theory, which is $a_\mathrm{c} \approx 30\ \Delta a$. Results for the displacement and stress profile at a given temperature $k_B T = 0.2\, E^* \Delta a^3$ are presented in Fig. 3.5.

When temperature is non-zero, the boundary of contact and non-contact domain becomes indistinct. In this case, the definition of "true contact area" should be discussed explicitly. In classical hard-wall constraint, contact can be detected only when elastic solids penetrate into rigid indenter is observed. However, when thermal fluctuation is switched on, the penetration behavior turns out to be instantaneous and undetectable. As a result, the instantaneous contact area could be argued to be zero. However, during each instantaneous time, the forces between surfaces is infinitely large, consequently, the stress profile is similar to a classical Hertzian case after time averaging. If the temperature is sufficiently small, the stress profile would very close to an athermal Hertzian case.

Regarding the definition of true contact area, we follow the idea that define a contact line where the gradient of the normal stress has a maximum slope, which is proposed in a recent paper [89]. In this example, this definition leads to a reduction of contact radius of order 1%, while the normal displacement is reduced by roughly 30%.

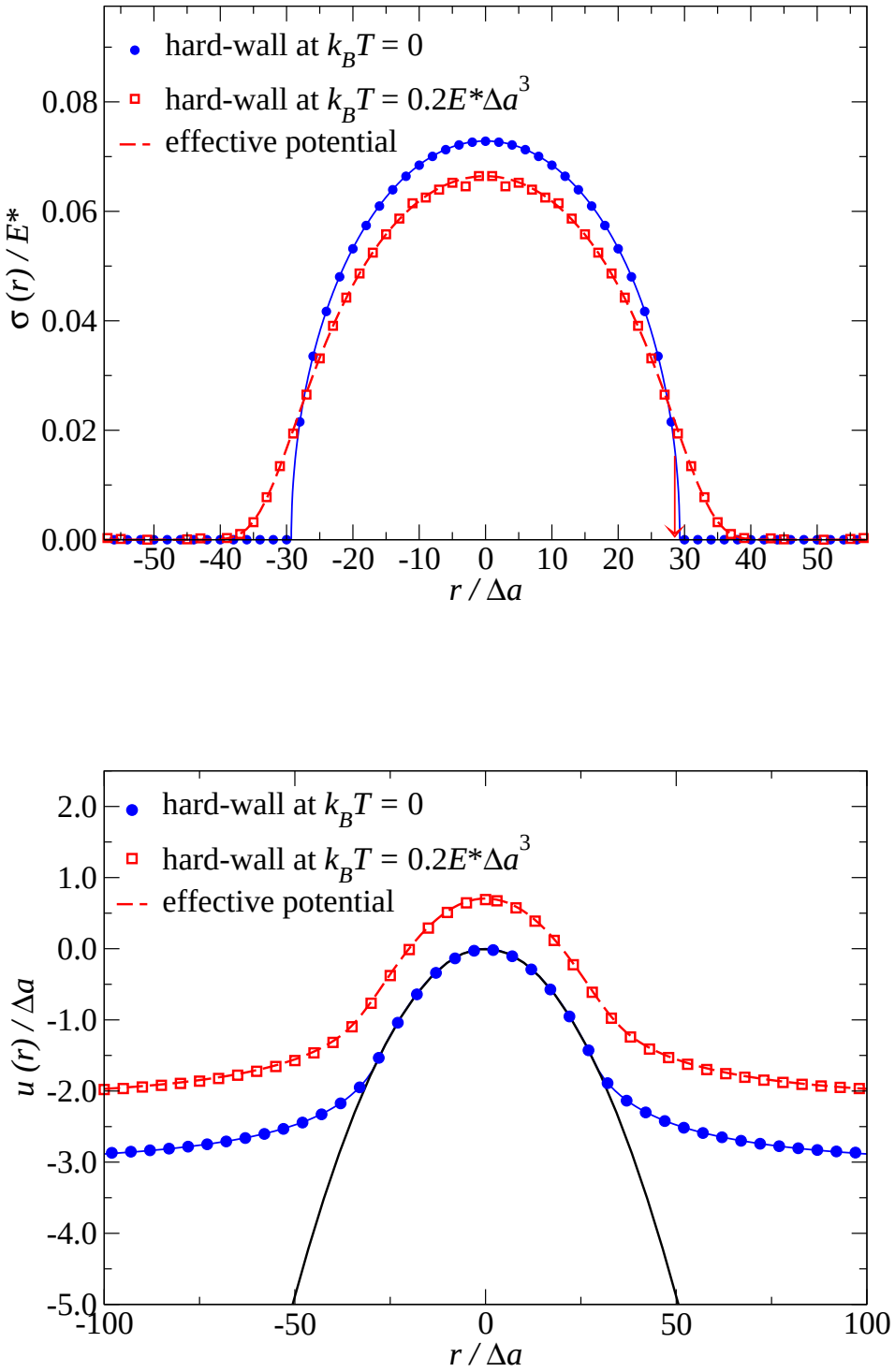

Figure 3.5: **Top:** Interfacial stress σ as a function of distance $r/\Delta a$ from the symmetry axis. The blue circles represent GFMD data at $k_BT = 0$ with hard-wall overlap potential, the blue line is the analytical solution of stress in Hertzian contact problem. The red open squares represent full simulation data at finite temperature, while the red dotted line shows GFMD data without thermal fluctuations, however, an effective potential was constructed to reflect the thermal effects at a given temperature. The arrow marks the point of largest slope for the thermal indenter. **Bottom:** Displacement field $u(r)$ as a function of distance r from the symmetry axis.

Unlike the definition of contact area, the load-displacement relation for thermal contact problem could be defined in a straightforward way. As mentioned in Sec. 3.1.2, because of the repulsive force induced by the thermal fluctuations, the displacement d will reduced by d_T. The expression of displacement d for classical Hertzian contact problem is scale free, in a similar manner, the temperature induced displacement d_T/d_0 should also hold this property when $\Delta a \ll a_\mathrm{c}$. As shown in Fig. 3.6, the thermal displacement d_T for different Hertzian realizations can be mapped exactly on a single master curve $\Xi(T/\tilde{T})$, which reads

$$d_T = \tilde{d}_0 \, \Xi(T/\tilde{T}), \tag{3.63}$$

where

$$\tilde{d}_0 = \left(\frac{R_\mathrm{c} L}{E^* \Delta a^3} \right)^{-\frac{1}{3}} d_0 \tag{3.64}$$

and

$$\tilde{T} = \left(\frac{L}{E^* R_\mathrm{c}^2} \right)^{\frac{2}{3}} \frac{E^* \Delta a^3}{k_B}. \tag{3.65}$$

The master curve describes the thermal displacement at low and high temperature limits. It shows that d_T could be approximated with power laws, however, logarithmic corrections should be made for both limits, such that the approximation could be consistent with GFMD data.

$$\Xi(t) \approx \begin{cases} t\,(1 - \ln t) & \text{for } t \ll 1 \\ 1.727\,\sqrt{t}\,\{1 + \ln(t)/6\} & \text{for } 0.1 < t < 10^4 \end{cases} . \tag{3.66}$$

Substituting the low-temperature limit to Eq. (3.63) would result in the following thermal displacement expression.

$$\frac{d_T}{d_0} \approx \frac{T}{T^*} \left(1 - \ln \frac{T}{\tilde{T}} \right) \tag{3.67}$$

for $T \ll \tilde{T}$. This expression indicates that the low-temperature approximation deduced in Sec. 3.3.3 predicted correctly the linear term, but failed to predict the logarithmic corrections, which become dominant for a small ratio $T/\tilde{T}$.

The argument that extending the integration domain in Eq. (3.51) back to radii beyond the athermal contact radius would lead better results at small $T/\tilde{T}$ is demonstrated to be inefficient. The reason is sketched as follows: the displacement

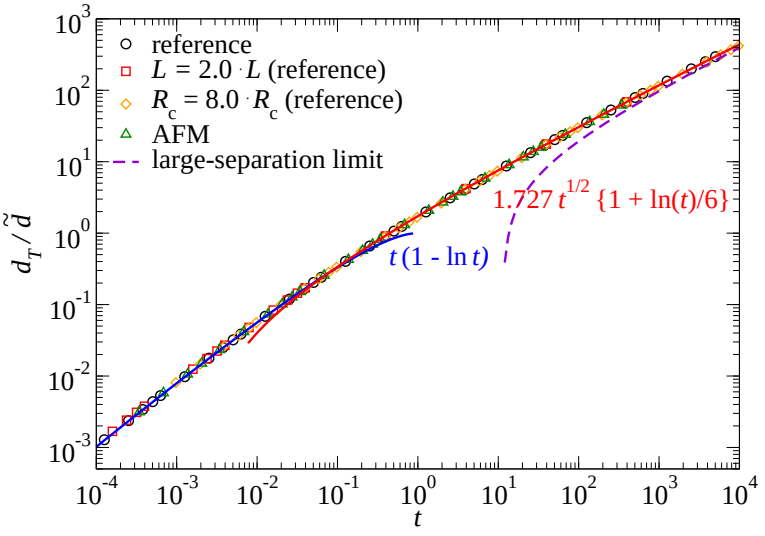

Figure 3.6: Reduced thermal displacement $d_{\mathrm{T}}/\tilde{d}_0$ as a function of reduced temperature $t = T/\tilde{T}$ for different Hertzian contact realizations. The reference model (black circles) is defined in Sec. 3.4.2. In one case, load was increased by a factor of two (red squares), and in another case, the radius of curvature was increased by a factor of eight (orange diamonds) with respect to the default values. Green triangles represent GFMD simulations with parameters in real units: $\Delta a = 2.5$ Å, $R_{\mathrm{c}} = 200$ nm, $E^* = 100$ GPa, and $L = 200$ nN, which was a typical blunt atomic-force microscope (AFM) indenter contact. Solid blue and red line show the low- and intermediate-temperature approximation from Eq. (3.66). The dash line indicates the high temperature limit of Eq. (3.59).

shift due to thermal fluctuations is assumed to be a constant, which is inconsistent with the results as shown in Fig. 3.7, this shift far away from the indenter is significantly larger than at $r = 0$ and this difference increases with decreasing temperature. Nevertheless, we still decided to keep this low-temperature discussion since it allows one to rationalize $d_T \sim T$ relation to be linear.

From a practical point of view, one may want to study the thermal displacements for real rather than for reduced units. Before investigating this issue, we should make it clear that the range of application of the master curve presented in Eq. (3.66) for $t > 0.1$ can only hold for the shown domain, and cannot extend to $t \to \infty$. Nevertheless, when $t > 10^3$, the correlated temperature is already far beyond that required for a typical real-laboratory experiment which turns out to be almost impossible to be reached. Therefore, we would like to conclude that this master curve is still applicable for practical purposes.

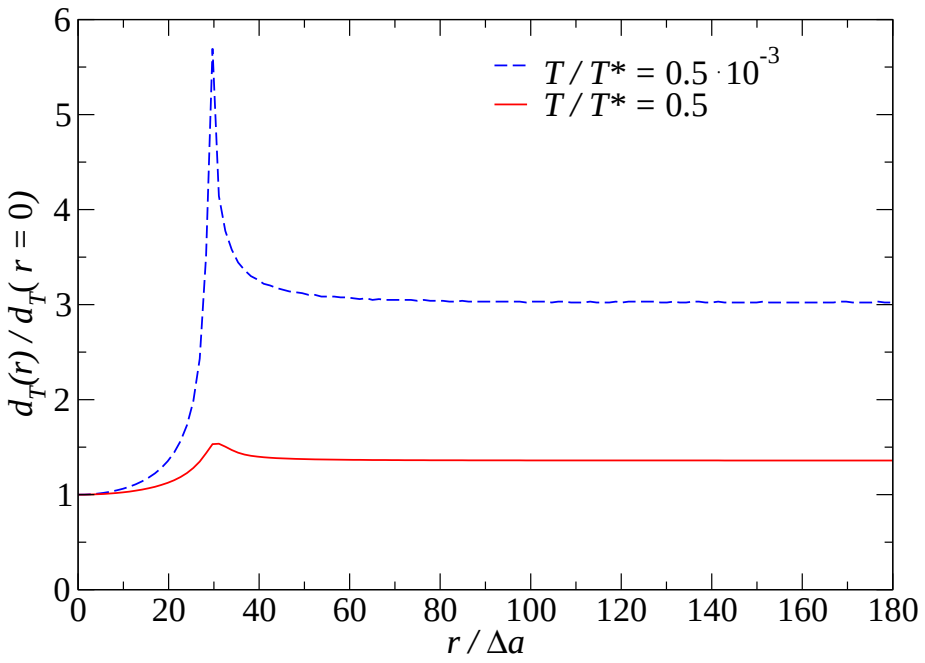

Figure 3.7: Spatially resolved thermal displacement d_T as a function of distance $r/\Delta a$ from the symmetry axis, where d_T was normalized to its value at $r = 0$. Dashed blue line represents the lower temperature case, while solid red line represents the high temperature case.

At this point, we start to explore the issue that translating $d(T)$ dependence with real units rather than reduced units. Towards this end, the expressions for both low-temperature and intermediate-temperature limits are updated for a hard-matter ($E^* = 1$ GPa) and a soft-matter ($E^* = 50$ MPa) system. The expressions are demonstrated by thermal GFMD simulations. Results are presented in Fig. 3.8. The radius of curvature was set to $R_c = 50$ nm for both cases and the external load was adjusted so that plastic deformation can be neglected.

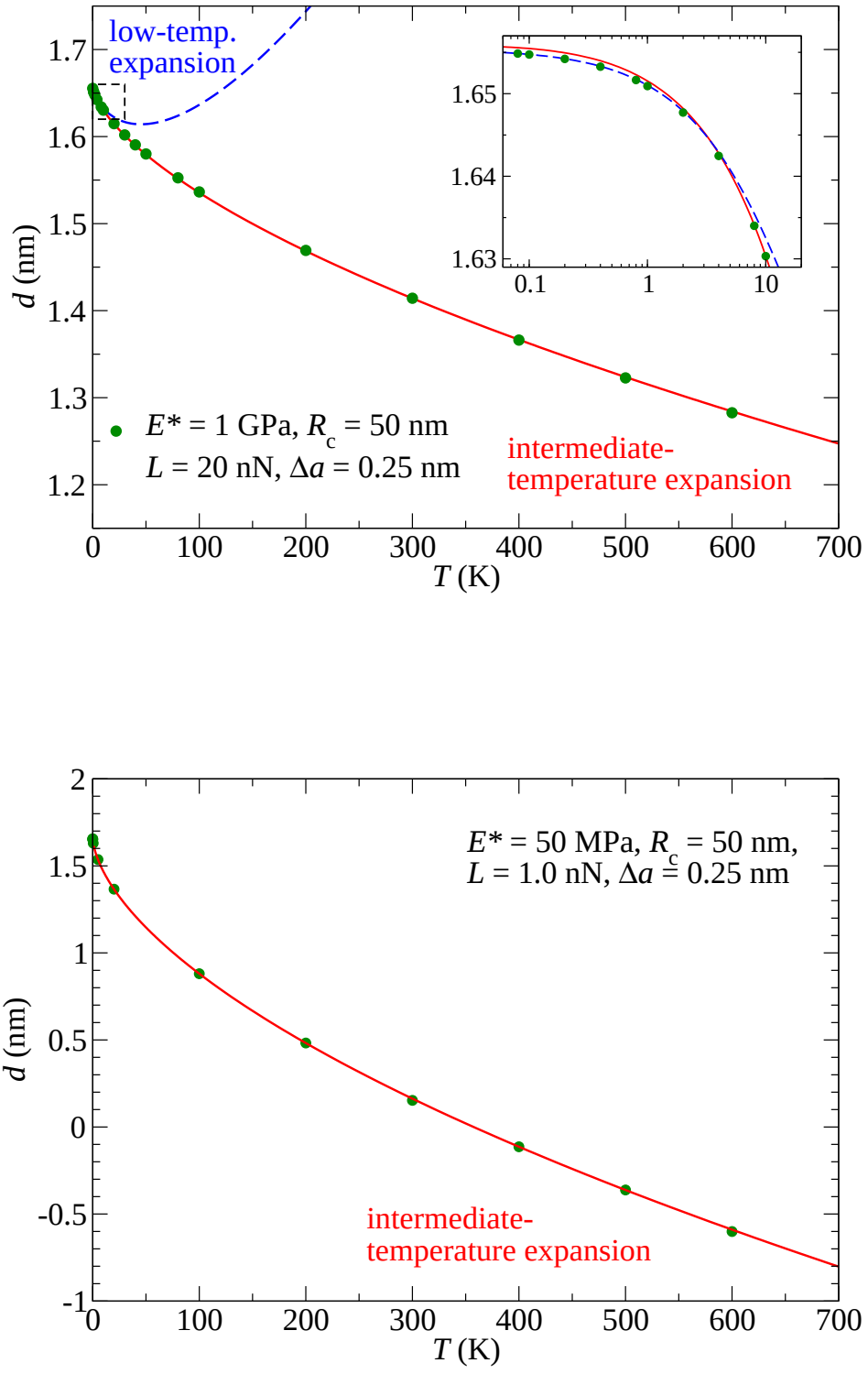

Figure 3.8: Displacement d as a function of temperature T for fixed external load. Top figure corresponds to hard-matter ($E^* = 1$ GPa), and the bottom figure corresponds to soft-matter ($E^* = 50$ MPa). Green circles indicate the GFMD data. Red lines represent the intermediate-temperature approximations, while blue dashed line represents the low-temperature approximation.

As shown in Fig. 3.8, the GFMD results of both soft- and hard-matter match the intermediate-temperature estimation at room temperature extremely well. Relative corrections are required at low-temperature limit for hard-matter and can be ignored for soft-matter. This observation motivated us to explore the question: how far do thermal fluctuations affect the load-displacement relation? This question is critical to contact mechanics experiments because most indentation experiments are conducted at constant temperature and varying load. Substituting the intermediate-temperature approximation of Eq. (3.66) into Eqs. (3.63–3.65) and considering the displacement-load relation in classical Hertzian contact theory leads to

$$d_T = d_T^{\mathrm{ref}} \left\{ 1 - \frac{1}{9} \ln\left(L/L^{\mathrm{ref}}\right) \right\} \tag{3.68}$$

with $d_{\mathrm{T}}^{\mathrm{ref}} \approx 1.426\,\Delta u$ and

$$L^{\mathrm{ref}} \;=\; \left(\frac{k_B T}{E \Delta a^3}\right)^{3/2} E^* R_{\mathrm{c}}^2. \tag{3.69}$$

This expression indicates that when thermal fluctuation is switched on, the thermal shift is only roughly 1.5 times the thermal standard deviation of its smallest-scale surface fluctuations.

As shown in Fig. 3.9, the thermal corrections leads to a constant shift for soft matter systems. When external load equals to $L \approx 16$ nN, the corresponding thermal shift is $d_T \approx 1.2$. Reducing the external load by 100 times only leads to a bare change of thermal shift, say $d_T \approx 1.7$. If twice the value of thermal displacement compared to that at 16 nN is required, a corresponding external load of 20 fN is expected, which is almost undetectable. For reasons of completeness, we state that the range of validity of the intermediate-temperature approximation of $0.1 < t < 10^4$ demonstrated in Fig. 3.6 translates to a range of loads of $0.15 < L/\mathrm{nN} < 1.5 \cdot 10^4$ for the specific examples studied here. This range is sufficient for most of indenter experiments.

3.5 Conclusion

In this chapter, the effect of thermal fluctuations on classical Hertzian contact mechanics in the case of hard-wall interactions is studied. Towards this end, we

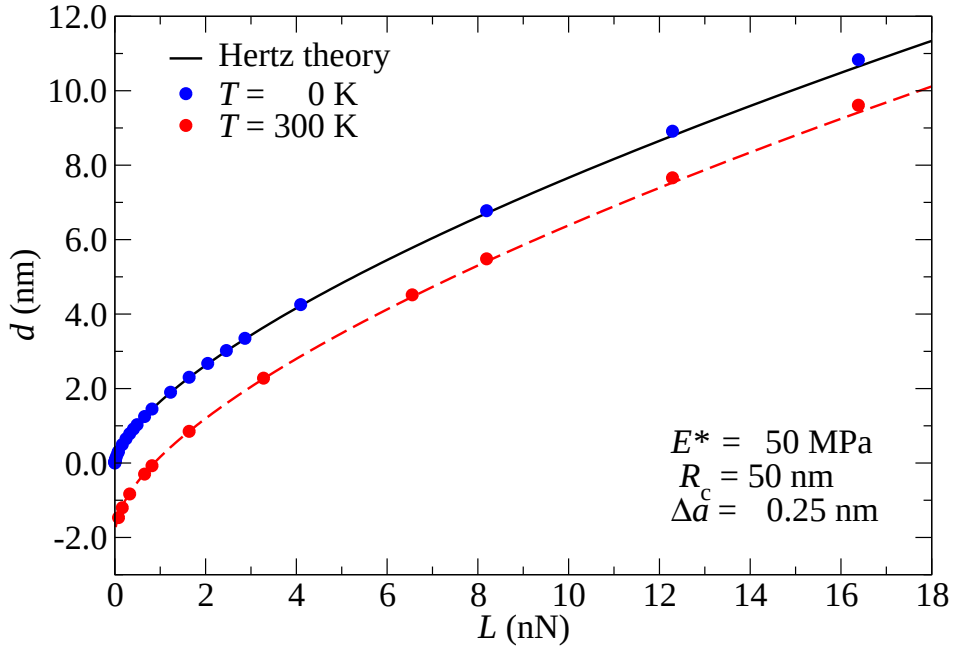

Figure 3.9: Displacement d as a function of external load L for a soft-matter ($E^* = 50$ MPa). Blue circles indicate GFMD data with zero temperature, and the red circles indicate the GFMD data with $T = 300$ K, which corresponds to room temperature. Black line is the load-displacement curve in Hertzian theory. Red dashed line represents the intermediate-temperature approximations.

first investigate an initially flat elastic surface contacts with a flat rigid indenter. The purpose is to construct effective surface interactions so that the thermal effect could be considered in the case of hard-wall interaction. The thermal fluctuations could be translated to a finite-range repulsive force. The functional form of this repulsive force was derived analytically and demonstrated to increase with decreasing the interfacial separation u_0 at small u_0 but starts to decrease quickly with increasing interfacial separation when u_0 is sufficiently large.

To validate the analytical approach, Green's function molecular dynamics (GFMD) technique was extended to include thermal fluctuations. The most critical issue that needs to be addressed here was how to deal with hard-wall interactions in the simulations. A stiff harmonic potential was introduced to replace the hard-wall constraint and it turns out to be applicable if simulations are conducted at different values for the stiffness and extrapolation is made to infinite stiffness. The GFMD

results are consistent with the different mean-field approaches to the thermal contact mechanics problem addressed above. In this way, an accurate, closed-form displacement-force relation was obtained to describe the contact behavior of an initially flat, linear elastic solids and a flat, rigid substrate.

After that, we applied this effective hard-wall interaction to the classical Hertzian contact problem and a noticeable shift in the normal displacement is obtained. The thermal shift of Hertzian indenter was demonstrated to be slightly less than 1.5 times the thermal standard deviation of surface positions of a free, initially flat surface. Logarithmic corrections which depend on external load turns out to be negligible. In this case, thermal noise leads to a shift of the load-displacement curve that is roughly equal to the root-mean-square fluctuation of surface atoms but almost independent of the load. Constant shifts usually hardly undetectable, this could potentially explain why Hertzian contact theory can be applied to nanoscale problem without trouble.

As expectation, similar results should be reached if the classical Hertzian contact replaced by randomly rough surface contact. On the other hand, if the short range adhesion is included into this study, we expect a reduction of this adhesion would be obtained due to thermal fluctuations. Future works could attempt to elucidate this issue.

Chapter 4

Effects of structural parameters on the relative contact area

This chapter attempts to understand what structural parameters characterizing the surface topography affect the area-pressure relation in nominally flat contacts. Towards this end, the friction-, and adhesionless contact problem between an initially flat, linearly elastic solid and a rigid indenter with various profiles was studied. Specifically, the indenter was designed to move from below, and the hard-wall constraint between these two bodies was imposed. Green's function molecular dynamics (GFMD) is a technique that allows us to solve this kind of contact problem in the framework of MD, which has already been widely used in contact mechanics study [7, 41, 87, 90]. As throughout this thesis, we use the FIRE-GFMD, which is demonstrated to be an efficient and reliable solver to locate the stable mechanical structure of contact simulations quickly [75].

The first counterface investigated in this chapter is an isotropic, randomly rough indenter, which is commonly used in many contact mechanics studies. The second case was also a randomly rough indenter, however, the isotropy was destroyed. The third case is an isotropic warping indenter, which is a typical randomly rough, phase correlated surface. The fourth and the last case was a generilized Hertzian indenter.

The remainder of this chapter is organized as followes: The elastic body and rigid indenter are introduced in Sec. 4.1. The theory is sketched in Sec. 4.2, which includes the construction of topographic order parameters beyond the Nayak

parameter. Results are presented in Sec. 4.3, while conclusions are shown in Sec. 4.4.

4.1 Model design

4.1.1 Elastic body

The elastic body studied in this chapter is designed as initially flat, linear elastic body. Periodic boundary conditions are assumed by default with the intention to reduce finite-size effect and simplify the numerical simulation.

An external load is applied to the elastic body so that the contact between elastic body and rigid indenter could be measured. In order to avoid one single point contact, the minimum load is adjusted to lead to at least one meso-scale asperity in contact. The interaction considered in this chapter is the hard-wall constraint, or non-overlap constraint, in which case the contact is considered only if the penetration of the elastic body is detected. In addition, the small-slope approximation is also assumed, which allows us to assume a zero shear-stress boundary conditions between the bodies.

4.1.2 Rigid indenter

Isotropic rpa indenter

The default indenter considered in this study is randomly rough, self-affine surface, which is fully defined by a height power spectral function $C(q)$. This kind of surface has a feature that the stochastic properties are dominated by the resolution of the measuring apparatus. The spectrum used in this chapter reads

$$C(q) = C(q_{\mathrm{r}}) \times \begin{cases} f_{\mathrm{roll}} & \text{if } q < q_{\mathrm{r}} \\ (q/q_{\mathrm{r}})^{-2(1+H)} & \text{if } q_{\mathrm{r}} < q < q_{\mathrm{s}} \\ 0 & \text{else,} \end{cases} \tag{4.1}$$

where f_{roll} is a Boolean variable, of which the value can only be zero or one. It is set to be zero by default in this study and only set to one when mentioned

explicitly. In this case, the roll-off wavelength $\lambda_\mathrm{r} = 2\pi/q_\mathrm{r}$ plays the role of a long wavelength cutoff. Accordingly, the properties of the isotropic rpa surface is fully defined by the Hurst exponent H, the system size $\mathcal{L}$, the roll-off wavelength λ_r and cut-off $\lambda_\mathrm{s} = 2\pi/q_\mathrm{s}$, and a prefactor $C(q_\mathrm{r})$. In practice, $\mathcal{L}$ should be chosen larger than λ_r to average implicitly over different random realizations, which can become relevant for large Hurst exponent at small relative contact area.

The surface is defined according to

$$\tilde{h}(\mathbf{q}) = \sqrt{C(q)}e^{2\pi i r(\mathbf{q})} \tag{4.2}$$

where $r(\mathbf{q})$ is a uniform random number on $(0, 1)$. $\tilde{h}(\mathbf{q})$ represents the Fourier transform of height profile. The real space representation could be obtained if the following convention is applied.

$$h(\mathbf{r}) = \sum_{\mathbf{q}} \tilde{h}(\mathbf{q})\exp[i\mathbf{q}\cdot\mathbf{r}] \tag{4.3}$$

$$\tilde{h}(\mathbf{q}) = \frac{1}{N}\sum_{\mathbf{r}} h(\mathbf{r})\exp[-i\mathbf{q}\cdot\mathbf{r}] \tag{4.4}$$

where N denotes the number of grid points, into which the surface is discretized.

Anisotropic rpa indenter

An anisotropic surface is realized by introducing a single number, known as "Peklenik" number γ_P. The number results in an effective wavenumber

$$q_\mathrm{P} = \left(\frac{\gamma_\mathrm{P}^2 q_x^2 + q_y^2/\gamma_\mathrm{P}^2}{\sqrt{\gamma_\mathrm{P}^4 + 1/\gamma_\mathrm{P}^4}}\right)^{1/2} \tag{4.5}$$

as the variable to be used in the height spectrum rather than the true wave number q. The Peklenik number satisfies $0 < \gamma_\mathrm{P} < \infty$. The isotropic rpa surface is realized when $\gamma_\mathrm{P} = 1$. The such produced height profiles reveal prefered directions or "grooves", as shown in Fig. 4.1.

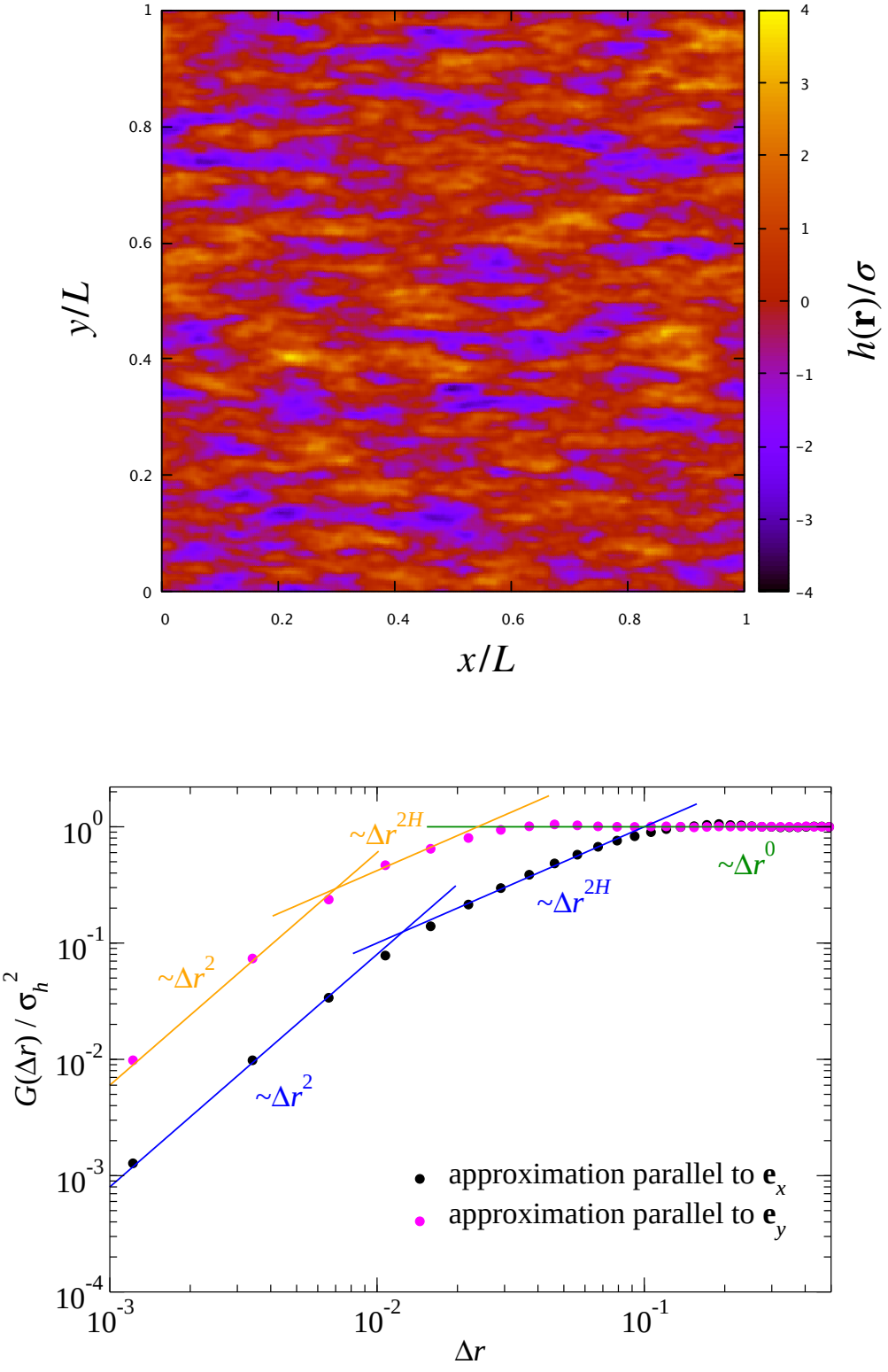

Figure 4.1: **Top**: Anisotropic rpa surface profile with a Peklenik number of $\gamma_{\mathrm{P}} = 4$. **Bottom**: Height-difference auto-correlation function $C(r)$ for shown topography and $\mathbf{r}$ parallel to $\mathbf{e}_x$ (closed black circles) and $\mathbf{e}_y$ (closed pink circles).

Isotropic height-warped indenter

An isotropic height-warped surface is defined by

$$h_w = \begin{cases} h_{\min} + (h - h_{\min}) \left(\frac{h - h_{\min}}{h_{\max} - h_{\min}} \right)^w & \text{if } w \geq 0 \\ h_{\max} - (h_{\max} - h) \left(\frac{h_{\max} - h}{h_{\max} - h_{\min}} \right)^{|w|} & \text{else,} \end{cases} \tag{4.6}$$

where $h_{\min} \leq \mathrm{Min}\{h(\mathbf{r})\}$ and $h_{\max} \geq \mathrm{Max}\{h(\mathbf{r})\}$. Here h indicates the height of an ideal randomly rough surface at a given position $\mathbf{r}$ and h_w is the height after warping transform at the same position. According to this expression, the surface remains unchanged when $w = 0$. When $w > 0$, peaks are blunted and valleys are sharpened, while the opposite is achieved with $w < 0$, as can be seen explicitly in the cross-section of the height profile shown in Fig. 4.2. In the current study, $h_{\min} = 2\mathrm{Min}\{h(\mathbf{r})\} - \mathrm{Max}\{h(\mathbf{r})\}$ and $h_{\max} = 2\mathrm{Max}\{h(\mathbf{r})\} - \mathrm{Min}\{h(\mathbf{r})\}$ were applied.

Phase correlation through the warping procedure is reflected by the observation that the height histograms are systematically skewed for $w \neq 0$. The reference histogram is produced with rpa surface, which turns out to be symmetric. Additionally, the expectation value of the rms gradient is much increased in the sharpened parts and significantly reduced in the blunted domains. In contrast, for sufficiently large rpa surfaces, $\bar{g}$ is independent of the height, except near the heighest and lowest heights in a finite sample. In practical point of view, the Peklenik parameter should be correlated with wave vector [91]. The warping surface should also include additional refinements. However, our impression is that the constant γ_{P} already includes the feature of scratched surface. $w = 2$ could also lead to a reasonable polished surface, *i.e.*, relatively deep valleys and smoothened tops.

Generalized Hertzian indenter

The last indenter is a generalized Hertzian indenter, which is defined by

$$h(r) = \frac{R}{n} \left(\frac{r}{R} \right)^n \tag{4.7}$$

where R is of unit of length, r is the in-plane distance of a point from the symmetry axis of an individual indenter, which we place into the center-of-mass of the

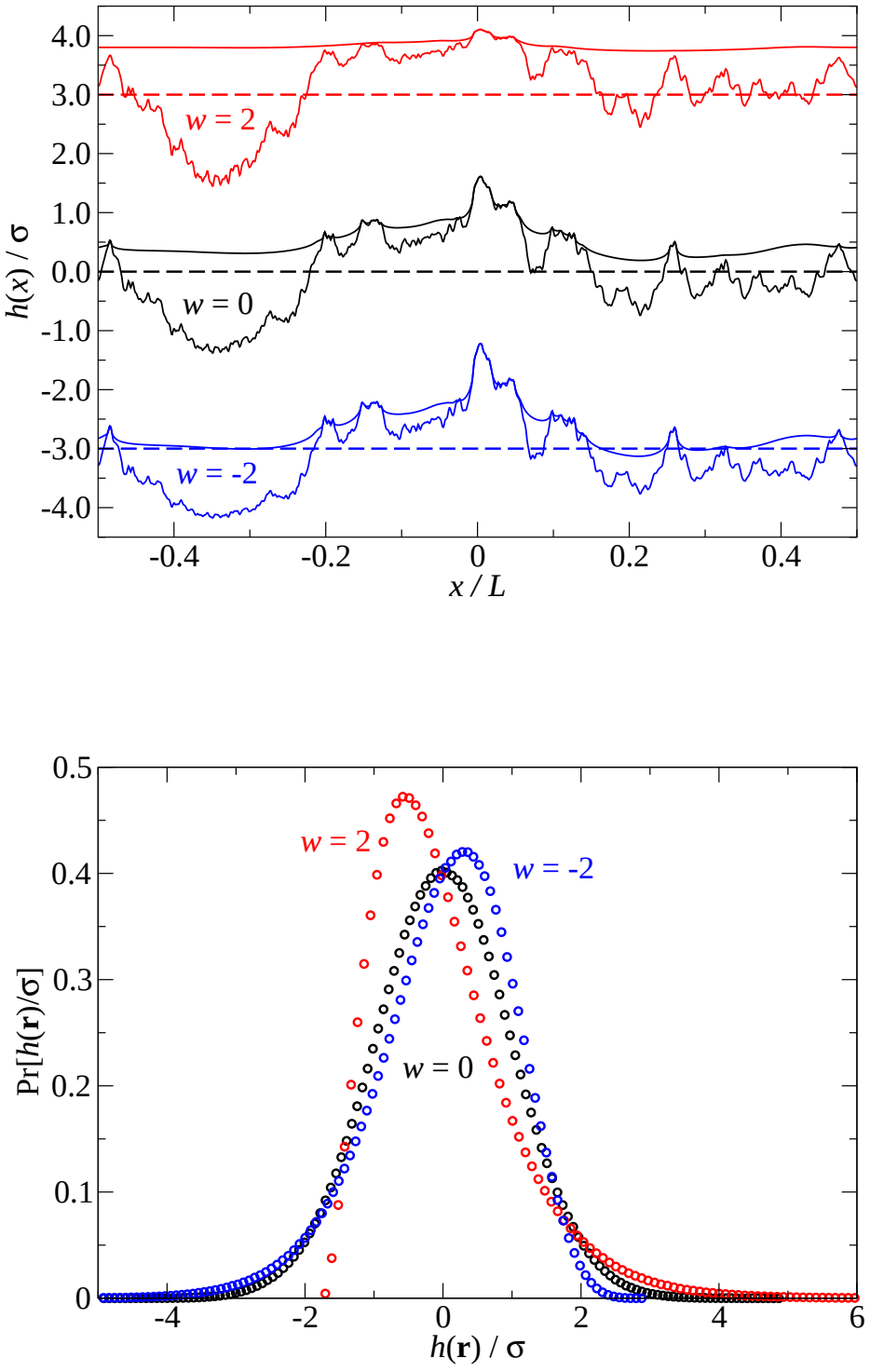

Figure 4.2: **Top:** Height profile of warped indenters along a cross-section as a function of x coordinates. Different color represents different warping w: red for $w = 2$, black for $w = 0$, and blue for $w = -2$. The dashed lines indicate the center-of-mass height for the shown cross section. The curves $w = \pm 2$ are shifted by a constant to improve their visualization. **Bottom:** Height histograms for the different surfaces.

simulation cell. Different values of n lead to different profiles. In this study, we study the surfaces generated from three different values of n, *i.e.*, $n = 1.5$ (sharp indenter), $n = 2$ (parabolic indenter), and $n = 4$ (blunt indenter).

4.2 Theory

4.2.1 Prediction of κ in Persson theory

Considering a linearly elastic solid in contact with an ideal randomly rough, self-affine fractal rigid substrate, Persson theory predicts the area-load relation as

$$a_{\mathrm{r}} = \mathrm{erf}\left\{\sqrt{2}\, p_0 / E^* \bar{g}\right\}, \tag{4.8}$$

where $\bar{g}$ is the rms height gradient averaged over the entire surface, *i.e.*,

$$\bar{g}^2 = \int d^2q\, C(q)\, q^2. \tag{4.9}$$

Eq. (4.8) not only works for randomly rough indenter, but also holds for smooth indenters with harmonic height profiles defined in Eq. (4.7) if $\bar{g}$ is evaluated over the true contact domains [92], in which case the $\bar{g}$ is replaced by $\bar{g}_{\mathrm{c}}$. Therefore, the range of applicability of Eq. (4.8) appears to extend when re-expressing it through

$$a_{\mathrm{r}} = \mathrm{erf}\left(\sqrt{\pi}\kappa_{\mathrm{c}} p^*_{\mathrm{c}}/2\right), \tag{4.10}$$

where κ_c is the proportionality coefficient of area-load relation, $p^*_{\mathrm{c}} = p_0/(E^*\bar{g}_{\mathrm{c}})$ represents the reduced pressure, the index "c" indicates that the quantity is evaluated over the true contact zones rather than the entire surface.

In fact, when taking Persson theory literally, it does ask the question how the rms-height changes in a given point of contact (described using a small resolution of the surface topography) when short-wavelength roughness is added to the description of the contact problem. Using the full spectrum to estimate this increase in the rms-roughness can be seen as an approximation, which might be possible to correct in future work.

Persson theory predicts a value of $\kappa = \sqrt{8/\pi} \approx 1.596$. In the formulation of the theory, it appears to us as if no distinction is made – or must be made – between κ and κ_c, at least as long as pressures lie in a range in which $a_r \propto p$, that is, if p is sufficiently large for contact to spread out over clearly disconnected contact patches but still small enough so that a_r is less than, say, 0.05. Careful simulations of sufficiently large systems find a relatively weak dependence of κ on the Hurst roughness exponent, e.g., $\kappa(H \approx 0.8) \lesssim 2$ and $\kappa(H \approx 0.3) \gtrsim 2$. [35, 52–54, 57, 93]. Analytical results for the Hertz contact result in $\kappa_c \approx 1.666$, see also Eq. (4.29) and the more detailed discussion of periodically repeated, smooth indenters in Sec. 4.3.5.

4.2.2 Definitions of scalar parameters

Relative contact area is determined by the ratio of the true contact area and the nominal contact area. Therefore, it is a scalar, and it can only be a function of other scalars, such as reduced pressure p^*, Nayak parameter Φ_N and other scalar structural parameters. In principle, structural parameters, including Nayak parameter, must follow the law of dimensional analysis, some details about such dimensional analysis could be found in Ref.[40]. Additionally, real contact is destroyed predominantly due to roughness at small wavelengths. Therefore, those structural parameters Φ_i, where i indicates an integer, should not depend on parameters that are defined exclusively by parameters from the height-distribution.

Because the structural parameters are closely correlated with square-gradient height, we could discuss the square-gradient term firstly. When determining $\bar{g}$ over a periodically repeated surface, $\bar{g}^2 \equiv \langle (\nabla h)^2 \rangle$ is identical to $-\langle \delta h \Delta h \rangle$, where $\delta h = h - \langle h \rangle$, and $\langle \bullet \rangle$ represents ensemble average. However, this equality only holds for full contact. If the situation from full contact turns to partial contact, we define

$$\left(\bar{g}_c'\right)^2 = -\langle \delta h \Delta h \rangle_c \tag{4.11}$$

the dependence of a_{rel} on parameters depending on height profiles in the contact then becomes

$$a_{rel} = a_{rel}[p/(E^* \bar{g}_c), \bar{g}_c/\bar{g}_c', \{\Phi_c\}]. \tag{4.12}$$

Ultimately, a_{rel} is a functional of the height topography. As such, there should exist a dependence of a_{rel} that does not necessitate parameters averaged over the real

contact. However, those might necessitate very non-local terms, or, alternatively, high-order derivatives of $h(\mathbf{r})$. The latter may not be well defined when the surface profile or its (higher-order) derivatives are not well defined, as is the case, for example, for a conical indenter. Thus, the following discussion assumes surface height profiles to be sufficiently smooth.

Regarding the construction of relevant parameters used to determine the contact area, it is useful to keep in mind three symmetry relations. First, inversion ($\mathbf{r} \to -\mathbf{r}$) leaves the contact area unchanged. This is why each derivative with respect to a spatial coordinate must appear an even number of times in the construction of an invariant. Second, each measure should be rotationally invariant and reduce to a scalar. This is automatically achieved when representing derivatives with the Einstein summation convention, which requires every index (enumerating an in-plane coordinate) occurring twice in a product to be summed over. To use it effectively, we use it jointly with the index notation, in which case h_α^2 indicates the square-height gradient $(\nabla h) \cdot (\nabla h)$ and $h_{\alpha\alpha}$ the Laplacian Δh. However, $\bar{g}$ will keep indicating the rms height gradient $\sqrt{\langle h_\alpha^2 \rangle}$. Third, the invariants may not change on a rigid, vertical translation of the surface $h(\mathbf{r}) \to h(\mathbf{r}) + h_0$. This is why only $\delta h = h - \langle h \rangle$ can appear in the invariants. The lowest-order invariant obeying these rules that we could identify are given by

$$\Phi_1 = \frac{\langle \delta h \, h_\alpha^2 \rangle}{\sqrt{\langle h_\alpha^2 \rangle} \, \bar{g}^2} \tag{4.13}$$

$$\Phi_2 = \frac{-\langle \delta h^2 \, h_{\alpha\alpha} \rangle}{2\sqrt{\langle \delta h^2 \rangle} \, \bar{g}^2} \tag{4.14}$$

$$\Phi_3 = \frac{-\langle \delta h^2 \rangle \, \langle h_{\alpha\alpha} \rangle}{2\sqrt{\langle \delta h^2 \rangle} \, \bar{g}^2}. \tag{4.15}$$

Before constructing the next parameters, the allowed values for the parameter Φ_1 to Φ_3 will be discussed. Φ_1 and Φ_2 are identical when averaged over a periodically repeated surfaces (as can be seen again by integration in parts) but not when they are determined over partial contact, in which case the index "c" would be added. The parameter Φ_3 is identical zero for periodically repeated surfaces but not for finite contacts, since the mean curvature disappears for a periodically repeated surface, while the curvature must average to a positive number for partial contact (assuming the elastic body indents the profile from below).

The values of Φ_1 and Φ_2 averaged over a single rpa surface may be finite. However, averaging these means over various disorder realization will make them disappear, as any surface realization $h(\mathbf{r})$ has the same probability (density) to occur $-h(\mathbf{r})$. Thus, Φ_1 and Φ_2—as well as any other parameter, in which the symbol h appears an odd number of times as a factor—should be small when determined over a single rpa surface realization, in particular when the roll-off domain is sufficiently large.

When averaged over partial contact and/or over surfaces violating the rpa, Φ_1 and Φ_2 may and usually do take finite values. This is why we call them symmetry allowed in Table 4.1. For the remaining parameters, we will no longer state the rationale for why terms are symmetry allowed or forbidden, as all relevant arguments have been mentioned or are contained in Sec. 4.2.3. Table 4.1 summarizes our conclusions on each parameter constructed in this work.

Additional parameters in which numerator and denominator are second order in the derivative but higher order in h can be constructed. They will be considered up to the lowest order needed beyond the rms-height gradient, in which the parameters do not disappear in case of the random-phase approximation. This includes the parameters

$$\Phi_4 = \frac{\langle \delta h^2 \, h_\alpha^2 \rangle}{\langle \delta h^2 \rangle \, \bar{g}^2} \tag{4.16}$$

$$\Phi_5 = \frac{-\langle \delta h^3 \, h_{\alpha\alpha} \rangle}{3 \langle \delta h^2 \rangle \, \bar{g}^2} \tag{4.17}$$

For rpa-surfaces, Φ_4 is automatically equal to unity and for all periodically repeated surfaces, $\Phi_4 = \Phi_5$.

Finally, we consider parameters in which the order of the derivatives is increased from two to four while the order in the height is kept as small as possible. Three of quite a few resulting (irreducible) possibilities are

$$\Phi_6 = \frac{1}{\bar{g}^4} \left\langle \delta h^2 \right\rangle \left\langle h_{\alpha\alpha} h_{\beta\beta} \right\rangle \tag{4.18}$$

$$\Phi_7 = \frac{2}{3\,\bar{g}^4} \left\langle \delta h^2 \, h_{\alpha\alpha} h_{\beta\beta} \right\rangle \tag{4.19}$$

$$\Phi_8 = \frac{1}{\bar{g}^4} \left\{ \left\langle h_\alpha^2 h_\beta^2 \right\rangle - 3 \left\langle h_\alpha^2 \right\rangle \left\langle h_\beta^2 \right\rangle + \langle h_\alpha h_\beta \rangle^2 \right\} \tag{4.20}$$

$$\Phi_9 = \frac{2}{\bar{g}^4} \left\langle h_\alpha h_\beta - h_\gamma^2 \, \delta_{\alpha\beta}/2 \right\rangle^2, \tag{4.21}$$

where $\delta_{\alpha\beta}$ is the Kronecker-delta symbol.

The parameter Φ_6 is nothing but the Nayak parameter Φ_N, up to a multiplicative constant of 2/3. It is frequently interpreted as a measure for the spectral width. We chose the prefactor such that Φ_6 and Φ_7 are equal to unity for single-wavevector roughness. The parameter Φ_7 is a generalization of the Nayak parameter. For randomly rough, rpa surface, its expectation value is close to but less than Φ_6. Thus, both parameters tend to infinity as the ratio $\varepsilon_\mathrm{f} = \lambda_\mathrm{s}/\lambda_\mathrm{r}$ becomes large, that is, with $\varepsilon_\mathrm{f}^{-2H}$. However, for (strongly) correlated random roughness Φ_7 takes much greater values than Φ_6, just as Φ_4 starts to substantially exceed unity, because the factorization of the various terms (see also Sec. 4.2.3) no longer holds once the rpa is no longer satisfied.

The parameter Φ_8 plays the role of a generalized height gradient cumulant. It is constructed such that it takes the value of zero when the fourth-order cumulant of the surface slope s parallel to any in-plane unit vector $\mathbf{n}$ takes the value of zero if it is distributed normally, i.e., when $c_{4,\mathbf{n}} = \langle s^4 \rangle - 3\langle s^2 \rangle^2$ disappears for every $\mathbf{n}$. This parameter is implicitly symmetrized with respect to its mirror images in the xz and yz planes so that $\langle s \rangle = 0$ follows. Note that Φ_8 being small is a necessary but not a sufficient criterion for every $c_{4,\mathbf{n}}$ to disappear. It is only sufficient if the surfaces are stochastically isotropic.

Finally, Φ_9 is a measure for anisotropy. It takes the values of zero and one in the limits of ideal isotropic and ideal anisotropy, respectively, where, for the latter, surfaces are perfectly smooth along one spatial direction. Assuming the Peklenik number to be independent of the wavevector, Φ_9 can be easily shown to be identical to $(\gamma_\mathrm{P}^2 - 1/\gamma_\mathrm{P}^2)^2/(\gamma_\mathrm{P}^4 + 1/\gamma_\mathrm{P}^4)$. As is the case for some other parameters too, Φ_9 is not identical to zero for an individual surface realization, but only averages to zero after taking sufficiently many surface realizations.

We conclude this section by stating that the Nayak parameter is the lowest-order scalar structural parameter that the proportionality coefficient κ can depend on if the surface is isotropic and satisfies the random-phase approximation. All other parameters of similar or smaller order in height are either identical to zero, or their expectation value is zero, or they strongly correlate with the Nayak parameter.

full prs	rpa	n-rpa
Φ_1	ϵ	allowed
Φ_2	Φ_1	Φ_1
Φ_3	0	0
Φ_4	$1-\epsilon$	allowed
Φ_5	Φ_4	Φ_4
Φ_6	allowed	allowed
Φ_7	$\approx \Phi_6$	allowed
Φ_8	ϵ	allowed
Φ_9	ϵ	ϵ
	if isotropic	if isotropic

Table 4.1: Values of parameters averaged over a full, periodically repeated surface (prs) if the random-phase approximation (rpa) is valid and when it is not valid (n-rpa). The word "allowed" indicates that a finite value is symmetry allowed. The number ϵ implies that the result averages to zero after an ensemble average over many surface realizations and that it should be small for an individual instantiation.

4.2.3 Evaluation of fourth-order invariants

For (isotropic) randomly rough surfaces, invariants being fourth order in height and fourth order in derivatives are the leading-order, scalar structural parameters that can affect the proportionality coefficient κ. Of particular interest should be those that—unlike the Nayak parameter—cannot be reduced to products of invariants being second order in height. Yet, the evaluation of fourth-order expressions is commonly done using Wick's theorem [94], which, applied to the current problem, translates to

$$\begin{aligned} C_4(\mathbf{q}_1,\ldots,\mathbf{q}_4) &\equiv \left\langle \tilde{h}(\mathbf{q}_1)\tilde{h}(\mathbf{q}_2)\tilde{h}(\mathbf{q}_3)\tilde{h}(\mathbf{q}_4)\right\rangle \\ &\approx \quad \left\langle \tilde{h}(\mathbf{q}_1)\tilde{h}(\mathbf{q}_2)\right\rangle \left\langle \tilde{h}(\mathbf{q}_3)\tilde{h}(\mathbf{q}_4)\right\rangle \\ &\quad + \left\langle \tilde{h}(\mathbf{q}_1)\tilde{h}(\mathbf{q}_3)\right\rangle \left\langle \tilde{h}(\mathbf{q}_2)\tilde{h}(\mathbf{q}_4)\right\rangle \\ &\quad + \left\langle \tilde{h}(\mathbf{q}_1)\tilde{h}(\mathbf{q}_4)\right\rangle \left\langle \tilde{h}(\mathbf{q}_2)\tilde{h}(\mathbf{q}_3)\right\rangle, \end{aligned} \tag{4.22}$$

whereby expectation values of fourth-order expressions are reduced to products of height spectra, since

$$\left\langle \tilde{h}(\mathbf{q}_m)\tilde{h}(\mathbf{q}_n)\right\rangle \propto C(|\mathbf{q}_m|)\,\delta(\mathbf{q}_m+\mathbf{q}_n), \tag{4.23}$$

where $C(q)$ is the height spectrum. Eq. (4.22) is exact for Gaussian random variables of mean zero.

4.3 Results

4.3.1 On the accurate calculation of a_r and κ

In a recent study proposed by Yastrebov and coworkers [61], a new expression to estimate the relative contact area in purpose of ensuring an unprecedented accuracy is given,

$$a_\mathrm{r} = \frac{n_\mathrm{c} - \alpha\, n_\mathrm{cl}}{n_\mathrm{tot}}, \tag{4.24}$$

where n_tot is the total number of points into which the surface is discretized and $\alpha = (\pi - 1 + \ln 2)/24$. n_c is the number of contact points, n_cl the number of contact line points, which are in contact but have at least one non-contact point as nearest neighbor.

For an isotropic rpa surface, this expression turns out to be quite efficient to get an applicable accurate relative contact area. Nevertheless, we believe that the performance can at best be comparable with a properly executed Richardson extrapolation. The reason is that the numerical coefficient $\alpha \approx 0.11811$ can hardly be universal even if the special form of writing it as $(\pi - 1 + \ln 2)/24$ might convey an intelligent mathematical reason for its specific value. To make it clear, let us assume that the leading order correction were truly follow the idea of Eq.(4.24), in which a_r is proportional to the number of contact line points within the contact domains. This number would ultimately scale with a/λ_s, because the fractal nature of the contact seizes exist in this limit, so that the contact line acquires the (fractal) dimension of unity. This linear scaling of the leading order corrections to the contact area would be picked up by Richardson extrapolation and the proportionality coefficient would automatically adjust to the exact value and not to a value, which is very good but not exact.

The proposed correction scheme can only outperform a Richardson extrapolation if higher order corrections happened to be incorporated into it, as is shown in Fig. 4.3 by the accurate values from the Yastrebov extrapolation at large ε_c. However, since the exact value α must depend on the specifics of a simulation, it

can only be exact in isolated cases of measure zero so that it is generally asymptotically inferior to Richardson. As such, a claim of having provided data with unprecedented accuracy with this method is not justified given that previous works used a Richardson extrapolation while employing ratios of $\varepsilon_c = a/\lambda_s$, $\varepsilon_f = \lambda_s/\lambda_r$, and $\varepsilon_t = \lambda_r/\mathcal{L}$, which were simultaneously all greater than the data having the purportedly unprecedented accuracy.

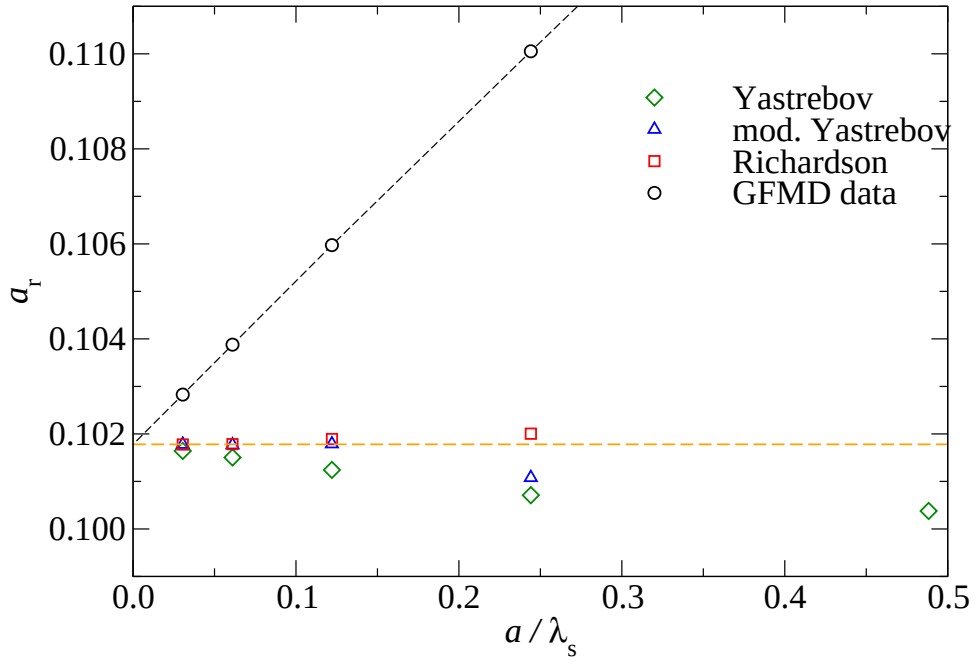

Figure 4.3: Relative contact area a_r as a function of a/λ_s for an isotropic rpa surface with different extrapolation schemes. The parameters to define the system are specified by: $H = 0.8$, $p^* = 0.05$, $\lambda_r/\mathcal{L} = 0.5$, and $\lambda_s/\mathcal{L} = 0.008$. In the modified Yastrevob extrapolation, the prefactor α in Eq. (4.24) was chosen such that the extrapolated contact area remain unchanged if discretization $a\lambda_s$ increased by a factor of 2.

To improve the performance of Yastrebov's scheme, an incorporation of Richardson extrapolation could be applied. Consider two independent contact simulations with different values of a/λ_s while leave other parameters identical. For the two simulations, the Yastrebov's extrapolation should lead to identical relative contact area. Therefore, the resulting α should also be adjusted such that the extrapolation could give the same estimation. This modification leads to an improvement, as can be seen in Fig. 4.3. However, the performance turns out to be imprecise when

$a/\lambda_s \geq 1/4$. In our contact simulations, including rpa surface and warped surface, we noted that the result produced from Yastrebov's extrapolation with the choice of $\alpha = 0.11$ appears to be very close to that of Richardson extrapolation, say, within 0.1%. In order to apply Yastrebov's extrapolation scheme in our study without loss of precision, we choose $\alpha = 0.11$ and the discretization of $a/\lambda_s \lesssim 1/4$. This value of α typically deteriorates the quality of the contact area estimation for $a = \lambda_s/2$ but improves it overall otherwise.

Lastly, different pressures may lead to different errors in Yastrebov's extrapolation scheme. In this case, the following questions remain: What is the origin of their observed logarithmic correction of κ on pressure? Is it the lack of a rigorous extrapolation to the continuum ($\varepsilon_c = a/\lambda_s \to 0$), the fractal ($\varepsilon_f = \lambda_s/\lambda_r \to 0$), the thermodynamic ($\varepsilon_t = \lambda_r/\mathcal{L} \to 0$) limit? Or is it actually true? Even though our comments of their self assessment are critical, their data appears to be of similar quality as that most other leading works, which had all together come to the conclusion that κ would remain unchanged at small p [42], but which either simply took the values at the smallest value of ε_c without further extrapolation or that made Richardson extrapolations, which we can no longer reconstruct [54]. In a recent study managed by Nicola and coworkers [42], they show logarithmic corrections in κ at small p for (1+1) dimensional contact simulations even for very large sizes when many different meso-scale patches exist.

To investigate if κ is constant or not at small pressure, the trends of κ at limit $p \to 0$ is studied. Towards this end, we compute κ as a pressure-dependent function through the equation

$$a_r = \operatorname{erf}\left(\sqrt{\pi}\kappa p^*/2\right), \tag{4.25}$$

rather than through a_r/p^*, because Eq. (4.25) accounts for some of the low-pressure non linearities, as can be appreciated in Fig. 1 of Ref. ([95]).

4.3.2 Isotropic rpa surfaces

Does κ have a low-pressure limit?

κ cannot have a finite low-pressure limit, if it is defined or computed according to

$$\kappa = \left(\prod_x \lim_{\varepsilon_x \to 0}\right) \lim_{p \to 0} \kappa(p) \tag{4.26}$$

where the various limits (defined in the previous section with x taking the "values" c for continuum, f for fractal, and t for thermodynamic) are taken in arbitrary order. The reason is that for any finite system, if pressure is extremely small, only the highest asperity could be in contact, which is similar to Hertzian contact, in which case κ results in infinity.

Because it is not possible to get a finite limit with the definition of κ presented above, we turn to another approach to obtain the low-pressure limit, which reads

$$\kappa = \lim_{p\to 0} \lim_{\varepsilon_{\mathrm{t,f}}\to 0} \frac{a_{\mathrm{r}}}{p^*}, \tag{4.27}$$

With this definition, we attempt to study whether a_{r} can be proportional to p over an extended range in pressure with no or negligible logarithmic corrections to the proportionality coefficient κ if both $\varepsilon_{\mathrm{t,f}}$ are sufficiently small while ε_{c} is properly taken to zero at each pressure. This limit is certainly not approached if the product $\varepsilon_{\mathrm{t}}\varepsilon_{\mathrm{f}}$ is not taken to infinite similarly small while having a varying discretization errors, as in Ref. [61]. Another approach proposed by Prodanov *et al.* [54], they managed to keep all but one $\varepsilon_{\mathrm{t,f,c}}$ constant. However, this idea is not good enough, because the discretization corrections probably decrease as ε_{f} decreases due to the increase of the characteristic patch size. Additionally, they assumed that the leading errors to κ follow the sum of the power law in terms of ε_x, while they could also be of a more general form.

Alternatively, to study the trend of κ at small pressure limit, we ran simulations in which ε_{t} and/or ε_{f} were decreased simultaneously with decreasing pressure according to

$$\varepsilon = \varepsilon_{\mathrm{ref}} \left(p/p_{\mathrm{ref}}\right)^{\frac{1}{4}}. \tag{4.28}$$

Results are shown in Fig. 4.4. It reveals that κ increases apparently with decreasing p for all three $H = 0.3$ cases, while it essentially plateaus for the two $H = 0.8$ cases in which ε_{f} is decreased as p decreases. If the pressure is further decreased, the $H = 0.3$ cases could eventually reach plateaus. In this case, a qualitative difference between $H = 0.3$ and $H = 0.8$ would remain: The curves for which ε_{t} and ε_{f} are decreased with decreasing pressure lead to small values of κ for $H = 0.8$ but to large values for $H = 0.3$.

The reason for this phenomenon could be potentially linked to the distribution of contact patch areas and the characteristic contact patch size A_{c}, which we define to be the expected patch size that a randomly picked contact point belongs

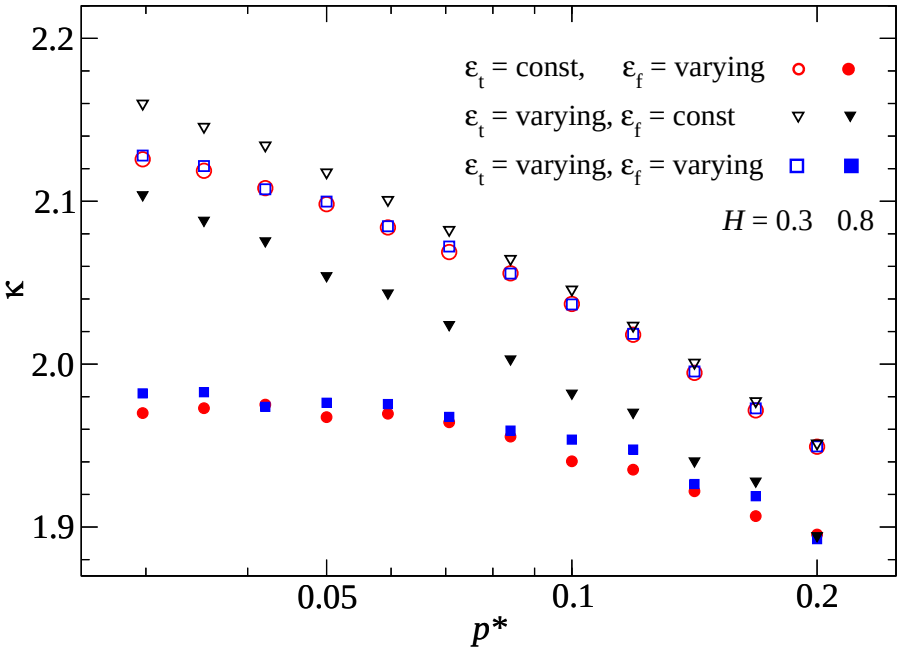

Figure 4.4: κ as defined in Eq. (4.27) as a function of reduced pressure p^*. Different color represent different choice of how $\varepsilon_{\mathrm{f,t}}$ change with pressure p. Open and closed symbols represent $H = 0.3$ and $H = 0.8$ respectively. The term "const" relates to $\varepsilon_{\mathrm{t}} = 1/2$ and $\varepsilon_{\mathrm{f}} = 1/32$. The reference value of pressure is $p^* = 0.2$. The term "varying" indicates that the respective ε is scaled according to Eq. (4.28).

to. The three $H = 0.3$ curves and the $H = 0.8$ case with fixed ε_{f}, all of which belong to those simulations in which the characteristic contact areas are rather small. According to a recent study on contact patches [96], A_{c} increases only logarithmically with ε_{f} for $H < 0.5$. In this case, large patches are not possible to occur for $H = 0.3$ cases even when ε_{f} is small. Additionally, even for $H = 0.8$ case, only small contact patches are allowed to arise at pressures well below the percolation threshold if ε_{f} is fixed to a constant value as large as $\varepsilon_{\mathrm{f}} = 1/32$. Conversely, large contact patches can arise even at small pressures if ε_{f} is small and $H > 0.5$. The large patches play a significant role in the linear area-load relation at small pressure, as can be rationalized qualitatively from bearing-area models.

To investigate whether κ has a well-defined limit when being deduced with the meaningful limit defined in Eq.(4.27), we ran simulations with two sets of $\varepsilon_{\mathrm{t,f}}$ to

comprare the resulting $\kappa(p)$ relation, the first case is a small system with $\varepsilon_\mathrm{t} = 1$ and $\varepsilon_\mathrm{f} = 1/32$, another case is a larger system with $\varepsilon_\mathrm{t} = 1/4$ and $\varepsilon_\mathrm{f} = 1/128$. The results are depicted in Fig. 4.5. This figure demonstrates that with increasing system size, *i.e.*, decreasing ε_t and ε_f, the pressure sensitivity of κ turns out to be remarkable for $H = 0.8$ case but not for $H = 0.3$ case.

The tendancies revealed in Fig. 4.5 are consistent with those of Fig. 4.4, *i.e.*, increasing system size leads to a reduction of κ and its pressure sensitivity for $H = 0.8$ but not for $H = 0.3$. The trends also roughly match the observations by Prodanov *et al.* [54], who proposed the existence of a well-defined value of κ for $H = 0.8$ but not for $H = 0.3$.

So far, we have already speculatively linked the different trends for $H = 0.3$ and $H = 0.8$ to the way how a characteristic contact patch size changes with decreasing ε_f. It motivated us to explore the explanation why A_c increases only logarithmically with ε_f for $H < 0.5$ but algebraically for $H > 0.5$. One potential reason could be that most of the elastic energy (in full contact) is stored in long-wavelength modes for $H > 0.5$ but in short-wavelength modes for $H < 0.5$. If this consideration were tenable, $H = 0.5$ could be the dividing line for the divergence. We therefore repeated simulations for $H = 0.5$ case, as shown in Fig. 4.5. However, the results leave us uncertain. More rigorous works should be conducted to characterize the transition between the different scaling behaviors in future.

In this section, we studied the trend of κ at zero pressure limit for an isotropic, rpa surface, in a manner of Eq. (4.27). For small Hurst exponent, *i.e.*, $H < 0.5$, it might not exist and/or it might depend on how $\varepsilon_\mathrm{f} \to 0$ is approached, *e.g.*, it could take different valus when reaching it with constant $\varepsilon_\mathrm{f}/\varepsilon_\mathrm{t}$ and with constant $\varepsilon_\mathrm{f}/\sqrt{\varepsilon_\mathrm{t}}$. Meanwhile, we expect that the value of $\kappa = \sqrt{2\pi} \approx 2.5$ predicted by the BGT model [97], might provide a (potentially rigorous) upper bound for κ when the limit $\varepsilon_\mathrm{t} \to 0$ is taken before $\varepsilon_\mathrm{f} \to 0$.

Effect of Nayak and related parameters on κ

Yastrebov *et al.* [61] came up with a decreased logarithmic dependence of κ on the Nayak parameter for isotropic, randomly rough, self-affine surfaces. However, this dependence appears to be problematic with respect to two aspects of their claim and their data. First, κ is implicitly predicted to become negative for very large

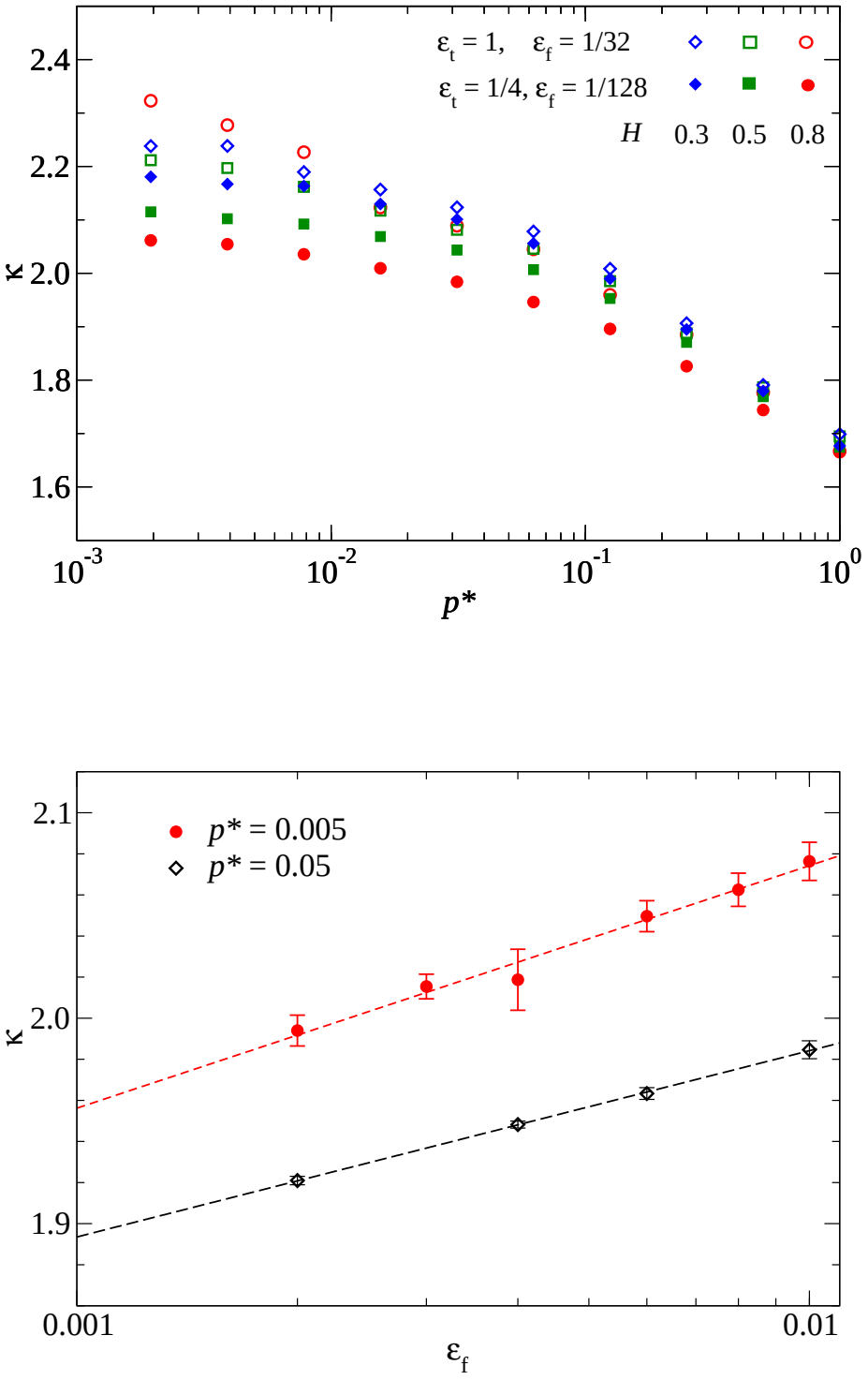

Figure 4.5: **Top:** κ as a function of reduced pressure p^*. Different color indicates different Hurst exponent. Open symbols represent GFMD data with the choice of $\varepsilon_t = 1$ and $\varepsilon_f = 1/32$, while closed symbols $\varepsilon_t = 1/4$ and $\varepsilon_f = 1/128$. **Bottom:** Scaling with ε_f for $H = 0.8$ and $\varepsilon_t = 0.5$. Dashed lines are linear fits to the three lowest values in ε_f. Results were averaged over up to 100 random realizations per data point.

Nayak parameters, which is physically meaningless. Second, their data points seem to be partially inconsistent, *e.g.*, in their Fig.10d, the points $(\Phi_N, \kappa) = (700, 1.93)$ and $(70, 2.05)$ should be moved to $(70, 1.93)$ and $(700, 2.05)$, respectively. In this way, the Nayak parameter Φ_N would be consistent not only with our own calculations but also with the values that Yastrebov *et al.* reported themselves in their Fig.1. Once these two data points are corrected, the logarithmic dependence seems to be much less convincing than with improperly plotted data.

The suspectable logarithmic dependence of κ on Nayak parameter motivated us to run simulations to present an independent test of the extent with which the Nayak parameter affects κ. In our simulations, we expand the range of surfaces and contrast surfaces with cutoff to those with smooth and sharp rolloffs. Results are presented in Fig. 4.6, which were averaged over up to 400 random realizations per data points.

As shown in Fig. 4.6, the averaged values of κ turn out to be consistent with a $\kappa(\Phi_N) = \kappa(\infty) - c_N \Phi_N^{-\nu_N}$ relation rather than a decreased logarithmic relation. Two different dependencies plotted in Fig. 4.6 correspond to $H = 0.3$ and $H = 0.8$ case respectively. Therefore, κ cannot be concluded to be a single function of Φ_N (and p^*), at least not possible for different Hurst exponent.

4.3.3 Anisotropic rpa surfaces

In this section, we attempt to understand how anisotropy affects the relative contact area. Towards this end, we repeated the simulations presented in Fig. 4.4 with a Peklenik number of $\gamma_P = 4$. As shown in Fig. 4.7, the pressure dependence of κ at fixed value of $\varepsilon_{t,f}$ is improved compared the ideal rpa surfaces with $\gamma_P = 1$. This result may not be particularly surprising in consideration of the observation that one-dimensional surfaces have logarithmic corrections to the $\kappa(p)$ relation, even for $H > 0.5$.

Fig. 4.7 also shows that κ is not very pressure sensitive for $H = 0.8$ when ε_f is decreased with pressure so that for macroscopic systems, in which ε_f is two or three orders of magnitude smaller than in simulations, the pressure sensitivity is marginally small. However, compared with the isotropic case, κ is apparently increased due to anisotropy. When the Peklenik number is chosen far from unity, different law may apply as the surface's dimensionality has effectively changed

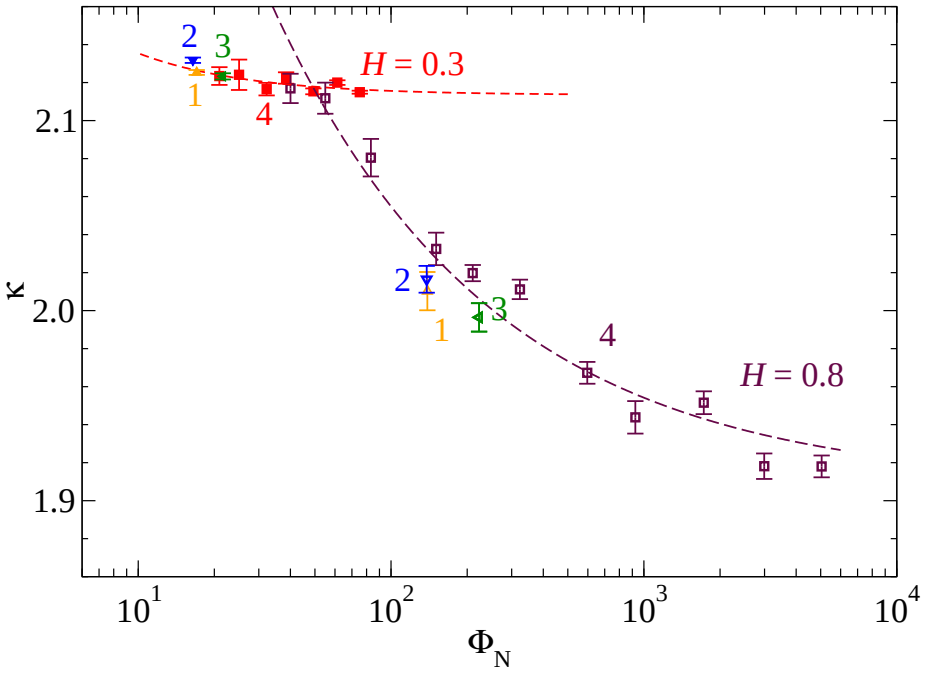

Figure 4.6: Proportionality coefficient κ as a function of the Nayak parameter $\Phi_N = 1.5\,\Phi_6$ at $p^* = 0.02$. Full and open symbols relate to $H = 0.3$ and $H = 0.8$, respectively. Different surface realizations were considered: (1) orange triangles up: cut-off, (2) blue triangles down: smooth roll-off, (3) green triangles left: hard roll-off. In these three cases, ε_t and ε_f were fixed: $\varepsilon_t = 1/4$, $\varepsilon_f = 1/125$, Finally, (4) squares: cut-off with $1/40 \leq \varepsilon_f \leq 1/1000$. The dashed lines are fits $\kappa = \kappa_\infty + c\,\Phi_N^{-\nu}$, where ν turned out to be consistent with $\nu \approx 0.5$ for $H = 0.8$ and $\nu \approx 1$ for $H = 0.3$.

from two to one. In a recent study on κ, the tendency for one-dimensional contact problem, the pressure sensitivity of κ at the zero pressure limit has been convincingly established not only for small H but also for $H = 0.8$ [42].

Additionally, regarding the anisotropic rpa surfaces, we noticed that κ_c, whose definition of reduced pressure uses the rms height gradient $\bar{g}$ averaged over the contact domain only, has a fairly weak dependence on p^*. Values of κ_c are roughly close to 1.8. Interestingly, the order of the points are essentially in reverse order compared to the analysis in which $\bar{g}$ was averaged over entire surfaces.

Lastly, as shown in Fig. 4.7, the smallest κ occurs for the smallest Hurst exponent. The explanation could be as follows: for $H = 0.3$, roughness exists mainly at small wavelengths and as a result, contact patches are rather small compared to $H = 0.8$.

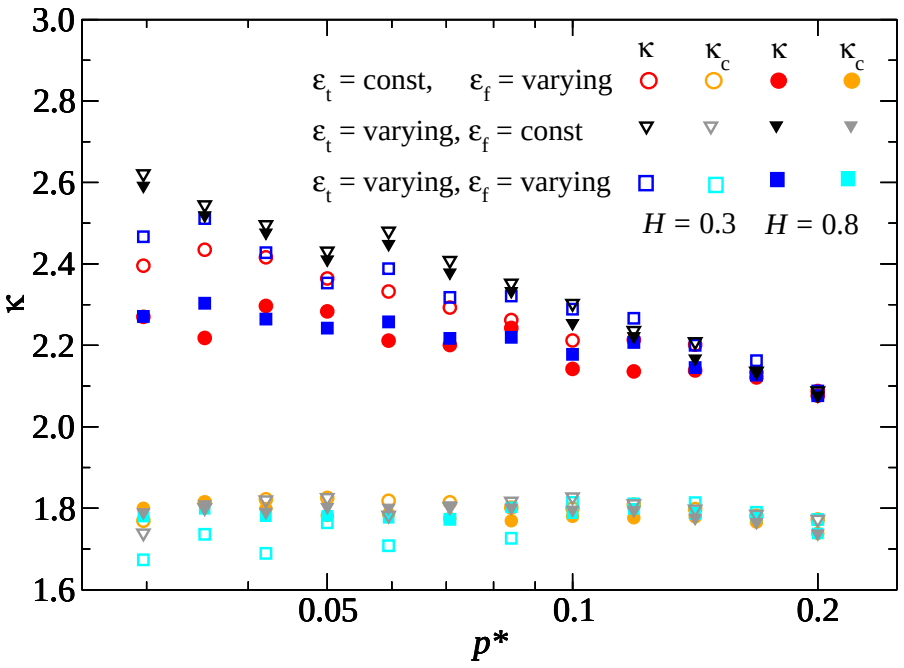

Figure 4.7: The interpretation is similar to Fig. 4.4, however, the rigid indenter used in this figure is replaced by an anisotropic indenter with $\gamma_P = 4$. The color symbols used in this figure, which are not used in the Fig. 4.4, represent results for κ_c.

The coarse grained, or rotationally averaged height profile of an individual mesoscale asperity is therefore blunter for $H = 0.8$ than $H = 0.3$.

4.3.4 Isotropic height-warped surfaces

Most of contact studies focus on the ideal, rpa surfaces with assumption of the random-phase approximation, quite a few numerical studies use a Weierstrass profile, which has phase correlation, while producing a height autocorrelation function (ACF) being similar to experimental ACFs. Nevertheless, the Weierstrass profile is far from those experimental surfaces as demonstrated in Fig.2 of Ref. [98]. This convinces us that the warping surface introduced in Sec. 4.1, while perhaps far from ideal, reproduces the stochastic properties of correlated surfaces in a significantly more realistic fashion than a Weierstrass-function based height profile.

Results are shown in Fig. 4.8. It shows that the increase of κ with decreasing pressure is much stronger for a positive warping exponent w, in which case the peaks are blunted and valleys are sharpened. In this figure, when $H = 0.8$, κ even increases with decreasing p^* when ε_f is reduced with decreasing pressure. Oppositely, the negative warping exponent leads to sharp peaks and blunt valleys. In this case, κ is found to decrease with pressure. This observation also holds in certain pressure ranges, when ε_f is not scaled according to Eq. (4.28) but kept constant.

Similar to the observation for anisotropic surfaces, κ_c turns out to be insensitive to the reduced pressure if the rms height gradient is defined in the true contact zones. Again, κ_c is generally equals to 1.8 for small reduced pressure. Correlating the respective values of κ_c with the structural parameters, which are symmetry-allowed and finite, has remained unsuccessful so far.

4.3.5 Periodically repeated smooth indenters

In this section, indenters are periodically repeated, therefore, each indenter bears the same external load. If the contact zone is relatively small compared with the period, which means, the external pressure p_0 applied on the indenter is quite small, a area-load relation must be obtained as if the indenter were isolated. According to a recent study [92], the asymptotic low pressure relation for periodically repeated indenters with harmonic height profiles can be rationalized with Eq. (4.10). The prefactor κ_c can be obtained analytically, which reads

$$\kappa_\mathrm{c}(n) = \sqrt{\frac{\pi}{n}} \frac{\Gamma(\frac{n}{2} + \frac{3}{2})}{\Gamma(\frac{n}{2} + 1)}, \tag{4.29}$$

where $\Gamma(\bullet)$ represents the gamma function. The simulation results are depicted in Fig. 4.9. It confirms the analytical results at low pressure. Even though the errors become apparent when $a_\mathrm{r} > 0.3$, they remain below 25%. The high pressure asymptotic trend could also rationalized with Eq. (4.10), however, the value of κ_c should be decreased.

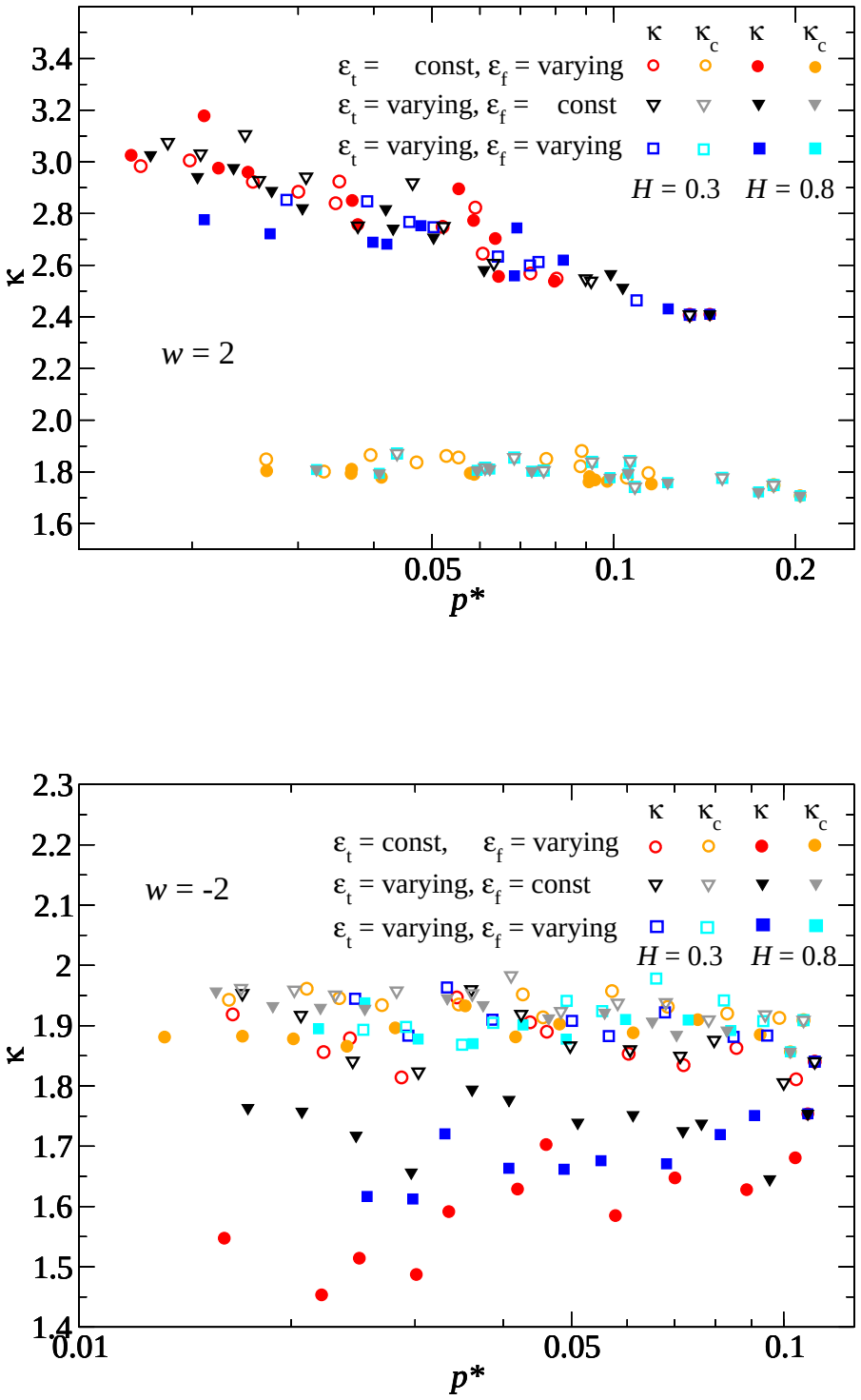

Figure 4.8: The interpretation is similar to Fig. 4.4, however, the indenter is replaced by a height warped surfaces. The top and bottom graph represents GFMD results for a warping surface with $w = 2$ and $w = -2$, respectively.

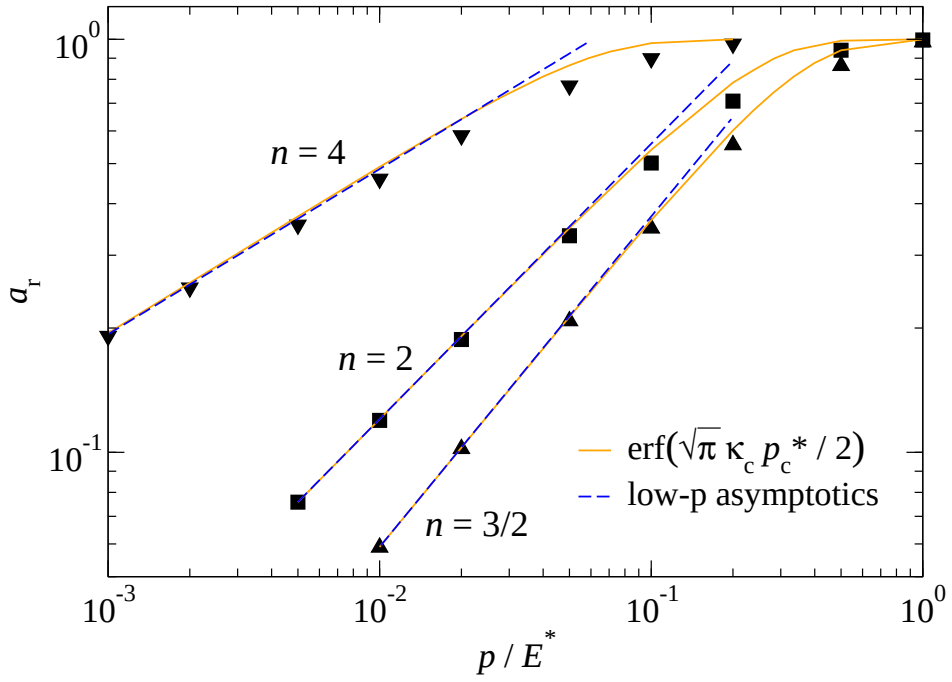

Figure 4.9: Relative contact area a_r as a function of reduced pressure p/E^* for periodically repeated indenters which are fully defined in Sec. 4.1. Symbols represent GFMD data.

4.4 Conclusion

In this study, we constructed a variety of structural parameters and attempted to determine which one could affect the relative contact area in a straightforward way. The key point was to understand if a_r is linear in pressure p and inversely proportional to the rms height gradient $\bar{g}$ for small reduced pressures, defined as $p^* = p/(E^*\bar{g})$. If the linear relation is true, what structural parameter determine the proportionality $\kappa = a_r/p^*$? Towards this end, the contact problem between an initially flat, adhesion- and frictionless, linearly elastic body and a variety of rough, rigid surfaces, including isotropic rpa surface, anisotropic rpa surface, isotropic warping surface and periodically repeated harmonic smooth surface, is studied.

One of the difficulties to validate the area-load linearity for the small-pressure limit is that taking the limit $p^* \to 0$ properly is not a simple task, because ε_t, which represents the ratio roll-off wavelength and system size, and ε_f, which indicates

the ratio of short wavelength and roll-off wavelength, have to be sufficiently small. In a previous study by Prodanov *et al.* [54], they kept the ratio of grid distance and short wavelength, $\varepsilon_c = a/\lambda_s$, fixed, which appears to be insufficient. In this study, we extrapolate results for a determined surface to the continuum limit first and then compute contact area while taking thermodynamic and fractal limit to zero simultaneously or by taking fractal limit to zero while keep thermodynamic limit constant.

The last type of analysis, in which continuum and fractal limits are set to zero, while thermodynamic limit is kept constant, and reduced pressure p^* is set to be extremely small, attracted particular attention. In this case, only a single meso-scale asperity contact could be detected for very small ε_f and Hurst exponent $H > 0.5$. The reason is that typical contact patch sizes increase algebraically with decreasing ε_f for $H > 0.5$ [96]. In an individual meso-scale asperity, which could be described as a single asperity with micro-scale roughness added to it, the linearity between contact area and pressure is well satisfied [50] and the expression can be rationalized with Persson theory [49]. Accordingly, the linearity between load and contact area in a macroscale system should be determined automatically. However, this conclusion can only hold for (2+1) dimensional systems. It was reported that in (1+1) dimensional systems, area-load relation does not follow the linear dependence at small pressure, even for very large systems [41]. This discrepancy still remains unclear to us. Additionally, the area-load dependence at small reduced pressure p^* for $H < 0.5$ surface is not determined. Even though our current analysis supports the findings [59, 61] that the area-load relation indeed has logarithmic corrections in p^*. They might be the consequence of the small, logarithmic growth of characteristic contact patch sizes with decreasing ε_f for $H < 0.5$. Meanwhile, we wonder if κ computed in the thermodynamic limit can systematically exceed predictions of the more advanced bearing-area models such as Bush, Gibson, and Thomas (BGT) [97]. Thus although we believe to have furthered the rigor with which κ is computed, we expect that the final answer to how κ has to be computed in the thermodynamic limit still needs to be found.

Additionally, it is demonstrated that the Nayak parameter Φ_N has no rigorous correlation with κ. In this case, it is not allowed the function $\kappa(p^*, H, \varepsilon_t, \varepsilon_f)$ to be reduced to a smaller number of variables, such as, $\kappa(p^*, \Phi_N, \varepsilon_t)$.

Although Persson theory cannot be used to explain why different Hurst exponent

leads to different κ, it allows us to rationalize the deviation of $\kappa(p^*)$ from linearity both for finite system and surfaces violating the rpa approximation. The basic version of Persson theory assumes that the elastic body "feels" the full root-mean-square gradient (averaged over the entire surface) as soon as the elastic body hits the rough substrate. However, for any *finite* surface, a certain fraction must be in contact before the root-mean-square gradient and other stochastic parameters, such as the curtosis, approach their "true" mean values. While this fraction decreases with system size, $\bar{g}$ (typically) remains below its asymptotic value for finite rpa surfaces at small a_r so that (according to Persson theory and simulations presented in this work) a_r turns out larger than in the thermodynamic limit. A possible correction of Persson theory for this case could be to identify the rms-gradient of the $a_\mathrm{r} \times 100\%$ top- (or bottom) most heights and use this value to determine the reduced pressure p_c^*, which would then satisfy Eq. (4.10) reasonably well. To some extent, this would constitute a somewhat dissatisfactory compromise between Persson theory and bearing-area models, since it is not the top- (or bottom) most, say, 20% of the peaks that are in contact at 20% relative contact area, as is implicitly assumed in bearing-area models. However, this is the simplest correction that comes to our mind at this point of time. It is certainly much less tedious to work out than the systematic corrections to Persson theory relying on a cumulant expansion of the short- but finite-range repulsive interactions between indenter and elastic body [23].

In full simulations, $\bar{g}$ can be averaged over the true contact area and no compromise between bearing-area models and Persson theory needs to be made. In all investigated randomly-rough contacts, we find a close-to-linear relation between a_r and p_c^*, i.e., when averaging the rms height gradient only over the true contact even if the original $a_\mathrm{r}(p)$ deviates clearly from linearity. In these simulations, we find κ_c to lie in the relatively narrow range satisfying $\kappa_\mathrm{c} \approx 1.8 \pm 0.1$. This value for κ_c is only slightly larger than the value of 1.6 predicted by Persson theory but clearly below the value of 2.5 predicted by Bush, Gibson, and Thomas [97] using an advanced bearing-area model. Thus, the range of validity of Persson theory could be substantially expanded if the approximation of using the full rms-height gradient were replaced with an accurate estimate of the mean rms-height gradient in the true contact.

Chapter 5

Thermal effects on the pull-off force in the JKR model

This chapter attempts to understand how thermal fluctuations effect the pull-off force in the JKR model. Towards this end, we set up a virtual loading-unloading experiment, in which a parabolic rigid indenter is fixed in space, an isotropic elastic solid is placed below the indenter and is connected with an elastic spring. This spring is designed to characterize the stiffness of the cantilever in AFM experiments and is allowed to move up and down with a constant velocity.

The purpose of this chapter is to study to what extent the thermal fluctuations affect the pull-off force within the formalism of the JKR model. Furthermore, this work is also expected to provide a plausible reproduction for the existing experiment results [16].

The remainder of this chapter is organized as follows: The details about the virtual loading-unloading simulation are introduced in Sec. 5.1. The method is sketched in Sec. 5.2, in which the basic idea of the numerical simulation and how we implement the thermal fluctuations are described in detail. The numerical results are presented in Sec. 5.3, while conclusions are drawn in Sec. 5.4.

5.1 Model design

In this section, the details about the loading-unloading simulation are introduced. As shown in Fig. 5.1, the elastic body is designed as initially flat and lineally elastic, which is placed in the xy plane and below $z = 0$. The parabolic rigid counterface is fixed in space and the profile is given by

$$h(\mathbf{r}) = \frac{r^2}{2R} \tag{5.1}$$

where R denotes the radius of curvature, $r = \sqrt{x^2 + y^2}$ is the in-plane distance of the center of the counterface from the center of the coordinate system. The elastic body is connected to an elastic spring with stiffness k, which is allowed to move along the z direction at constant velocity v_{spr}.

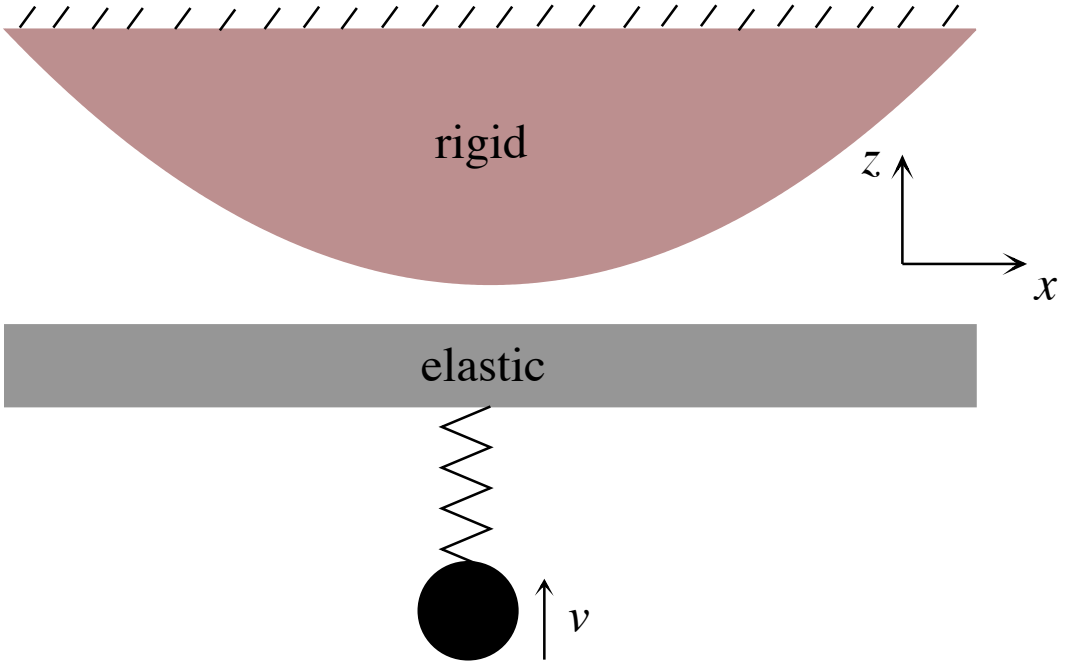

Figure 5.1: Schematic illustration showing the set up of a tip-substrate model for an loading-unloading simulation.

The interaction between the elastic body and the rigid counterface is defined as the same as that in the JKR model [3], in which case the short-ranged adhesion is assumed as a delta function of strength γ, hence it only exists within the contact domain. The contact force F_{cont} as a function of indentation d can be determined

jointly by [99]

$$F_{\mathrm{cont}} = \frac{4E^*}{3R}a_{\mathrm{c}}^3 - \sqrt{8\pi\gamma E^*}a_{\mathrm{c}}^{3/2} \tag{5.2}$$

$$d = \frac{a_{\mathrm{c}}^2}{R} - \sqrt{\frac{2\pi\gamma}{E^*}}a_{\mathrm{c}}^{1/2} \tag{5.3}$$

where E^* is the contact modulus and a_{c} the contact area. The resulting pull-off force F in the JKR model for the athermal case is given by

$$F = -\frac{3}{2}\pi\gamma R \tag{5.4}$$

which is independent of the contact modulus [3]. To discriminate the athermal pull-off force from the thermal pull-off force, the short-hand notation F_0 will be used to indicate the pull-off force in athermal case.

The loading-unloading process of a certain simulation can be described as follows: The elastic spring, which is used to characterize the cantilever, moves to the rigid counterface with a constant velocity. Consequently, the elastic body begins to move due to the work of the spring force and comes into contact with the rigid counterface at $z = 0$. The elastic body continues to indent for some distance. After that, the spring begins to move in the opposite direction, which represents the beginning of the unloading process.

In an AFM experiment, the interaction between the tip and the counterface will result in the vertical deflection of the cantilever beam. As a result, the applied force can be deduced from the deflection according to Hooke's law [100, 101]. In MD simulations, the cantilever beam is modeled by coupling a harmonic spring to the bottom layer of the elastic body [102]. In such a way, the force F_{spr} which is measured by the spring, is defined as

$$F_{\mathrm{spr}} = -k\left(u_{\mathrm{spr}} - u_{\mathrm{ela}}\right) \tag{5.5}$$

where u_{spr} denotes the normal displacement of the spring and u_{ela} the normal displacement of the elastic body.

5.2 Method

Bradley's model has been widely used to calculate the pull-off force between two spheres by assuming that the interaction is nothing but a Lennard-Jones (LJ) potential [16, 103, 104]. In such a way, if the indenter is supposed to be controlled by an elastic spring, the total potential energy realized by this spring can be given as below

$$V_{\mathrm{tot}} = \frac{1}{2}k\left(u_{\mathrm{spr}} - u_{\mathrm{ela}}\right)^2 - \frac{4\gamma}{3}\left[\left(\frac{\rho_0}{u_{\mathrm{ela}}}\right)^2 - \frac{1}{4}\left(\frac{\rho_0}{u_{\mathrm{ela}}}\right)^8\right] \tag{5.6}$$

where ρ_0 has the unit of length. This model estimated the pull-off force as $F = -2\pi\gamma R$, which is identical to the value of that in the Derjaguin-Muller-Toporov (DMT) model [4]. It has been demonstrated several times that the DMT model is accurate in the case of the long-range adhesion and stiff material [32, 105, 106]. Unfortunately, this model becomes increasingly inaccurate for large and soft matter, hence different assumptions on the interaction have led to the Johnson-Kendall-Roberts (JKR) model [3], in which a singular crack term is assumed near the contact line.

This just motivates us to replace the LJ potential with a JKR contact force and to study to what extent the thermal fluctuations affect the pull-off force in the framework of the JKR model. Therefore, we rewrite the total potential V_{tot} as follows.

$$V_{\mathrm{tot}} = \frac{1}{2}k\left(u_{\mathrm{spr}} - u_{\mathrm{ela}}\right)^2 - \int_0^{u_{\mathrm{ela}}} \mathrm{d}u F_{\mathrm{cont}} \tag{5.7}$$

where the contact force F_{cont} is naturally invoked only in the contact zone.

To simulate the loading-unloading process, we solve Newton's equations of motion as described below.

$$m\ddot{u}_{\mathrm{ela}} + m\eta\left(\dot{u}_{\mathrm{ela}} - \dot{u}_{\mathrm{spr}}\right) = -\frac{\partial V_{\mathrm{tot}}}{\partial u_{\mathrm{ela}}} \tag{5.8}$$

The effect of thermal fluctuations can be cast as random forces, which have to satisfy the fluctuation-dissipation-theorem (FDT) [85]. Hence, the mean and second moment of random forces $\Gamma(t)$ must obey

$$\langle\Gamma(t)\rangle = 0 \tag{5.9}$$

$$\langle\Gamma(t)\Gamma(t')\rangle = 2\eta k_B T\delta(t - t') \tag{5.10}$$

respectively, where η represents a damping constant of unit inverse time and $\delta(\cdot)$ denotes the Dirac delta function, k_B is the Boltzmann constant and T is temperature, $\langle\cdot\rangle$ represents ensemble average.

To include the thermal fluctuations, we rewrite the Eq.(5.8) as follows.

$$m\ddot{u}_{\mathrm{ela}} + m\eta\left(\dot{u}_{\mathrm{ela}} - \dot{u}_{\mathrm{spr}}\right) = -\frac{\partial V_{\mathrm{tot}}}{\partial u_{\mathrm{ela}}} + \Gamma_{\mathrm{spr}}(t) + \Gamma_{\mathrm{cont}}(t) \tag{5.11}$$

Similar to the contact force, the random force $\Gamma_{\mathrm{cont}}(t)$, which is used to characterize the thermal effects during the contact process, is also assumed to be realized only in the contact domain. Another random force term Γ_{spr}, which is used to simulate the thermal effects on the spring, however, is assumed to exist throughout the simulation.

The displacement of the elastic spring $u_{\mathrm{spr}} = v_{\mathrm{spr}}\Delta t$ as it is restricted to move at constant velocity, where Δt is time step. The displacement of the elastic body u_{ela}, however, is controlled by the spring and the interaction force jointly. In this case, we use the following scheme to propagate the displacement of the elastic body.

$$u_{\mathrm{ela}}^{\mathrm{now}} = u_{\mathrm{ela}}^{\mathrm{old}} + \dot{u}_{\mathrm{ela}}^{\mathrm{now}}\Delta t \tag{5.12}$$

$$\dot{u}_{\mathrm{ela}}^{\mathrm{now}} = \dot{u}_{\mathrm{ela}}^{\mathrm{old}} + \ddot{u}_{\mathrm{ela}}\Delta t \tag{5.13}$$

The implementation of JKR-MD in terms of pseudo code works as follows:

```
loop over time steps until the stop request is applied
```
- `move elastic spring`
  $u_{\mathrm{spr}} += \dot{u}_{\mathrm{spr}}\Delta t$
- `if the retract request is applied, change velocity direction`
  $\dot{u}_{\mathrm{spr}} \times = -1$
- `move elastic indenter`
  $u_{\mathrm{ela}} += \dot{u}_{\mathrm{ela}}\Delta t$
- `calculate the elastic force`
  $F_{\mathrm{ela}} = k\left(u_{\mathrm{spr}} - u_{\mathrm{ela}}\right)$
- `calculate random force on elastic spring due to thermal fluctuations`
  $F_{\mathrm{ela}} += \Gamma_{\mathrm{ela}}(t)$
- `calculate contact JKR force`
  $F_{\mathrm{ela}} += F_{\mathrm{cont}}$
- `calculate random force in contact domain`
  $F_{\mathrm{ela}} += \Gamma_{\mathrm{cont}}(t)$

- propagate the velocity of the elastic body
  $\dot{u}_{\text{ela}} += F_{\text{ela}}/\Delta t$

end loop

5.3 Results

In this section, we investigate to what extent the thermal fluctuations results in the deviation of the pull-off force. As a first glance, Fig. 5.2 shows a force-displacement hysteresis of a single loading-unloading simulation considering both the contact force and the thermal fluctuations as described in previous section. To obtain this curve, the contact modulus E^* is chosen to be 40 GPa, which represents a typical oxidized silicon surface. The radius of curvature is fixed to $R = 11.8$ nm. The surface energy is $\gamma = 42$ mJ/m^2 and the spring stiffness is $k = 0.005$ N/m. Room temperature ($T = 300$ K) is applied. These values are motivated by the experimental setup of Ref. [107].

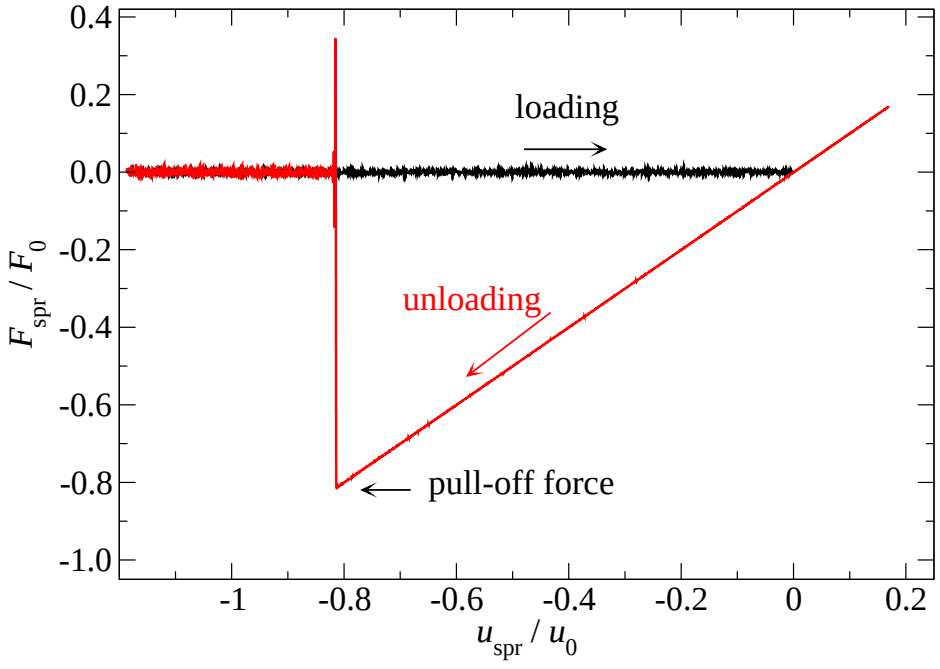

Figure 5.2: The dimensionless spring force F_{spr}/F_0 as a function of the dimensionless spring displacement u_{spr}/u_0 in an loading-unloading simulation, where u_0 represents the spring displacement at pull-off point for an athermal case.

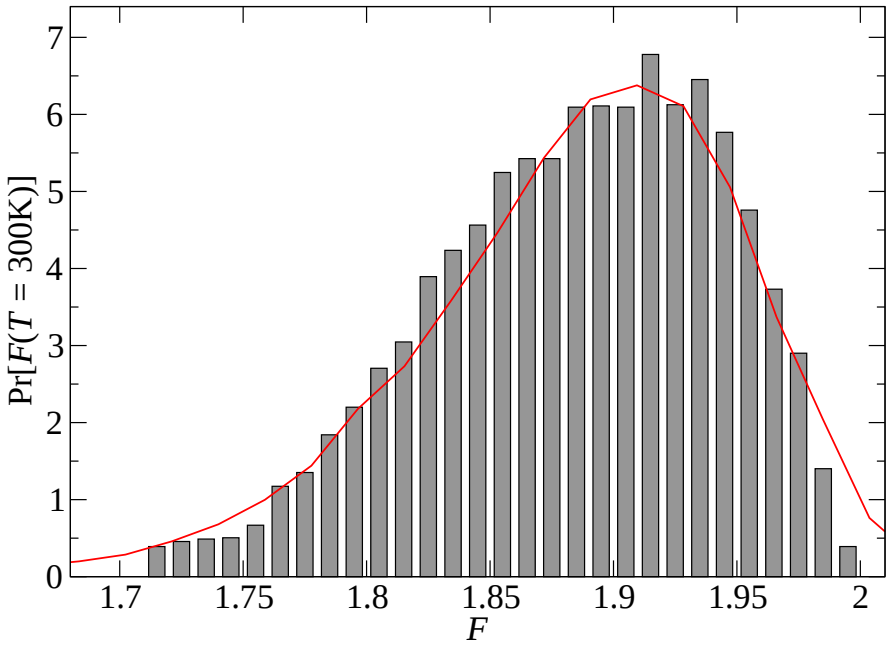

Figure 5.3: An experimental pull-off force probability reported in Fig.5 of Ref. [107], while the data is renormalized so that the integration equals to one. The red line represents the probability curve obtained using simulation with adjustable parameters.

To further demonstrate that this simulation can realistically reflect the experiment, we measured the probability distribution curve of the pull-off force from a mass of loading-unloading simulations, and compared our data to the existing data from the real experiment. Results are shown in Fig. 5.3: the grey histogram is the probability to measure a specific pull-off force, which is obtained from a large number of AFM experiments [107].

Some crucial information of the experiment, which should be helpful to our simulation are summarized as below: Both surfaces and tips are silicon oxide, in which case elastic modulus $E = 74$ GPa and $\nu = 0.17$ are applied. All AFM tips of the probes had a radius of curvature around 10 nm. The normal stiffness $k_{\rm spr}$ was of order 10^{-3} N/m, which represents a compliant cantilever is applied. Experiments are conducted at room temperature. Parameters utilized in our simulations are identical to those values applied to get the hysteresis curve in Fig. 5.2, which remains similar to the experiment parameters. The probability distribution (solid

red line) is obtained over 20, 000 loading-unloading curves and it roughly coincides with the distribution obtained from experiments.

Fig. 5.4 shows plots of pull-off force histogram with different temperatures using the JKR-MD introduced in Sect. 5.2. MD results can be described as an asymmetric bell shape and can be perfectly fitted using the Gumbel distribution with adjustable parameters, which is given by

$$\Pr[F] = \frac{1}{\beta} e^{-z-e^{-z}} \tag{5.14}$$

with

$$z = \frac{F-\mu}{\beta}, \tag{5.15}$$

where μ is the mode of the Gumbel distribution, that is, the most likely value for pull-off force to occur, and β represents a parameter to determine the bell shape.

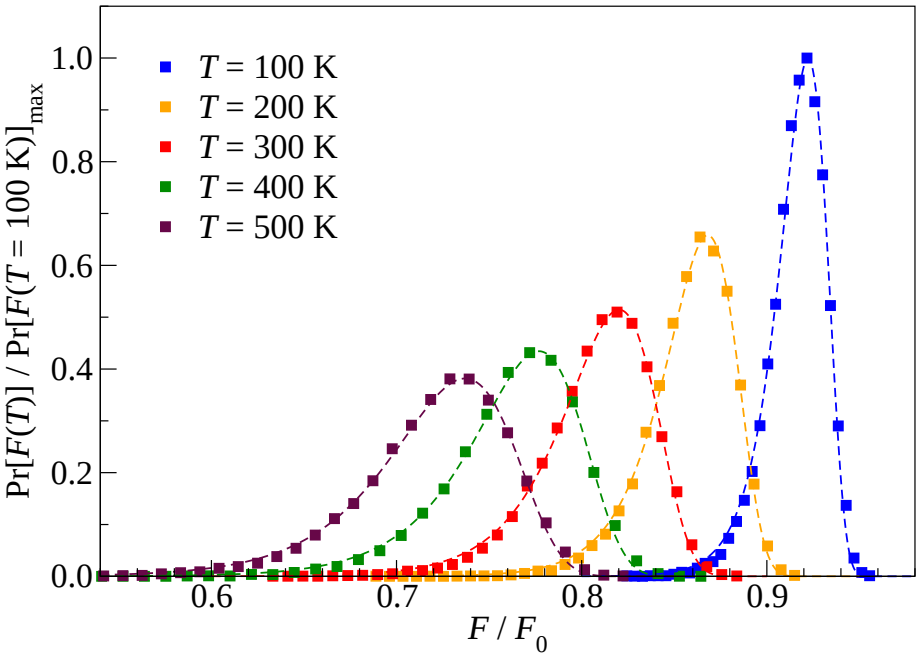

Figure 5.4: Normalized probability density function of pull-off force with various temperatures. Solid squares indicates the JKR-MD results while dashed lines represent fitting lines using the Gumbel distribution.

As shown in this figure, the distributions of pull-off force are expanded with increasing temperature, a remarkable reduction of pull-off force is also realized at the

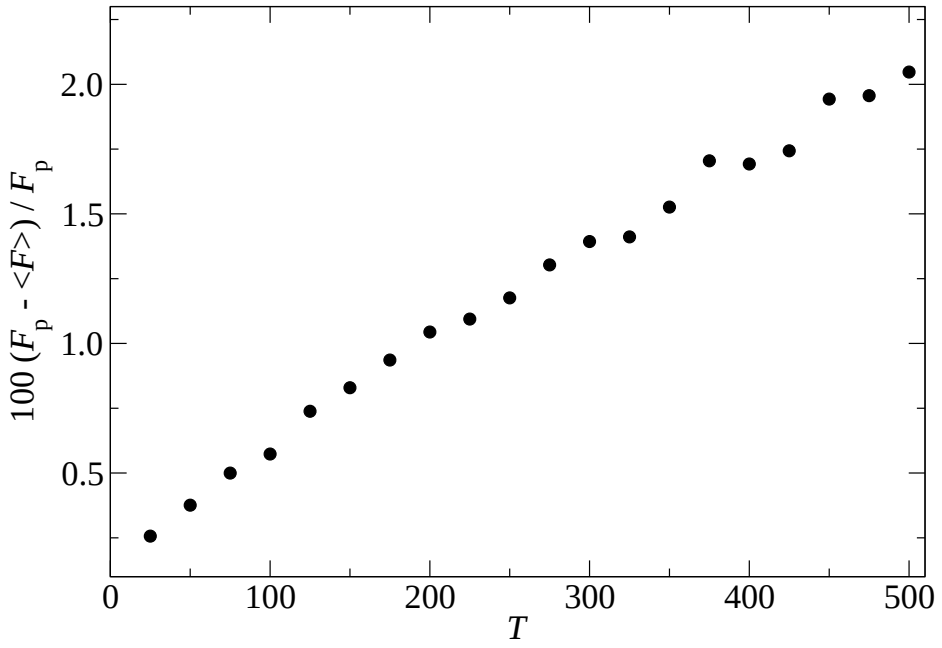

Figure 5.5: The deviation of average pull-off force from F_{p} as a function of temperature T.

same time. As an example, the most likely pull-off force F_{p}/F_0 decreases from 0.9 to 0.75 as temperature increases from 100 K to 500 K. This result indicates that the thermal fluctuations contribute to the process in which an AFM tip probes jump-out-of-contact dynamics.

We would like to argue that the significant reduction of the pull-off force stems from the effects of thermal fluctuations as it is the only additional factor considered in this study. A possible explanation could be that the thermal fluctuations lead to a reduction of the surface energy. In this case, a particle of the elastic body is more likely to jump to another local minimum, which represents the case to jump out of contact, even though in the case where the pulling force is relatively small.

Fig. 5.5 presents the temperature dependence of bias of pull-off force from F_{p}. The trend shows that the deviation increases with increasing temperature, which shows F_{p} decreases with temperature assuming the surface energy to be constant.

5.4 Conclusions

In this chapter, we proposed a modified Bradley's model, in which the LJ interaction is replaced by a JKR contact model, to simulate the loading-unloading process of a typical AFM tip. Therefore, an extremely short-ranged adhesion between counterfaces is assumed in this model. Thermal effects are included by considering a Langevin thermostats, which satisfies the FDT.

To validate the reliability of this model, we analysed a large number of loading-unloading curves such that a probability distribution of pull-off force was achieved. The distribution obtained from our simulation turned out similar to the experimental result, which recognized adjusting parameters.

Furthermore, we explored the distribution of the pull-off force with different temperatures. It shows that even at room temperature, i.e., $T = 300$ K, the pull-off force is already reduced by 20% compared to the athermal case. This reduction increases with increasing temperature. Meanwhile, thermal fluctuation can also benefit the broadening of pull-off force distribution, which has also been observed experimentally [16].

Even though this crude work managed to reproduce the experiment results, there are some interesting issues still remain unsolved due to time limit, which are expected to be investigated in future works.

First, the issue how thermal fluctuations affect the surface energy still remains open. Intuitively, thermal fluctuations reduce the adhesion strength, however, the quantitative relation between temperature and surface energy is not yet determined. One can start this issue by studying the flat-flat adhesion contact problem using Green's function molecular dynamics (GFMD), which is an efficient method to get the linear response of an elastic solid with various boundary conditions [7].

Second, it has been demonstrated that the model introduced in this chapter can reproduce the experiment result quite reasonably. In light of this fact, it is also worth some effort to get the probability distribution function other than a simple fitting curve.

Chapter 6

Conclusions and outlook

In this thesis, the first contribution is to build up an efficient contact mechanics simulation toolbox. Towards this end, the fast-inertial-relaxation-engine (FIRE), which is a minimization method that can locate a minimum of the potential energy quickly, was implemented into the regular Green functional molecular dynamics (GFMD). GFMD is a method which translates a contact-mechanics problem, or generally, a boundary-value problem into the framework of molecular dynamics. Two contact mechanics benchmarks were introduced to validate the reliability of this new toolbox. The first benchmark is a simple parabolic indenter in contact with a weakly adhesive, linearly elastic solid of finite thickness. The second benchmark is a nominally flat indenter with random roughness in contact with a weakly adhesive, linearly elastic solid of finite thickness. It was demonstrated that FIRE was successfully implemented during this thesis into a regular GFMD and leads to a remarkable speedup of one order of magnitude for typical system sizes and even larger speedups for larger systems. Furthermore, because GFMD propagates displacement in Fourier space, at this point, another prominent speedup was obtained through an effective choice for the inertia of the modes. The conclusions obtained in this thesis indicated that FIRE could also benefit finite-element methods, which is another approximation method access to the solution of boundary value problem.

The second contribution is to investigate the effect of thermal fluctuations on contact mechanics in the case of hard wall constraint. Towards this end, the analytical expression of the repulsive force resulted from thermal fluctuations was derived. To validate the analytical results, the GFMD technique was generalized to include thermal noise, which satisfies fluctuation dissipation theorem. The simulation results were consistent with different mean-field approximations to the problem,

which allows us to determine a closed-form analytical distance-force expression for a flat, thermal elastic layer interacting with a flat, rigid substrate. After that, an application of this method was a traditional Hertzian contact problem which thermal fluctuations were added to validate this method. It was shown that thermal fluctuation can induce non-negligible shifts in the normal displacement. This displacement was found to be roughly equal to the root-mean-square fluctuation of surface atoms but almost independent of the load.

The third contribution of this thesis is the study on the dependence of relative contact area on pressure for nominally flat surface contact problem. Some studies claimed that the area-pressure relation should follow a rigorous linearity. However, the proportionality of relative contact area and pressure remains unclear. Therefore, it is meaningful to study if there are any structural parameter to correlate with this proportionality. For this reason, the relative contact area between an initially flat, adhesion- and frictionless, linearly elastic body and a variety of rough, rigid substrate is studied using GFMD. It is found that the linearity can only hold if the root-mean-square height gradient evaluated over the real contact area. No single unitless structural parameter, including the Nayak parameter, correlate to the proportionality.

On the basis of the work presented in this thesis, further extensions should be considered. First, since FIRE was demonstrated to be efficient to the solution of boundary-element method, it should also benefit the solution of finite element method. It is meaningful to implement the FIRE algorithm into any existing finite element method toolbox. Second, regarding the effect of thermal fluctuation on pressure-distance relation, only hard-wall constraint is included. A more general case should include the surface force, *e.g.*, van der Waals forces since the surface force starts to dominate with decreasing the length scale. Therefore, it would be interesting to study the effect of thermal noise on the pressure-distance relation for adhesive contacts.

List of Figures

List of Tables

Bibliography

[1] Heinrich Hertz. Ueber die beruhrung fester elastischer korper. *J reine angew Math*, 92:156–171, 1882.

[2] F. P. Bowden, D. Tabor, and Frederic Palmer. The friction and lubrication of solids. *American Journal of Physics*, 19(7):428–429, October 1951. doi: 10.1119/1.1933017. URL https://doi.org/10.1119/1.1933017.

[3] Kenneth Langstreth Johnson, Kevin Kendall, and A.D. Roberts. Surface energy and the contact of elastic solids. *Proceedings of the Royal Society of London. A. Mathematical and Physical Sciences*, 324(1558):301–313, September 1971. doi: 10.1098/rspa.1971.0141. URL https://doi.org/10.1098/rspa.1971.0141.

[4] B.V Derjaguin, V.M Muller, and Yu.P Toporov. Effect of contact deformations on the adhesion of particles. *Journal of Colloid and Interface Science*, 53(2):314–326, November 1975. doi: 10.1016/0021-9797(75)90018-1. URL https://doi.org/10.1016/0021-9797(75)90018-1.

[5] I. A. Polonsky and L. M. Keer. Fast methods for solving rough contact problems: A comparative study. *Journal of Tribology*, 122(1):36–41, April 1999. doi: 10.1115/1.555326. URL https://doi.org/10.1115/1.555326.

[6] R. Bugnicourt, P. Sainsot, D. Dureisseix, C. Gauthier, and A. A. Lubrecht. FFT-based methods for solving a rough adhesive contact: Description and convergence study. *Tribology Letters*, 66(1), January 2018. doi: 10.1007/s11249-017-0980-z. URL https://doi.org/10.1007/s11249-017-0980-z.

[7] Carlos Campaná and Martin H Müser. Practical green's function approach to the simulation of elastic semi-infinite solids. *Physical Review B*, 74(7):075420, 2006.

[8] B. N. J. Persson, O. Albohr, U. Tartaglino, A. I. Volokitin, and E. Tosatti. On the nature of surface roughness with application to contact mechanics, sealing, rubber friction and adhesion. *Journal of Physics: Condensed Matter*, 17(1):R1–R62, dec 2004. doi: 10.1088/0953-8984/17/1/r01. URL http://dx.doi.org/10.1088/0953-8984/17/1/R01.

[9] A. Tiwari, L. Dorogin, M. Tahir, K. W. Stöckelhuber, G. Heinrich, N. Espallargas, and B. N. J. Persson. Rubber contact mechanics: adhesion, friction and leakage of seals. *Soft Matter*, 13(48):9103–9121, 2017. doi: 10.1039/c7sm02038d. URL https://doi.org/10.1039/c7sm02038d.

[10] B. Lorenz and B. N. J. Persson. Leak rate of seals: Effective-medium theory and comparison with experiment. *The European Physical Journal E*, 31(2): 159–167, February 2010. doi: 10.1140/epje/i2010-10558-6. URL https://doi.org/10.1140/epje/i2010-10558-6.

[11] Wolf B. Dapp and Martin H. Müser. Fluid leakage near the percolation threshold. *Scientific Reports*, 6(1), February 2016. doi: 10.1038/srep19513. URL https://doi.org/10.1038/srep19513.

[12] Y. P. Zhao, L. S. Wang, and T. X. Yu. Mechanics of adhesion in MEMS—a review. *Journal of Adhesion Science and Technology*, 17(4):519–546, January 2003. doi: 10.1163/15685610360554393. URL https://doi.org/10.1163/15685610360554393.

[13] C.K. Bora, E.E. Flater, M.D. Street, J.M. Redmond, M.J. Starr, R.W. Carpick, and M.E. Plesha. Multiscale roughness and modeling of MEMS interfaces. *Tribology Letters*, 19(1):37–48, May 2005. doi: 10.1007/s11249-005-4263-8. URL https://doi.org/10.1007/s11249-005-4263-8.

[14] B. N. J. Persson and M. Scaraggi. Theory of adhesion: Role of surface roughness. *The Journal of Chemical Physics*, 141(12):124701, September 2014. doi: 10.1063/1.4895789. URL https://doi.org/10.1063/1.4895789.

[15] A. Tiwari, L. Dorogin, A. I. Bennett, K. D. Schulze, W. G. Sawyer, M. Tahir, G. Heinrich, and B. N. J. Persson. The effect of surface roughness and viscoelasticity on rubber adhesion. *Soft Matter*, 13(19):3602–3621, 2017. doi: 10.1039/c7sm00177k. URL https://doi.org/10.1039/c7sm00177k.

[16] A. V. Pinon, M. Wierez-Kien, A. D. Craciun, N. Beyer, J. L. Gallani, and M. V. Rastei. Thermal effects on van der waals adhesive forces. *Physical Review B*, 93(3), January 2016. doi: 10.1103/physrevb.93.035424. URL https://doi.org/10.1103/physrevb.93.035424.

[17] Yi Sang, Martin Dubé, and Martin Grant. Thermal effects on atomic friction. *Physical Review Letters*, 87(17), October 2001. doi: 10.1103/physrevlett.87.174301. URL https://doi.org/10.1103/physrevlett.87.174301.

[18] Jan-Michael Y. Carrillo and Andrey V. Dobrynin. Dynamics of nanoparticle adhesion. *The Journal of Chemical Physics*, 137(21):214902, December 2012. doi: 10.1063/1.4769389. URL https://doi.org/10.1063/1.4769389.

[19] D. Tabor. Surface forces and surface interactions. *Journal of Colloid and Interface Science*, pages 3–14, 1977. doi: 10.1016/b978-0-12-404501-9.50009-2. URL https://doi.org/10.1016/b978-0-12-404501-9.50009-2.

[20] K. L. Johnson. Adhesion and friction between a smooth elastic spherical asperity and a plane surface. *Proceedings of the Royal Society of London. Series A: Mathematical, Physical and Engineering Sciences*, 453(1956):163–179, January 1997. doi: 10.1098/rspa.1997.0010. URL https://doi.org/10.1098/rspa.1997.0010.

[21] J.A. Greenwood and J.B.P. Williamson. Contact of nominally flat surfaces. *Proceedings of the Royal Society of London. Series A. Mathematical and Physical Sciences*, 295(1442):300–319, December 1966. doi: 10.1098/rspa.1966.0242. URL https://doi.org/10.1098/rspa.1966.0242.

[22] K.N.G. Fuller and D. Tabor. The effect of surface roughness on the adhesion of elastic solids. *Proceedings of the Royal Society of London. A. Mathematical and Physical Sciences*, 345(1642):327–342, September 1975. doi: 10.1098/rspa.1975.0138. URL https://doi.org/10.1098/rspa.1975.0138.

[23] Martin H. Müser. Rigorous field-theoretical approach to the contact mechanics of rough elastic solids. *Physical Review Letters*, 100(5), February 2008. doi: 10.1103/physrevlett.100.055504. URL https://doi.org/10.1103/physrevlett.100.055504.

[24] B. N. J. Persson. Theory of rubber friction and contact mechanics. *The Journal of Chemical Physics*, 115(8):3840, 2001. doi: 10.1063/1.1388626. URL http://dx.doi.org/10.1063/1.1388626.

[25] Carlos Campañá, Martin H Müser, and Mark O Robbins. Elastic contact between self-affine surfaces: comparison of numerical stress and contact correlation functions with analytic predictions. *Journal of Physics: Condensed Matter*, 20(35):354013, August 2008. doi: 10.1088/0953-8984/20/35/354013. URL https://doi.org/10.1088/0953-8984/20/35/354013.

[26] B.N.J. Persson. Contact mechanics for randomly rough surfaces. *Surface Science Reports*, 61(4):201–227, June 2006. doi: 10.1016/j.surfrep.2006.04.001. URL https://doi.org/10.1016/j.surfrep.2006.04.001.

[27] A. Almqvist, C. Campañá, N. Prodanov, and B.N.J. Persson. Interfacial separation between elastic solids with randomly rough surfaces: Comparison between theory and numerical techniques. *Journal of the Mechanics and Physics of Solids*, 59(11):2355–2369, November 2011. doi: 10.1016/j.jmps.2011.08.004. URL https://doi.org/10.1016/j.jmps.2011.08.004.

[28] J. F. Archard. Contact and rubbing of flat surfaces. *Journal of Applied Physics*, 24(8):981–988, August 1953. doi: 10.1063/1.1721448. URL https://doi.org/10.1063/1.1721448.

[29] A. Majumdar and C.L. Tien. Fractal characterization and simulation of rough surfaces. *Wear*, 136(2):313–327, March 1990. doi: 10.1016/0043-1648(90)90154-3. URL https://doi.org/10.1016/0043-1648(90)90154-3.

[30] B. N. J. Persson. On the fractal dimension of rough surfaces. *Tribology Letters*, 54(1):99–106, March 2014. doi: 10.1007/s11249-014-0313-4. URL https://doi.org/10.1007/s11249-014-0313-4.

[31] Carmine Putignano, Luciano Afferrante, Giuseppe Carbone, and Giuseppe P. Demelio. A multiscale analysis of elastic contacts and percolation threshold for numerically generated and real rough surfaces. *Tribology International*, 64:148–154, August 2013. doi: 10.1016/j.triboint.2013.03.010. URL https://doi.org/10.1016/j.triboint.2013.03.010.

[32] D. S. Grierson, E. E. Flater, and R. W. Carpick. Accounting for the JKR–DMT transition in adhesion and friction measurements with atomic force microscopy. *Journal of Adhesion Science and Technology*, 19(3-5):291–311, January 2005. doi: 10.1163/1568561054352685. URL https://doi.org/10.1163/1568561054352685.

[33] Yijie Jiang, Judith A. Harrison, J. David Schall, Kathleen E. Ryan, Robert W. Carpick, and Kevin T. Turner. Correcting for tip geometry effects in molecular simulations of single-asperity contact. *Tribology Letters*, 65(3), May 2017. doi: 10.1007/s11249-017-0857-1. URL https://doi.org/10.1007/s11249-017-0857-1.

[34] B Lorenz and B N J Persson. Interfacial separation between elastic solids with randomly rough surfaces: comparison of experiment with theory. *Journal of Physics: Condensed Matter*, 21(1):015003, December 2008. doi: 10.1088/0953-8984/21/1/015003. URL https://doi.org/10.1088/0953-8984/21/1/015003.

[35] S. Hyun, L. Pei, J.-F. Molinari, and M. O. Robbins. Finite-element analysis of contact between elastic self-affine surfaces. *Physical Review E*, 70(2): 026117, aug 2004. doi: 10.1103/physreve.70.026117. URL http://dx.doi.org/10.1103/PhysRevE.70.026117.

[36] C Yang and B N J Persson. Contact mechanics: contact area and interfacial separation from small contact to full contact. *Journal of Physics: Condensed Matter*, 20(21):215214, April 2008. doi: 10.1088/0953-8984/20/21/215214. URL https://doi.org/10.1088/0953-8984/20/21/215214.

[37] K. Y. Wang, Q. H. Qin, Y. L. Kang, J. S. Wang, and C. Y. Qu. A direct constraint-trefftz FEM for analysing elastic contact problems. *International Journal for Numerical Methods in Engineering*, 63(12):1694–1718, 2005. doi: 10.1002/nme.1333. URL https://doi.org/10.1002/nme.1333.

[38] Syam P Venugopalan, Lucia Nicola, and Martin H Müser. Green's function molecular dynamics: Including finite heights, shear, and body fields. *Modelling and Simulation in Materials Science and Engineering*, 25(3):034001, 2017.

[39] Martin H. Müser, Wolf B. Dapp, Romain Bugnicourt, Philippe Sainsot, Nicolas Lesaffre, Ton A. Lubrecht, Bo N. J. Persson, Kathryn Harris, Alexander Bennett, Kyle Schulze, Sean Rohde, Peter Ifju, W. Gregory Sawyer, Thomas Angelini, Hossein Ashtari Esfahani, Mahmoud Kadkhodaei, Saleh Akbarzadeh, Jiunn-Jong Wu, Georg Vorlaufer, András Vernes, Soheil Solhjoo, Antonis I. Vakis, Robert L. Jackson, Yang Xu, Jeffrey Streator, Amir Rostami, Daniele Dini, Simon Medina, Giuseppe Carbone, Francesco Bottiglione, Luciano Afferrante, Joseph Monti, Lars Pastewka, Mark O. Robbins, and James A. Greenwood. Meeting the contact-mechanics challenge. *Tribology Letters*, 65(4), August 2017. doi: 10.1007/s11249-017-0900-2. URL https://doi.org/10.1007/s11249-017-0900-2.

[40] Martin H Müser. Single-asperity contact mechanics with positive and negative work of adhesion: Influence of finite-range interactions and a continuum description for the squeeze-out of wetting fluids. *Beilstein J. Nanotechnol.*, 5:419–437, apr 2014. doi: 10.3762/bjnano.5.50. URL `http://dx.doi.org/10.3762/bjnano.5.50`.

[41] Jan Steven van Dokkum and Lucia Nicola. Green's function molecular dynamics including viscoelasticity. *Modelling and Simulation in Materials Science and Engineering*, 27(7):075006, August 2019. doi: 10.1088/1361-651x/ab3031. URL `https://doi.org/10.1088/1361-651x/ab3031`.

[42] J. S. van Dokkum, M. Khajeh Salehani, N. Irani, and L. Nicola. On the proportionality between area and load in line contacts. *Tribology Letters*, 66(3), August 2018. doi: 10.1007/s11249-018-1061-7. URL `https://doi.org/10.1007/s11249-018-1061-7`.

[43] J. Nocedal and S.J Wright. *Numerical Optimization*. Springer, New York, 1996.

[44] W.H. Press, B.P. Flannery, S.A. Teukolsky, and W.T. Vetterling. *Numerical Recipes in C*. Cambridge University, UK, 1997.

[45] A.R. Leach. *Molecular Modelling: Principles and Applications*. Prentice Hall, UK, 2001.

[46] T. Schlick. *Molecular Modelling and simulation: An Interdisciplinary Guide, Interdisciplinary Applied Mathematics*, volume 21. Springer, New York, 2002.

[47] Erik Bitzek, Pekka Koskinen, Franz Gähler, Michael Moseler, and Peter Gumbsch. Structural relaxation made simple. *Physical review letters*, 97 (17):170201, 2006.

[48] EG Karpov, GJ Wagner, and Wing Kam Liu. A green's function approach to deriving non-reflecting boundary conditions in molecular dynamics simulations. *International Journal for Numerical Methods in Engineering*, 62(9): 1250–1262, 2005.

[49] Martin H Müser. On the contact area of nominally flat hertzian contacts. *Tribology Letters*, 64(1):14, 2016.

[50] Lars Pastewka and Mark O Robbins. Contact area of rough spheres: Large scale simulations and simple scaling laws. *Applied Physics Letters*, 108(22): 221601, 2016.

[51] G. Carbone and F. Bottiglione. Asperity contact theories: Do they predict linearity between contact area and load? *Journal of the Mechanics and Physics of Solids*, 56(8):2555–2572, aug 2008. doi: 10.1016/j.jmps.2008.03.011. URL http://dx.doi.org/10.1016/j.jmps.2008.03.011.

[52] C. Campañá and M. H. Müser. Contact mechanics of real vs. randomly rough surfaces: A Green's function molecular dynamics study. *Europhysics Letters (EPL)*, 77(3):38005, jan 2007. doi: 10.1209/0295-5075/77/38005. URL http://dx.doi.org/10.1209/0295-5075/77/38005.

[53] C. Putignano, L. Afferrante, G. Carbone, and G. Demelio. The influence of the statistical properties of self-affine surfaces in elastic contacts: A numerical investigation. *Journal of the Mechanics and Physics of Solids*, 60(5):973–982, may 2012. doi: 10.1016/j.jmps.2012.01.006. URL https://doi.org/10.1016%2Fj.jmps.2012.01.006.

[54] N. Prodanov, W. B. Dapp, and M. H. Müser. On the contact area and mean gap of rough, elastic contacts: Dimensional analysis, numerical corrections, and reference data. *Tribology Letters*, 53(2):433–448, dec 2013. doi: 10.1007/s11249-013-0282-z. URL http://dx.doi.org/10.1007/s11249-013-0282-z.

[55] C Campañá, B N J Persson, and M H Müser. Transverse and normal interfacial stiffness of solids with randomly rough surfaces. *Journal of Physics: Condensed Matter*, 23(8):085001, February 2011. doi: 10.1088/0953-8984/23/8/085001. URL https://doi.org/10.1088/0953-8984/23/8/085001.

[56] Wolf B. Dapp, Andreas Lücke, Bo N. J. Persson, and Martin H. Müser. Self-affine elastic contacts: Percolation and leakage. *Phys. Rev. Lett.*, 108 (24):244301, jun 2012. doi: 10.1103/physrevlett.108.244301. URL http://dx.doi.org/10.1103/PhysRevLett.108.244301.

[57] L. Afferrante, F. Bottiglione, C. Putignano, B. N. J. Persson, and G. Carbone. Elastic contact mechanics of randomly rough surfaces: An assessment of advanced asperity models and persson's theory. *Tribology Letters*, 66(2), May 2018. doi: 10.1007/s11249-018-1026-x. URL https://doi.org/10.1007/s11249-018-1026-x.

[58] Roman Pohrt, Valentin L. Popov, and Alexander E. Filippov. Normal contact stiffness of elastic solids with fractal rough surfaces for one- and three-dimensional systems. *Physical Review E*, 86(2):026710, aug 2012. doi: 10.1103/physreve.86.026710. URL http://dx.doi.org/10.1103/PhysRevE.86.026710.

[59] V. A. Yastrebov, G. Anciaux, and J.-F. Molinari. From infinitesimal to full contact between rough surfaces: Evolution of the contact area. *International Journal of Solids and Structures*, 52:83–102, jan 2015. doi: 10.1016/j.ijsolstr.2014.09.019. URL https://doi.org/10.1016/j.ijsolstr.2014.09.019.

[60] M. Khajeh Salehani, J.S. van Dokkum, N. Irani, and L. Nicola. On the load-area relation in rough adhesive contacts. *Tribology International*, 144:106099, April 2020. doi: 10.1016/j.triboint.2019.106099. URL https://doi.org/10.1016/j.triboint.2019.106099.

[61] Vladislav A. Yastrebov, Guillaume Anciaux, and Jean-Francois Molinari. The role of the roughness spectral breadth in elastic contact of rough surfaces. *Journal of the Mechanics and Physics of Solids*, 107:469–493, October 2017. doi: 10.1016/j.jmps.2017.07.016. URL https://doi.org/10.1016/j.jmps.2017.07.016.

[62] P. Ranganath Nayak. Random process model of rough surfaces. *Journal of Lubrication Technology*, 93(3):398–407, July 1971. doi: 10.1115/1.3451608. URL https://doi.org/10.1115/1.3451608.

[63] Binquan Luan and Mark O. Robbins. The breakdown of continuum models for mechanical contacts. *Nature*, 435(7044):929–932, jun 2005. doi: 10.1038/nature03700. URL https://doi.org/10.1038/nature03700.

[64] Binquan Luan and Mark O. Robbins. Contact of single asperities with varying adhesion: Comparing continuum mechanics to atomistic simulations. *Physical Review E*, 74(2):026111, aug 2006. doi: 10.1103/physreve.74.026111. URL https://doi.org/10.1103/physreve.74.026111.

[65] Yifei Mo, Kevin T. Turner, and Izabela Szlufarska. Friction laws at the nanoscale. *Nature*, 457(7233):1116–1119, February 2009. doi: 10.1038/nature07748. URL https://doi.org/10.1038/nature07748.

[66] Shengfeng Cheng, Binquan Luan, and Mark O. Robbins. Contact and friction of nanoasperities: Effects of adsorbed monolayers. *Physical Review E*, 81(1):016102, January 2010. doi: 10.1103/physreve.81.016102. URL https://doi.org/10.1103/physreve.81.016102.

[67] Yifei Mo and Izabela Szlufarska. Roughness picture of friction in dry nanoscale contacts. *Physical Review B*, 81(3):035405, January 2010. doi: 10.1103/physrevb.81.035405. URL https://doi.org/10.1103/physrevb.81.035405.

[68] S Eder, A Vernes, G Vorlaufer, and G Betz. Molecular dynamics simulations of mixed lubrication with smooth particle post-processing. *Journal of Physics: Condensed Matter*, 23(17):175004, April 2011. doi: 10.1088/0953-8984/23/17/175004. URL https://doi.org/10.1088/0953-8984/23/17/175004.

[69] Tevis D. B. Jacobs and Ashlie Martini. Measuring and understanding contact area at the nanoscale: A review. *Applied Mechanics Reviews*, 69(6):060802, November 2017. doi: 10.1115/1.4038130. URL https://doi.org/10.1115/1.4038130.

[70] Tian Tang, Anand Jagota, Manoj K. Chaudhury, and Chung-Yuen Hui. Thermal fluctuations limit the adhesive strength of compliant solids. *The Journal of Adhesion*, 82(7):671–696, June 2006. doi: 10.1080/00218460600775781. URL https://doi.org/10.1080/00218460600775781.

[71] Josep C. Pàmies, Angelo Cacciuto, and Daan Frenkel. Phase diagram of Hertzian spheres. *The Journal of Chemical Physics*, 131(4):044514, July 2009. doi: 10.1063/1.3186742. URL https://doi.org/10.1063/1.3186742.

[72] M.P. Allen and D.J. Tildesley. *Computer Simulation of Liquids*. Clarendon, Oxford, 1987.

[73] Daan Frenkel and Berend Smit. *Understanding Molecular Simulation: From Algorithms to Applications*, volume 1 of *Computational Science Series*. Academic Press, San Diego, second edition, 2002.

[74] I.A. Polonsky and L.M. Keer. A numerical method for solving rough contact problems based on the multi-level multi-summation and conjugate gradient techniques. *Wear*, 231(2):206–219, July 1999. doi: 10.1016/s0043-1648(99)00113-1. URL https://doi.org/10.1016/s0043-1648(99)00113-1.

[75] Yunong Zhou, Michael Moseler, and Martin H. Müser. Solution of boundary-element problems using the fast-inertial-relaxation-engine method. *Physical Review B*, 99(14), April 2019. doi: 10.1103/physrevb.99.144103. URL https://doi.org/10.1103/physrevb.99.144103.

[76] Jiunn-Jong Wu. Numerical analyses on elliptical adhesive contact. *Journal of Physics D: Applied Physics*, 39(9):1899–1907, April 2006. doi: 10.1088/0022-3727/39/9/027. URL https://doi.org/10.1088/0022-3727/39/9/027.

[77] Simon Medina and Daniele Dini. A numerical model for the deterministic analysis of adhesive rough contacts down to the nano-scale. *International Journal of Solids and Structures*, 51(14):2620–2632, July 2014. doi: 10.1016/j.ijsolstr.2014.03.033. URL https://doi.org/10.1016/j.ijsolstr.2014.03.033.

[78] Valentine Rey, Guillaume Anciaux, and Jean-François Molinari. Normal adhesive contact on rough surfaces: efficient algorithm for FFT-based BEM resolution. *Computational Mechanics*, 60(1):69–81, March 2017. doi: 10.1007/s00466-017-1392-5. URL https://doi.org/10.1007/s00466-017-1392-5.

[79] G Carbone, B Lorenz, BNJ Persson, and A Wohlers. Contact mechanics and rubber friction for randomly rough surfaces with anisotropic statistical properties. *The European Physical Journal E*, 29(3):275–284, 2009.

[80] https://www.lmp.uni-saarland.de/index.php/research-topics/contact-mechanics-challenge-announcement/.

[81] Lior Kogut and Izhak Etsion. A finite element based elastic-plastic model for the contact of rough surfaces. *Tribology Transactions*, 46(3):383–390, January 2003. doi: 10.1080/10402000308982641. URL https://doi.org/10.1080/10402000308982641.

[82] Daniel Asenjo, Jacob D. Stevenson, David J. Wales, and Daan Frenkel. Visualizing basins of attraction for different minimization algorithms. *The Journal of Physical Chemistry B*, 117(42):12717–12723, May 2013. doi: 10.1021/jp312457a. URL https://doi.org/10.1021/jp312457a.

[83] Carl P. Goodrich, Simon Dagois-Bohy, Brian P. Tighe, Martin van Hecke, Andrea J. Liu, and Sidney R. Nagel. Jamming in finite systems: Stability, anisotropy, fluctuations, and scaling. *Physical Review E*, 90(2), August 2014. doi: 10.1103/physreve.90.022138. URL https://doi.org/10.1103/physreve.90.022138.

[84] Bernhard Eidel, Alexander Stukowski, and Jörg Schröder. Energy-minimization in atomic-to-continuum scale-bridging methods. *PAMM*, 11 (1):509–510, December 2011. doi: 10.1002/pamm.201110246. URL https://doi.org/10.1002/pamm.201110246.

[85] Ryogo Kubo. Statistical-mechanical theory of irreversible processes. i. general theory and simple applications to magnetic and conduction problems. *Journal of the Physical Society of Japan*, 12(6):570–586, June 1957. doi: 10.1143/jpsj.12.570. URL https://doi.org/10.1143/jpsj.12.570.

[86] Seiji Kajita, Hitoshi Washizu, and Toshihide Ohmori. Approach of semi-infinite dynamic lattice Green's function and energy dissipation due to phonons in solid friction between commensurate surfaces. *Physical Review B*, 82(11):115424, September 2010. doi: 10.1103/physrevb.82.115424. URL https://doi.org/10.1103/physrevb.82.115424.

[87] Seiji Kajita. Green's function nonequilibrium molecular dynamics method for solid surfaces and interfaces. *Physical Review E*, 94(3):033301, September 2016. doi: 10.1103/physreve.94.033301. URL https://doi.org/10.1103/physreve.94.033301.

[88] Herbert A David and Haikady N Nagaraja. *Order Statistics. 2003.* Wiley, New York, 2003.

[89] Martin H. Müser. Elasticity does not necessarily break down in nanoscale contacts. *Tribol. Lett.*, 67:57, jun 2019. doi: 10.1007/s11249-019-1170-y. URL https://doi.org/10.1007/s11249-019-1170-y.

[90] Lars Pastewka, Tristan A. Sharp, and Mark O. Robbins. Seamless elastic boundaries for atomistic calculations. *Physical Review B*, 86(7):075459, August 2012. doi: 10.1103/physrevb.86.075459. URL https://doi.org/10.1103/physrevb.86.075459.

[91] T. Candela, F. Renard, M. Bouchon, J. Schmittbuhl, and E. E. Brodsky. Stress drop during earthquakes: Effect of fault roughness scaling. *Bulletin of the Seismological Society of America*, 101(5):2369–2387, September 2011. doi: 10.1785/0120100298. URL https://doi.org/10.1785/0120100298.

[92] Martin H. Müser. On the linearity of contact area and reduced pressure. *Tribology Letters*, 65(4), aug 2017. doi: 10.1007/s11249-017-0912-y. URL https://doi.org/10.1007/s11249-017-0912-y.

[93] Sangil Hyun and Mark O. Robbins. Elastic contact between rough surfaces: Effect of roughness at large and small wavelengths. *Tribology International*, 40(10-12):1413–1422, October 2007. doi: 10.1016/j.triboint.2007.02.003. URL https://doi.org/10.1016/j.triboint.2007.02.003.

[94] G. C. Wick. The evaluation of the collision matrix. *Physical Review*, 80(2): 268–272, October 1950. doi: 10.1103/physrev.80.268. URL https://doi.org/10.1103/physrev.80.268.

[95] Wolf B Dapp, Nikolay Prodanov, and Martin H Müser. Systematic analysis of persson's contact mechanics theory of randomly rough elastic surfaces. *Journal of Physics: Condensed Matter*, 26(35):355002, July 2014. doi: 10.1088/0953-8984/26/35/355002. URL https://doi.org/10.1088/0953-8984/26/35/355002.

[96] Martin Müser and Anle Wang. Contact-patch-size distribution and limits of self-affinity in contacts between randomly rough surfaces. *Lubricants*, 6(4):85, September 2018. doi: 10.3390/lubricants6040085. URL https://doi.org/10.3390/lubricants6040085.

[97] A.W. Bush, R.D. Gibson, and T.R. Thomas. The elastic contact of a rough surface. *Wear*, 35(1):87–111, nov 1975. doi: 10.1016/0043-1648(75)90145-3. URL http://dx.doi.org/10.1016/0043-1648(75)90145-3.

[98] Martin H. Müser. Response to "a comment on meeting the contact-(mechanics) challenge". *Tribology Letters*, 66(1), February 2018.

doi: 10.1007/s11249-018-0986-1. URL https://doi.org/10.1007/s11249-018-0986-1.

[99] Haneesh Kesari, Joseph C. Doll, Beth L. Pruitt, Wei Cai, and Adrian J. Lew. Role of surface roughness in hysteresis during adhesive elastic contact. *Philosophical Magazine Letters*, 90(12):891–902, December 2010. doi: 10.1080/09500839.2010.521204. URL https://doi.org/10.1080/09500839.2010.521204.

[100] Robert W. Carpick and Miquel Salmeron. Scratching the surface: fundamental investigations of tribology with atomic force microscopy. *Chemical Reviews*, 97(4):1163–1194, June 1997. doi: 10.1021/cr960068q. URL https://doi.org/10.1021/cr960068q.

[101] Izabela Szlufarska, Michael Chandross, and Robert W Carpick. Recent advances in single-asperity nanotribology. *Journal of Physics D: Applied Physics*, 41(12):123001, May 2008. doi: 10.1088/0022-3727/41/12/123001. URL https://doi.org/10.1088/0022-3727/41/12/123001.

[102] Qunyang Li, Yalin Dong, Danny Perez, Ashlie Martini, and Robert W. Carpick. Speed dependence of atomic stick-slip friction in optimally matched experiments and molecular dynamics simulations. *Physical Review Letters*, 106(12), March 2011. doi: 10.1103/physrevlett.106.126101. URL https://doi.org/10.1103/physrevlett.106.126101.

[103] R.S. Bradley. LXXIX.the cohesive force between solid surfaces and the surface energy of solids. *The London, Edinburgh, and Dublin Philosophical Magazine and Journal of Science*, 13(86):853–862, April 1932. doi: 10.1080/14786449209461990. URL https://doi.org/10.1080/14786449209461990.

[104] Huajian Gao, Xiang Wang, Haimin Yao, Stanislav Gorb, and Eduard Arzt. Mechanics of hierarchical adhesion structures of geckos. *Mechanics of Materials*, 37(2-3):275–285, February 2005. doi: 10.1016/j.mechmat.2004.03.008. URL https://doi.org/10.1016/j.mechmat.2004.03.008.

[105] M.D. Pashley. Further consideration of the DMT model for elastic contact. *Colloids and Surfaces*, 12:69–77, January 1984. doi: 10.1016/0166-6622(84)80090-6. URL https://doi.org/10.1016/0166-6622(84)80090-6.

[106] Polina Prokopovich and Stefano Perni. Comparison of JKR- and DMT-based multi-asperity adhesion model: Theory and experiment. *Colloids and Surfaces A: Physicochemical and Engineering Aspects*, 383(1-3):95–101, June 2011. doi: 10.1016/j.colsurfa.2011.01.011. URL `https://doi.org/10.1016/j.colsurfa.2011.01.011`.

[107] M Wierez-Kien, A D Craciun, A V Pinon, S Le Roux, J L Gallani, and M V Rastei. Interface bonding in silicon oxide nanocontacts: interaction potentials and force measurements. *Nanotechnology*, 29(15):155704, February 2018. doi: 10.1088/1361-6528/aaad4f. URL `https://doi.org/10.1088/1361-6528/aaad4f`.

[108] M. Frigo and S.G. Johnson. The design and implementation of FFTW3. *Proceedings of the IEEE*, 93(2):216–231, February 2005. doi: 10.1109/jproc.2004.840301. URL `https://doi.org/10.1109/jproc.2004.840301`.

Appendix A

GFMD documentation

A.1 Introduction

A.1.1 Basic idea of GFMD

Green's function molecular dynamics (GFMD) is a technique allowing us to solve boundary-value problems, for example, the linear-elastic response of a solid to a boundary condition, within the framework of MD [7, 38]. The central idea is to use Fourier transform of surface modes as coordinates, which are propagated according to Newton's equations of motion.

$$m_q \ddot{\tilde{u}}(\mathbf{q}) + \eta_q \dot{\tilde{u}}(\mathbf{q}) + \frac{qE^*}{2}\tilde{u}(\mathbf{q}) = \tilde{F}(\mathbf{q}) \tag{A.1}$$

where $\tilde{F}(\mathbf{q})$ is the Fourier transform of all external forces acting on the surface atoms, $\tilde{u}(\mathbf{q})$ is the Fourier transform of displacement field $u(\mathbf{r})$. m_q and η_q represent inertia and damping coefficients of different surface modes, which may depend on the wave vector. E^* is the contact modulus.

In this GFMD solver, displacement Verlet algorithm is applied to propagate the displacement, which reads

$$\tilde{u}^{\mathrm{new}}(\mathbf{q}) = 2\tilde{u}^{\mathrm{now}}(\mathbf{q}) - \tilde{u}^{\mathrm{old}}(\mathbf{q}) + \tilde{F}(\mathbf{q})\Delta t^2 \tag{A.2}$$

The implementation and basic idea of GFMD in terms of pseudo code is sketched below.

```
- initialize all parameters
- define rigid/elastic sheet
- loop over time steps until converged
  - implement interaction in real space
  - transform displacement and force into Fourier space
  - calculate elastic restoring force
  $\tilde{F}(\mathbf{q}) = \tilde{F}(\mathbf{q}) - q(E^*/2)\tilde{u}^{\mathrm{now}}(\mathbf{q})$
  - add external pressure
  $\tilde{F}(0) = \tilde{F}(0) + p$
  - add damping force
  $\tilde{F}(\mathbf{q}) = \tilde{F}(\mathbf{q}) + \eta_q\{\tilde{u}^{\mathrm{now}}(\mathbf{q}) - \tilde{u}^{\mathrm{old}}(\mathbf{q})\}$
  - use Verlet algorithm to propagate
  $\tilde{u}^{\mathrm{new}}(\mathbf{q}) = 2\tilde{u}^{\mathrm{now}}(\mathbf{q}) - \tilde{u}^{\mathrm{old}}(\mathbf{q}) + \tilde{F}(\mathbf{q})\Delta t^2$
  - transform displacement into real space
  - implement the boundary condition
- postanalysis
```

A.1.2 Source code structure

There are 5 source code files under the src directory, which are listed in Table A.1

Table A.1: source code structure

file name	description
`header.h`	declare all libraries and all global constants
`contMech.h`	declare all global variables and global functions
`gfmdSheet.h`	declare all variables and functions to define rigid indenter, elastic sheet and the interaction
`contMech.cpp`	main function, post-analysis
`gfmdSheet.cpp`	include all information on elastic sheet and rigid indenter

A.1.3 Basic running

Because GFMD simulation is conducted in Fourier space, a fast Fourier transform library is expected to pre-installed. In the current version, FFTW is in the

position to do this job, which is a C subroutine library for computing the discrete Fourier transform[108]. More details about FFTW, including installation and manipulation, could be referred on `www.fftw.org`.

To compile a C++ program, a commonly used C++ compiler should be installed. GNU compiler is used to compile the GFMD simulation under Linux platform while clang compiler is applied under macOS platform.

The command in Linux/macOS environment to compile GFMD code would be

```
$ g++ /path/contMech.cpp /path/gfmdSheet.cpp -O2
-std=c++11 -lfftw3 -L /path/fftw/lib -I /path/fftw/include
-o contMech.exe
```

This command generates an executable file `contMech.exe`. Then run this executable file with command

```
$ ./contMech.exe
```

After several time steps, some basic data files would be given, which are sketched in Table A.2.

Table A.2: output file overview

file name	description
`gMoni.dat`	energy at each time step, including total energy, kinetic energy, potential etc.
`moni1-xxxx.dat`	some typical displacement at each time step, i.e., center of mass mode, fastest mode etc.
`elSheet1.dat`	displacement and stress of elastic sheet which are generated at the last time step
`equilPos0.dat`	profile of rigid indenter
`elSheet1.datH`	cross section of displacement and stress of elastic sheet which are generated at the last time step
`equilPos0.datH`	cross section of rigid indenter profile
`params.out`	dump out some useful information and results of post-analysis, such as contact line, contact area etc..
`params.def`	default parameters.

A.1.4 Visualization

`gnuplot` is adopted to visualize those output files (`*.dat`). `gnuplot` is a portable command-line driven graphing utility for Linux, macOS and many other platforms. More details about `gnuplot`, including installation and manipulation, could be referred to the documentation on `www.gnuplot.info`.

Suppose that the newest version of `gnuplot` is installed, the first step to use `gnuplot` is to open terminal and write a command

```
$ gnuplot
```

The user interface should look like

```
username$ gnuplot

        G N U P L O T
    Version 5.2 patchlevel 7    last modified 2019-05-29

    Copyright (C) 1986-1993, 1998, 2004, 2007-2018
    Thomas Williams, Colin Kelley and many others

    gnuplot home:     http://www.gnuplot.info
    faq, bugs, etc:   type "help FAQ"
    immediate help:   type "help"  (plot window: hit 'h')

Terminal type is now 'qt'
gnuplot>
```

To visualize a data file with `gnuplot`, we basically only need to use command `plot`. For example,

```
gnuplot> plot "elSheet1.datH" u 1:3 w l
```

This command plots the `elSheet1.datH` using the data of 1st column and 3rd column.`u` is short for `using`, `w l` means `with line`.

A.2 Parameters

Similar to LAMMPS, the current version of GFMD code executes by reading commands from an input script `"params.in"`. It is not necessary for users to read the source code line by line, instead, the users just need to write a simple input script to define parameters about the contact simulation. All parameters have default setting, which means that only those parameters that the user wants to change need to be listed in the input script.

A completed input script consists of 3 parts, global parameters, elastic sheet parameters and rigid sheet parameters. Parameter names are prompt by a hash sign `#`. There must be a space between the parameter name and the hash sign.

A.2.1 Global parameters

All global default parameters are listed in Table A.3.

Table A.3: global parameters overview

parameter	default value	description
`lengthX/lengthY`	1.0/1.0	system length along x/y direction
`nxGlobal/nyGlobal`	512/512	grid points of system along x/y direction
`nTime`	100	simulation time in unit of time step
`dTime`	0.25	time step
`dampGlobal`	1.0	global damping
`randSeed`	4711	random seed
`fLangevin`	0	switch of Langevin thermostat, `==0`: switch off; `==1`: switch on
`tempInit`	0.01	initial dimensionless temperature, out of use if `fLangevin == 0`
`tempFinal`	0.01	final dimensionless temperature, out of use if `fLangevin == 0`
`nSheet`	2	sheet number, **DO NOT** change
`fFire`	0	switch of fire optimization, `==0`: switch off; `==1`: switch on

`fireRedrct`	0.005	a factor to redirect velocity , out of use if `fFire==0`
`fireIncrmt`	1.2	a factor to increase time step, out of use if `fFire==0`
`fireDecrmt`	0.5	a factor to decrease time step, out of use if `fFire==0`

There must be a line to remind the finish of global parameter definition, it reads

```
0   # end global parameters
```

Here is an example to define the global parameters

```
1     # lengthX
512   # nxGlobal

4000  # nTime
0.25  # dTime

0     # fFire

1.0   # dampGlobal
4711  # randSeed

2     # nSheet
0     # end global parameters

...
```

A.2.2 Rigid sheet parameters

All rigid sheet parameters are listed in Table A.5.

Table A.5: rigid sheet parameters

parameter	**default value**	**description**

fRough	1	define indenter shape ==1: parabolic indenter; ==2: random roughness indenter; ==4: flat punch; ==8: single wave indenter;
nx/ny	nxGlobal/nyGlobal	grid points for indenter
rXhertz/rYhertz	1.0/1.0	radius of curvature for Hertzian indenter, out of use if fRough $\neq$ 1
hertzRescale	1.0	$>$ 1.0: blunt Hertzian indenter; $<$ 1.0: sharp Hertzian indenter
hurst	0.8	hurst exponent, out of use if fRough $\neq$ 2
lambdaR	0.5	roll-off wavelength, out of use if fRough $\neq$ 2
lambdaS	0.005	short wavelength cut-off, out of use if fRough $\neq$ 2
fRollOff	1	switch of smooth roll-off, ==1: smooth roll-off; ==0: roll-off wavelength = long wavelength cutoff; ==2: roll-off with cusp; out of use if fRough $\neq$ 2
fRNorm	1	normalize rough indenter, == 1: normalize to rms gradient; == 2: normalize to rms height; out of use if fRough $\neq$ 2
rRoughNorm	1.0	specify a value for rms gradient/height, out of use if fRough $\neq$ 2.
fIndMode	0	punch shape, ==0: spherical flat punch; ==1: line flat punch; out of use if fRough $\neq$ 4.

indRadius	0.2*lengthY	punch radius, out of use if fRough $\neq$ 4.
indHeight	0.2*lengthY	punch height, out of use if fRough $\neq$ 4.
fRStep	0	change smooth indenter to step indenter, ==0: switch off; ==1: switch on;
rRoughStep	1.0/200	step height, out of use if fRStep = 0.
fBoxMuller	0	use BoxMuller random seed generator
heightWarp	0.0	warped surface
peklenik	1.0	anisotropic surface

Rigid indenter is set to sheet 0 by default. GFMD simulation starts to read indenter parameters after reading

```
1 0 # sheet start
```

and stop to read indenter parameters after reading

```
1 0 # sheet end
```

General Hertzian indenter

In this section, the input script of a general Hertzian indenter is sketched. The functional form of this indenter is given by

$$h(\mathbf{r}) = \frac{1}{2\alpha}\left(\frac{r^2}{R_\mathrm{c}}\right)^\alpha$$

where R_c denotes radius of curvature, α indicates the rescale factor, if $\alpha = 1$, the indenter is a typical parabola, if $\alpha < 1$, the indenter become sharp while it become blunt if $\alpha > 1$. Assume that the indenter grid point is set by default, and $R_\mathrm{c} = 1.0$. The input file should reads

```
1 ...
2
3 0 # sheet start
4 1 # fRough
5 1.0 # rXhertz
6 1.0 # hertzRescale
7 0 #sheet end
8
9 ...
```

The indenter profile could be plotted using gnuplot with command

```
1 gnuplot> plot "equilPos0.datH" u 1:2 w l
```

the cross section of this indenter is depicted as below.

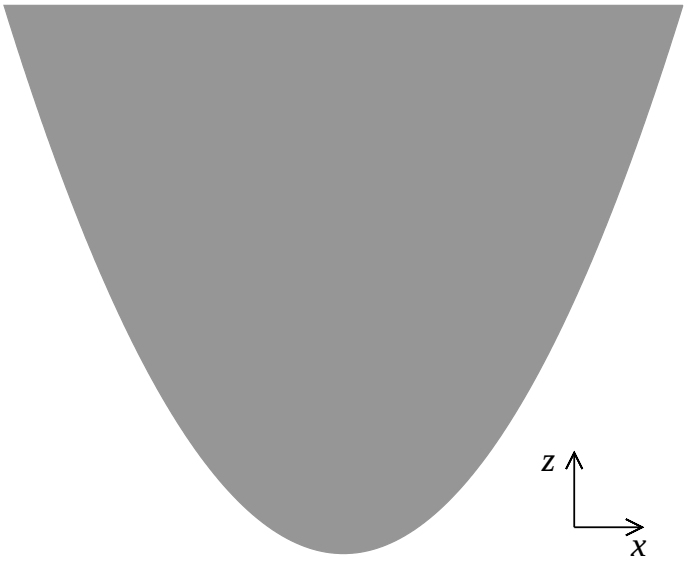

Figure A.1: parabolic indenter

Random roughness indenter

A typical random rough surface is fully defined by a height power spectrum function, which reads

$$\begin{aligned} C(\mathbf{q}) &= \langle|\tilde{h}(\mathbf{q})|^2\rangle \\ &= \frac{C(0)\Theta(q_s - q)}{\{1 + (q/q_r)^2\}^{(1+H)/2}} \end{aligned}$$

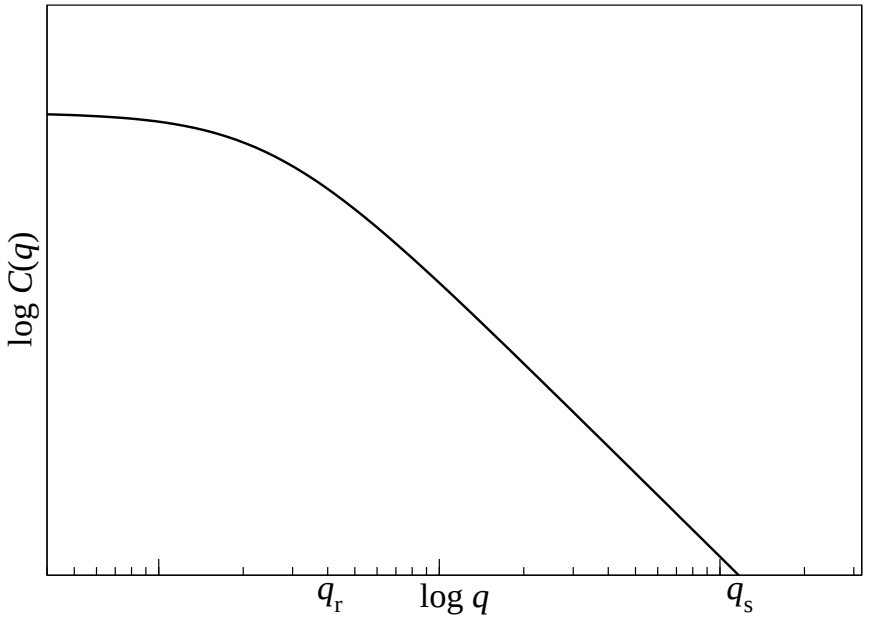

Figure A.2: Surface roughness power spectrum of a surface which is self-affine fractal for $q_s > q > q_r$. The roll-off wavevector q_r and short wavevector cut-off q_s depend on the system under consideration.

Here, $\tilde{h}(\mathbf{q})$ is the Fourier transform of the height $h(\mathbf{r})$. $q_r = 2\pi/\lambda_r$ is the roll-off wave number and $q_s = 2\pi/\lambda_s$ is the cut-off wave number. $H = 0.8$ is Hurst exponent, $\Theta(\bullet)$ is the Heavyside step function. The data is normalized by selecting $C(0)$ such that the root-mean-square (rms) gradient of the surface satisfies $\bar{g} = 1$.

If $\lambda_r = 0.25L_x$, $\lambda_r/\lambda_s = 128$, the input file should reads

```
...

0 # sheet start
2 # fRough
0.8 # hurst
0.25  # lambdaR
2e-3  # lambdaS
1 # fRollOff
1 # fRNorm
0 # sheet end
...
```

Figure A.3: cross-section plot of random roughness surface

Flat punch

A typical spherical flat punch with radius curvature $R_c = 0.2$, height $h = 0.2$ is defined as below.

```
0 # sheet start
4 # fRough
0 # fIndMode
0.2 # indRadius
0.2 # indHeight
...
0 # sheet end
```

A linear flat punch with height $h = 0.2$ should be defined as below.

```
0 # sheet start
4 # fRough
1 # fIndMode
0.2 # indHeight
...
0 # sheet end
```

Figure A.4: cross-section plot of flat punch

Stepped indenter

A stepped indenter with $R_c = 1.0$, step height $h_s = 0.005$ is defined as below.

```
0 # sheet start
1 # fRough
1.0 # rXhertz
1 # fRStep
5e-3  # rRoundStep
0 # sheet end
```

A.2.3 Elastic sheet parameters

This version of GFMD code is designed to solve contact problems of linear elastic solid with either finite or semi-infinite thickness. All parameters about the elastic solid are listed in Table A.7.

Table A.7: elastic sheet parameters overview

parameter	default value	description
elaDim	1	elastic dimension.
pressure	0.01	external pressure working on elastic sheet
pressFinal	pressure	pressure at the last time step
nx/ny	nxGlobal/nyGlobal	grid points of elastic sheet
contactMod	1.0	contact modulus
poisson	0.25	Poisson ratio
fThickness	0	elastic sheet property, ==0: infinite thickness; ==1: constant stress; ==2: constant strain;
thickness	lengthY	elastic sheet thickness
fConstCOM	0	center-of-mass (COM) constrained if ==1.
zConstCOM	0	position of COM mode when COM is constrained
vConstCOM	0	velocity of COM mode

A typical elastic sheet is defined as below.

```
1 # sheet start
1 # elaDim
2 # contactMod
0.25  # poisson
1e-3  # pressure
1 # fThickness
0.5 # thickness
0 # fConstCOM
...
1 # sheet end
```

In this `params.in`, an elastic sheet with contact modulus $E^* = 2.0$, Poisson ratio $\nu = 0.25$, external pressure $p = 0.001$ and thickness $h = 0.5$ is defined.

A.2.4 Read old configuration

Sometimes GFMD simulation requires to read configuration from a data file rather than initializing configuration from scratch. Towards this end, the data file of this configuration should be renamed.

If the old configuration is elastic solid, the file should be renamed to `elSheet1.old` and the data arrangement should be consistent with `elSheet1.dat`.

For rigid indenter, the situation is different because it is only allowed to read the rigid indenter in Fourier space. In this case, the first two columns correspond to q_{x} and q_{y}, respectively and the last two columns indicate the real and imaginary part of Fourier transform of the height position.

A.3 Interaction

So far, the elastic and rigid configuration are fully defined. In this section, the interaction between these two sheets would be sketched. All parameters related interactions are listed in Table A.9.

Table A.9: interaction parameters overview

`fMorse`	`0`	define interaction type, `==0`: hard-wall constraint; `==1`: adhesion + hard-wall `==2`: adhesion + short-ranged repulsion;
`morse2sheet`	`1`	apply interaction to a specified sheet
`surfEner`	`1e-4`	surface energy, out of use if `fMorse` = 0
`sigMorse`	`1e-3*lengthY`	finite distance, out of use if `fMorse` = 0
`surfDist`	`1`	initial distance between sheets, in unit of `dy`. out of use if `fMorse` = 0
`const2sheet`	`0`	apply hard-wall constraint to a specified sheet, `==2`: switch off hard-wall constraint

A.3.1 Hard-wall constraint

Hard-wall constraint is one of the most commonly used interactions in contact simulations, in which case the elastic sheet is not allowed to penetrate the rigid indenter. It is defined as

$$\gamma(g) = \begin{cases} \infty & \text{if } g < 0 \\ 0 & \text{else}\,. \end{cases}$$

where g is the gap between indenter and elastic sheet.

Hard-wall constraint is the default setting in GFMD code. Therefore, if there is no interaction specified in input script, the interaction would be hard-wall. Be careful that the `const2sheet` is a parameter which should be defined in elastic sheet.

A.3.2 Adhesion interaction and hard-wall constraint

Suppose $z(x, y)$ denotes the profile of rigid indenter, the displacement of elastic sheet, $u(x, y)$ is formally a function of both in-plane coordinates. The gap $g(x, y)$ indicates the distance between the deformed elastic sheet and undeformed tip, i.e.,

$$g(x, y) = z(x, y) - u(x, y)$$

It is furthermore assumed that the tip cannot penetrate the substrate, which is the hard-wall constraint. The finite-range adhesive interaction, which only depend on the local gap. The default expression would be

$$\gamma(g) = -\gamma_0 \int d^2r \exp\{-g(x, y)/\sigma_{\mathrm{M}}\} \tag{A.3}$$

where γ_0 is surface energy per unit area, σ_{M} is a single length scale. They are `surfEner` and `sigMorse` in `params.in` respectively.

Here is an example about the adhesion with hard-wall constraint.

```
0 # sheet start
...
1 # fMorse
1 # morse2sheet
2e-4  # surfEner
1e-3  # sigMorse
1  # surfDist
0 # sheet end

1 # sheet start
...
0 # const2sheet
1 # sheet end
```

In this example, $\gamma_0 = 2 \times 10^{-4}$ and $\sigma_{\mathrm{M}} = 1 \times 10^{-3}$.

A.3.3 Adhesion interaction and short-ranged repulsion

This interaction consists of a short-range adhesion and an even shorter-ranged repulsion. The expression is

$$\gamma(g) = \gamma_0 \int d^2r \left\{ \mathrm{e}^{2\{z_0 - g(x,y)\}/\sigma_\mathrm{M}} - 2\mathrm{e}^{\{z_0 - g(x,y)\}/\sigma_\mathrm{M}} \right\}$$

where γ_0 denotes the surface energy per unit surface area, $g(x, y)$ the gap between indenter and elastic sheet. We should notice that hard-wall constraint should be switched off if Morse potential is switched on. Here is an example.

```
0 # sheet start
...
2 # fMorse
1 # morse2sheet
1e-4  # surfEner
1e-3  # sigMorse
1 # surfDist
0 # sheet end

1 # sheet start
...
2 # const2sheet
1 # sheet end
```

A.4 Examples

So far, the elastic sheet configuration, rigid indenter configuration, and the interaction are fully defined, which are sufficient to run a frictionless contact simulation. In this section, some typical contact examples would be presented, so that the user could get familiar with the manipulation of the GFMD code.

All examples are (2+1) dimensional and run quickly. Most of them require roughly 1 minute to equilibration. Each problem needs an input script(`params.in`) and generates a variety of output files(`*.dat and *.datH`).

A.4.1 Hertzian contact problem with hard-wall constraint

```
1.0 # lengthX
512 # nxGlobal

4000  # nTime
0.25  # dTime

1.0 # dampGlobal

0 # end global parameters

0 # sheet start
1 # fRough
1.0 # rXhertz
0 # fMorse
0 # sheet end

1 # sheet start
1 # elaDim
1 # fThickness
1.0 # thickness
1e-3 # pressure
0 # const2sheet
1 # sheet end
```

In this example, the sample size is 1.0×1.0, grid points is 512×512, therefore, the grid distance would be $\Delta a \approx 2.0 \times 10^{-3}$. The rigid substrate is defined as parabolic indenter with radius curvature $R_\mathrm{c} = 1.0$. The effective modulus E^* and Poisson ratio ν are not declared in this script, therefore we use default value, which are $E^* = 1.0$ and $\nu = 0.25$ respectively. The elastic sheet thickness is $h = 1.0$ and it is constant stress boundary condition. The external pressure is defined as $p = 0.001$.

Assuming that $\Delta a = 0.25$Å is the typical atom distance and $E^* = 1$GPa the typical effective modulus. Therefore, we could calculate that the radius curvature of indenter would be $R_\mathrm{c} = 512\Delta a = 12.8$nm, the external load would be $L = 0.164$nN.

According to classical Hertzian theory, the distribution of interfacial stress in the contact area as a function of distance from the center of the contact area should be

$$\sigma_z(r) = \sqrt{p_0(1 - \frac{r^2}{a_c^2})}$$

where $a_c = [3LR_c/(4E^*)]^{1/3}$ and $p_0 = 3L/(2\pi a_c^2)$. These expressions could be found in any contact mechanics related textbook.

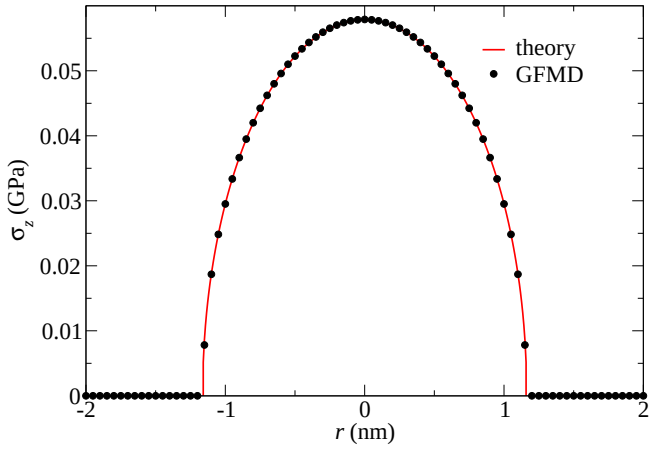

Figure A.5: Interfacial stress σ_z as a function of distance r from the central point of contact area in a Hertzian contact geometry. The (red) solid line represents the analytical solution to the Hertz problem, the (black) solid circles reflect the GFMD simulation.

In a regular Hertzian contact simulation, we should notice that the contact radius is required to be much less than the radius curvature of indenter. To validate the reliability of GFMD simulation on Hertzian contact problem, we could dump out the cross section of displacement field and check if the displacement outside contact area decays as function $1/r$.

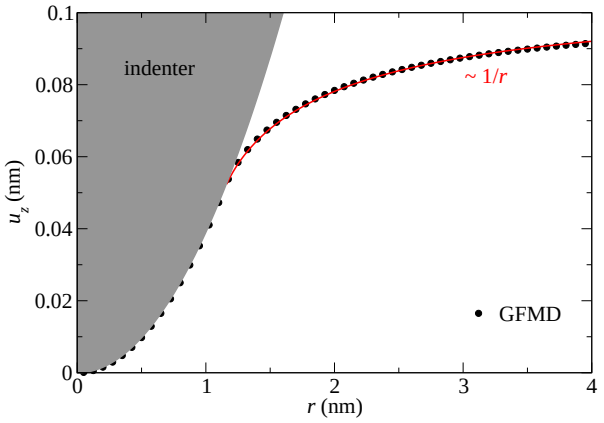

Figure A.6: displacement field $u_z(r)$ as a function of distance r from the symmetry axis. The (black) solid circle denotes the GFMD simulation, (red) solid line represents the displacement outside contact area decays as a function of $1/r$.

A.4.2 Hertzian contact problem with adhesion interaction

```
6000  # nTime

0 # end global parameters

0 # sheet start
1 # fMorse
1 # morse2sheet
2e-4 # surfEner
1e-3 # sigMorse
0 # sheet end

1 # sheet start
1 # elaDim
1 # fThickness
1.0 # thickness
5e-4 # pressure
0 # const2sheet
1 # sheet end
```

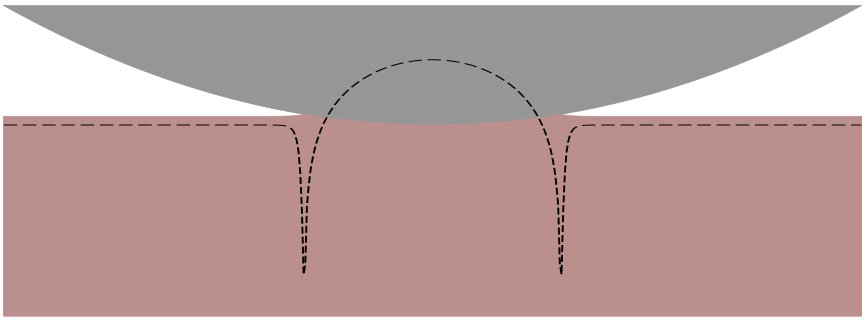

Figure A.7: A short-range adhesion, elastic solid of infinite thickness compressed by a parabolic indenter. The dotted line shows the associated stress profile.

In this example, we implement adhesion into original hard-wall constraint. For more details about the adhesion, we could go back to section 3.2. In this example, we set $\gamma_0 = 2.0 \times 10^{-4}$ and $\sigma_{\mathrm{M}} = 1.0 \times 10^{-3}$. Therefore, we could calculate that

the Tabor parameter would be $\mu_{\mathrm{T}} = [R_{\mathrm{c}}\gamma_0^2/(E^{*2}\sigma_{\mathrm{M}}^3)]^{1/3} \approx 3.42$, which closes to a typical short-range adhesion limit.

A.4.3 Rough surface contact problem with adhesion interaction

```
1 # lengthX
32768  # nxGlobal

3000 # nTime
0.25  # dTime

1 # dampGlobal
4711  # randSeed

0 # end global parameters

0 # sheet start
2 # fRough
1 # fMorse
1 # morse2sheet
2e-5 # surfEner
2.071e-5 # sigMorse
0 # sheet end

1 # sheet start
1 # elaDim
0 fThickness
1e-2  # pressure
0 # const2sheet
1 # sheet end
```

The stochastic properties of a random roughness surface are fully defined by the following variables: Hurst exponent H, linear system size $\mathcal{L}$, roll-off wavelength λ_{r}, short wavelength cut-off λ_{s}, height power spectrum $C(q_{\mathrm{r}})$ and in the case of numerical simulations, Δa, which represents the resolution of the discrete elastic

manifold. In this example, we don't use the parameters defined in the input script, instead, we read the old configuration from `equilPos0.Fourier.old`. One could download the surface from contact mechanics challenge webpage. Regarding the elastic sheet, we set `fThickness = 0`, which means that we are going to study an semi-infinite thickness elastic layer. The external pressure is set to $p = 0.01$.

There is a straightforward way to validate this example. Since all parameters defined in this script are consistent with those parameters defined in contact mechanics challenge paper [39], therefore, after equilibrium, we should get identical interfacial stress profile as contact mechanics challenge. The result is listed below.

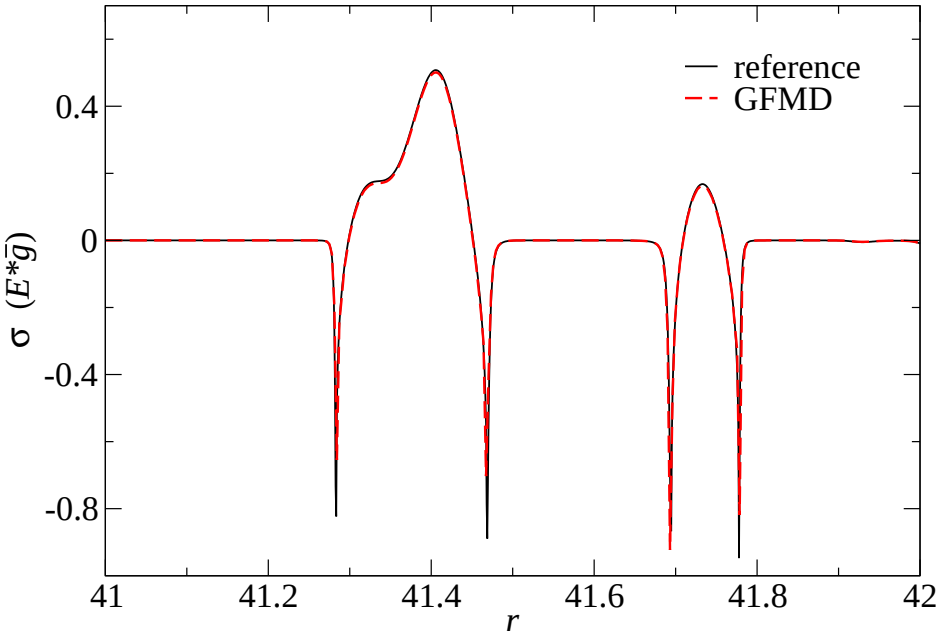

Figure A.8: Interfacial stress profile along a selected cross-section. solid (black) curve is reference data downloaded from contact mechanics challenge website, dashed (red) curve is GFMD result.

A.4.4 Hertzian contact problem with Morse potential

```
1.0 # lengthX
512 # nxGlobal

6000  # nTime
0.25  # dTime

1.0 # dampGlobal

0 # end global parameters

0 # sheet start
1 # fRough
1.0 # rXhertz
2 # fMorse
1 # morse2sheet
1e-4 # surfEner
1e-3 # sigMorse
0 # sheet end

1 # sheet start
1 # elaDim
1 # fThickness
1.0 # thickness
5e-4 # pressure
2 # const2sheet
1 # sheet end
```

A.5 Optimizations

In the given context, some optimization would be briefly introduced and the realizations would be discussed in details, so that the user could optimize a GFMD simulation in a proper manner.

In this section, the solution of either a typical Hertzian or a randomly rough contact problem is optimized. All parameters are well chosen so that the interaction is in the limit of short-range adhesion. For more details, please read this paper [75].

A.5.1 Fast inertia relaxation engine (FIRE)

The basic idea of FIRE is sketched in Erik's work [47]. Here we only outline the pseudo code of FIRE optimization.

```
- regular MD procedure
- propagate with Verlet algorithm
- FIRE optimization
  - calculate total potential energy V_tot^now and V_tot^old
  if (V_tot^now < V_tot^old)
    - move velocity direction to steepest-descent direction
      v → (1 − α)v + αF̃|v|
    - increase time step Δt
      Δt → min(f_inc Δt, Δt_max)
  else if (V_tot^now > V_tot^old)
    - freeze system
      v = 0
    - decrease time step Δt
      Δt → f_dec Δt
- back to MD procedure
```

For a FIRE optimization, 3 parameters should be declared explicitly, which are α, f_{inc} and f_{dec}. All of them are fully defined in the GFMD code, which are listed in the table.

parameter	default value	description
`fFire`	0	`==0`: switch off; `==1`: switch on.
`fireRedrct`	0.005	factor to redirect velocity direction, α
`fireIncrmt`	1.2	factor to increase time step, f_{inc}
`fireDecrmt`	0.5	factor to decreasxe time step, f_{dec}

Because FIRE optimization is sensitive to different configuration and different interaction, therefore, sometimes FIRE related parameters are needed to adjust for different simulations.

To find the best parameter set for specified simulation, the best practice would be choosing $\alpha = 0$, $f_{\mathrm{inc}} = 1.0$ and $f_{\mathrm{dec}} = 1.0$ at beginning, which means that we only switch on FIRE but change neither velocity $\mathbf{v}$ nor time step Δt. But it doesn't mean that we would get the same potential energy trajectory as the potential energy trajectory when we switch off FIRE, because when $V_{\mathrm{tot}}^{\mathrm{now}} < V_{\mathrm{tot}}^{\mathrm{old}}$, the system would be frozen up. If there is no error information, we could increase the value of α to redirect the velocity, increase the value of f_{inc} and decrease the value of f_{dec} to adjust the time step. Here is an example script.

```
4000  # nTime

1 # fFire
0.005 # fireRedrct
1.2 # fireIncrmt
0.5 # fireDecrmt

0 # end global parameters

0 # sheet start
1 # fRough
2 # fMorse
1 # morse2sheet
2e-4  # surfEner
1e-3  # sigMorse
0 # sheet end

1 # sheet start
```

```
1 # elaDim
1 # fThickness
1 # thickness
5e-4  # pressure
2 # const2sheet
1 # sheet end
```

A.5.2 Mass-weighted GFMD

The basic idea of mass-weighted has sketched in our publication[75]. In this manual, we would like to introduce how to optimize simulation with mass- weighting in our GFMD code.

Unlike FIRE optimization, we don't have any parameters to be adjusted, to optimize a typical simulation with mass-weighted algorithm, the only thing we need to do is to switch on mass-weighted and choose a reasonable zero mode mass.

parameter	default value	description
`fMassweightg`	0	`==0`: switch off; `==1`: switch on
`zeroModeMass`	1	zero mode mass

Regarding mass-weighting optimization, we should keep in mind that this optimization cannot work with hard-wall constraint. Another thing that we should be careful is that these two parameters are not global parameters, they are elastic sheet parameters. Here is an example script.

```
4000  # nTime
0.1 # dTime

10  # dampGlobal

0 # end global parameters

0 # sheet start
1 # fRough
```

```
2 # fMorse
1 # morse2sheet
2e-4  # surfEner
1e-3  # sigMorse
0 # sheet end

1 # sheet start
1 # elaDim
1 # fThickness
1 # thickness
5e-4  # pressure
2 # const2sheet
1 # fMassWeightg
1 # zeroModeMass
1 # sheet end
```

A.5.3 FIRE mass-weighting GFMD

It has been demonstrated that FIRE can successfully accelerate a regular GFMD calculation resulting a remarkable speed up. It can also be combined in a straightforward fashion with other accelerator of GFMD method, such as mass-weighting optimization. The only thing we need to do is to switch on these two optimizations in script and adjust parameters for different simulations. Here is an example script.

```
4000  # nTime
0.05   # dTime

1 # fFire

0 # end global parameters

0 # sheet start
1 # fRough
2 # fMorse
```

```
1 # morse2sheet
2e-4  # surfEner
1e-3  # sigMorse
0 # sheet end

1 # sheet start
1 # elaDim
1 # fThickness
1.0 # thickness
5e-4  # pressure
2 # const2sheet
1 # fMassWeightg
1 # sheet end
```